Title
Laser Ablation Mass Spectrometry for Fuel Analysis

Author
Mason, William

Publication Date
2022

Peer reviewed|Thesis/dissertation

Laser Ablation Mass Spectrometry for Nuclear Fuel Analysis

by

William Mason

A dissertation submitted in partial satisfaction of the

requirements for the degree of

Doctor of Philosophy

in

Nuclear Engineering

in the

Graduate Division

of the

University of California, Berkeley

Committee in charge:

Professor Peter Hosemann, Chair
Professor Lee Bernstein
Professor Paul Renne

Summer 2022

Laser Ablation Mass Spectrometry for Nuclear Fuel Analysis

Abstract

Laser Ablation Mass Spectrometry for Nuclear Fuel Analysis

by

William Mason

Doctor of Philosophy in Nuclear Engineering

University of California, Berkeley

Professor Peter Hosemann, Chair

Femtosecond and faster lasers have ushered in a new regime of physics. Because their pulse duration is shorter than the phonon relaxation time of most materials, they deposit energy with almost no loss to the surrounding area. Calibration curves using NIST Glass, CRM 125-A, and tungsten metal allowed the use of Laser Ablation Inductively Coupled Plasma Mass Spectrometry (LAMS) to interrogate element distributions in Pressurized Water Reactor fuel surrogates fabricated at Los Alamos National Laboratory. LAMS can be faster and less expensive than traditional acid dissolution of surrogate PWR fuel pellets. With traditional acid dissolution, spatial information is mostly lost, whereas LAMS offers the possibility of three-dimensional isotope analysis. This three-dimensional data could help resolve longstanding issues in fission product movement through the fuel. The LAMS system used here had a limit of detection for tungsten of approximately 800 parts per billion, which is better than the Los Alamos neutron tomography study (Tremsin et al., 2013) but not state of the art. A calibration curve for tungsten was obtained with a least-squares residual $R^2 = 1$ (Sewall, 1921). Isotope ratios were generally within 1% of declared values. These results corroborate the findings of the LANL study and suggest LAMS a cost effective approach for rapid three-dimensional analysis of spent fuel. Other applications may include fuel fabrication, additive manufacturing, and nuclear forensics.

for Bahia

Contents

List of Figures

List of Tables

Acknowledgments

My deep gratitude to Karl van Bibber for being a source of knowledge, encouragement, and leadership by example. I'm grateful that he took a chance on me and have been changed by the experience. Peter Hosemann lent patience and technical insight that profitably shaped the course of research. The group meetings brought together a spectrum of disciplines and expertise like nothing else I've experienced. His guidance at key junctures carried the issue to favorable conclusion. Thanks to Lee Bernstein for teaching nuclear physics with humor and verve while sharing startling insights into the structure of the natural world. Thanks also to his protégés, Amanda Lewis and Eric Matthews, for long hours spent working through details and providing insightful feedback. Kirsten Wimple-Hall went well out of her way to provide superior administrative guidance and support during some heavy hours.

The Lawrence Livermore group endured endless questions and false starts. Dr. Brett Isselhardt generously shared lab space, instrumentation, and good humor. David Weisz was pivotal to my success in several ways, from handling the grit of daily lab work to freely sharing key insights. He embodies the spirit of his distinguished academic heritage. Dr. Reto Trappitsch is one of the most gifted experimentalists I've ever met and possesses near-psychic knowledge of electronics. His multiple interventions to restore the laser or computer or Python code, with good humor all the while, ensure that all the rounds are on me. Josh Wimpenny provided a comprehensive method for calibrations and patiently explained many key aspects of geochemistry. Erick Ramon got me off the ground with the mass spectrometer and answered many questions as I found my legs. Peter Boone provided inspiration and good conversation as office mate and lab partner. John at Ion Flight answered my late-night calls to meet deadlines. Long ago Ross Williams and Brad Esser took me under their wing as a wide-eyed summer intern to begin an arc that, 20 years later, has come full circle.

Many fellow students contributed substantively over the years. Justin Ellin, Evan Still, Franziska Schmidt, Hi Vo, Tim Genda, Jeff Graham, and Darrell Stepter all worked selflessly to help me understand various concepts. Dajie Sun spent many hours and days clarifying mathematics, teaching code, and demonstrating the best of humanity.

Most of all to the memory my parents, truly of the Greatest Generation.

I said, 'I shall repay my debt',
But it was even as the sky; unapproachable.
- Chinese proverb

Chapter 1

Introduction

1.1 Energy Production

Energy production is a growing concern for countries around the world as populations continue to increase. Society consumes more energy than is presently available through renewable sources. Though this gap is likely to narrow over the coming years, renewable energy alone is not sufficient to meet present demand. Nuclear energy, when the carbon costs of mining, enrichment, transportation, concrete for plant construction, and spent fuel storage are included, is about as efficient as solar energy in terms of energy produced over energy required to produce. However, modern designs could dramatically increase nuclear efficiency and safety. Given the recent shift away from Russian oil and natural gas in Europe, the need for progress in nuclear power is greater than ever. Energy sources such as hydroelectric and natural gas are well suited to account for daily short-term fluctuations in energy demand because their power output is more easily adjusted than that from a nuclear reactor, but nuclear is the best option to meet mid-term demands.

High-Temperature Gas-cooled Reactors (HTGRs) possess several advantages over sodium- and lead-cooled reactors (Patel, 2019). Helium is virtually inert and monophasic, so there are no transitions between, for example, liquid and vapor. Helium does not dissociate in the manner of diatomic gases such as nitrogen ($N_2 \rightarrow 2N$). Crucial to diagnostic ease is helium's optical transparency at operating conditions. The disadvantage of high temperature gas-cooled reactors is the demand on fuel to contain fission products at high temperature and high neutron flux. Tri-Structural Isotropic (TRISO) fuel proposes to do this using various combinations of SiC and pyrolytic carbon to trap fission products and provide a high strength shell.

Recent developments in small modular reactors hold potential for improvements in nuclear safety and power distribution. However, current designs are plagued by limitations in the ability to retain certain fission products in the TRISO fuel. Silver has been particularly

challenging, despite decades of research (van Rooyen et al., 2014). The quest for new materials that will contain or capture all fission products continues to drive research in this area. A combination of femtosecond laser technology with mass spectrometry to rapidly assess fission product migration in SiC and standard fuel pins is sought.

Analysis of nuclear fuel is important for both power production and forensics applications but is hampered by the high activity of spent fuel. A person standing next to a spent reactor core would receive a lethal dose in seconds. Heavily shielded facilities provide the capability to analyse spent fuel rods but the processes are time, energy, and resource intensive. Current methods rely on acid dissolution of spent fuel, which loses most of the spatial information. The ability to ablate through fuel cladding and into the fuel itself could provide spatial maps of isotope concentrations. One goal of this work is to lay the groundwork for rapid remote interrogation of spent fuel using femtosecond laser ablation on National Institute of Standards and Technology (NIST) reference standards and then on surrogate nuclear fuel pellets of depleted uranium containing various dopants such as tungsten.

1.2 Laser Ablation Inductively Coupled Plasma Mass Spectrometry

Laser ablation mass spectrometry (LAMS) offers a promising approach to analyse spent fuel. Because it could potentially be remotely operated at some standoff distance to the fuel, this technique invites development of forensic applications. LAMS offers a path to realize remote standoff analysis of spent nuclear fuel. Mass spectrometry provides better detection limits than optical emission spectroscopy and much faster analysis than more sensitive techniques such as secondary ion mass spectrometry (SIMS). However, (Miliszkiewicz et al., 2015) assert that the signal's vulnerability to variations in the matrix have presented challenges, particularly with nanosecond and longer pulsed lasers.

Femtosecond lasers have ushered in a new regime of physics because the pulse duration (or pulse width) is shorter than the phonon relaxation time of most materials. For nanosecond and longer duration pulses, phonons and electrons in the material respond to the incoming electromagnetic energy of the laser pulse and carry away some fraction of the laser energy during the ablation process. This leads to heating and melting of the surrounding material, decreasing the ablation efficiency of the laser. With femtosecond and faster lasers, there is very little energy lost to phonon transport, providing cleaner ablation craters with almost no melting or spatter when optimized.

Mass spectrometry has long been the technique of choice for isotopic analysis in disciplines such as nuclear forensics and fuel analysis. The ability to precisely determine isotopic ratios

has opened powerful avenues for quantification in the geologic and life sciences. However, determining absolute concentrations requires the use of standards. The National Institute of Science and Technology (NIST) and the United States Geological Survey (USGS) produce standards relevant to this investigation. NIST 610, 612, and 614 (Wise & Watters, 2012) offer a starting point for quantifying LAMS performance.

NIST Glass Concentrations	
Sample	U Concentration [ppm]
610	461.5 ± 1.1
612	37.38 ± 0.08
614	0.823 ± 0.02

Table 1.1: NIST Glasses provide known concentrations of various elements and can be used to build calibration curves for mass spectrometry applications.

(MacLean, 2004) found that the isotope ^{110m}Ag ($\tau = 249.83 \pm 0.04$d), produced by neutron capture in ^{109}Ag, is the principal long-lived silver nuclide used to monitor the release of silver from coated particle fuel such as TRISO. The precursor to ^{109}Ag is the fission product ^{109}Pd ($\tau_{\frac{1}{2}} = 13.5$ hours Kumar et al. (2016)), which β^- decays to ^{109}Ag. Thus ^{110m}Ag is actually an activation product rather than a direct fission product, though commonly categorized as a fission product for convenience in the literature. The presence of Ag, Cd, and Pd as absorbers in control rods also increases the likelihood of finding their activation products in the circulation pathways of high-temperature reactors. However, (López-Honorato et al., 2011) and (López-Honorato, Yang, et al., 2010) found that heavily faulted grains do not necessarily release products because samples with good performance also had a high density of stacking faults. (MacLean, 2004) found no diffused silver from intact SiC, which implies that either nanofractures or neutron bombardment (as suggested by (B. G. Kim et al., 2015)) plays a role in the escape of Ag. The inner pyrolytic carbon layers are shown to effectively trap a significant fraction of fission gases such as Cs, but are ineffective at stopping Ag (but see (López-Honorato, Fu, et al., 2010) for a contrasting view). From (Cancino-Trejo et al., 2018): "The ease with which ^{110m}Ag can diffuse through SiC has baffled scientists, leading to a wide range of experiments and theories." The problem is complex and subtle. The aim of this work was to determine the effectiveness of femtosecond lasers for ablation of simulated PWR fuel and TRISO surrogates, with positive results.

1.3 High Temperature Gas Reactors (HTGR)

The ability of fast reactors to transmute actinides to shorter lived nuclides and convert ^{238}U to ^{239}Pu provides a powerful incentive to develop fast reactor technology. Fast reactors,

so named because neutrons are not moderated, have long been known to possess favorable characteristics. The Experimental Breeder Reactor at the Idaho National Reactor Testing Station in 1951 demonstrated the first instances of electric output from a nuclear reactor. Uranium was believed scarce and breeder reactors were identified as the best way to optimize energy extraction per unit mass of uranium. However, several issues plague fast reactors. Because neutrons are not moderated, they have a smaller cross-section and a longer mean free path, requiring higher enrichment to begin a sustainable chain reaction, with an increase in cost. In the long run, fast reactors can be more cost-effective if they achieve higher burnup and can run longer with more stable power output (Krane, 1988).

Another complicating factor is the need for more efficient cooling because fast reactors are smaller. Sodium-cooled reactors have the longest history, but sodium is highly reactive to both air and water while being opaque to visible light, making inspection and diagnostics difficult. The development of airtight, leakproof systems remains a challenge. Similar concerns apply to lead and lead-bismuth-eutectic coolants because lead is toxic, opaque, and corrosive at high temperature. Water is not viable for fast reactors because the hydrogen atoms will serve to moderate neutrons, disrupting the desired energy spectrum. These issues led to the development of helium as a coolant. Helium is transparent to visible light, monophasic, monatomic, activation resistant, and chemically inert. High flow rates are required to achieve the required cooling rates, but are technically feasible.

Though uranium reserves are more plentiful than original estimates, the ability to transmute long-lived isotopes into short-lifetime actinides coupled with much higher energy efficiency and the ready ability to convert weapon plutonium into energy make the quest for fast reactors a worthy goal. The process of generating ^{239}Pu for weapons is markedly different from that for power extraction by burning actinides (Touran, 2009). Nevertheless, President Carter mandated that US systems would use an open cycle. The benefits of fast reactors continue to attract research interest around the world. A critical step on this path is the development of a fuel form that can contain all fission products. Silicon carbide (SiC) shows promise and contains almost all fission products within regulatory limits. However, silver escapes at levels that pose a threat to worker safety and in a manner that remains unclear in the details. Femtosecond lasers coupled with mass spectrometry offer the hope of standoff fuel characterization capability with minimal fractionation and small heat-affected zone at any wavelength (Sonzogni, 2021).

1.4 Nuclear Fuel Analysis

Nuclear fission has provided commercial power for decades. Modern reactor designs promise higher efficiency and improved safety over early designs. However, they are limited by a few key problems, one being the unexplained release of silver from the SiC confining layers in

TRISO particles. For example, silver contamination was found in an Indian reactor (Sonwalkar et al., 2018).

The ability to determine the spatial position of fission products also provides a powerful diagnostic capability. Fuel analysis typically requires physical manipulation of the fuel elements and examination under an optical or scanning electron microscope to obtain Energy Dispersive X-Ray (EDX) spectra or backscatter images of high-Z material. Standoff ablation followed by mass spectrometry of the ablated fuel (either PWR fuel pin or TRISO sphere) would provide a more pristine snapshot of material conditions inside the fuel sooner than is possible with more hands-on methods such as EDX. Standoff laser ablation would allow determination of isotopes as a function of position through the fuel thickness. Mass spectrometry cannot provide structural details such as grain boundaries and stacking faults available to Transmission Electron Microscopy (TEM), but would give elemental and isotopic distributions with sub-millimeter resolution much earlier in the spent fuel timeline.

1.5 Planned Measurements

The purpose of this work is to measure the concentrations and isotopes ratios of the NIST glasses and related standards within $\pm 2\%$ of declared values, then apply these results to confirm the LANL neutron tomography study (Losko et al., 2014) of surrogate fuel pellets. If successful, this can be extended to standoff ablation of fuel pins, TRISO particles, and other highly active sources for in situ ablative mass spectrometry.

The goal of the work is to develop a standoff laser ablation mass spectrometry system for the interrogation of spent nuclear fuel and other hazardous materials. The approach is to use a fiber-transmitted femtosecond laser due to the unique advantages of ultrashort pulses in providing clean ablation. The fiber cable can be moved in space to ablate a volume of material. Gas flow (typically helium) would transport the ablated material into the plasma torch of an ICP-MS system, which would generate ions that can be filtered by mass-to-charge ratio and detected. Isotope ratios, absolute concentrations, and fission product identification can be accomplished as a function of position within the sample. The ability to conduct mass spectrometry on spent fuel remotely would allow more precise determination of specific fission products within the fuel pin. This is in contrast to more traditional ICP-MS where the fuel is dissolved, e.g. in nitric acid, and then analyzed in liquid form. The spatial resolution of the analysis would be limited by the spot size of the laser and the depth of ablation. The laser spot size is determined in large part by the characteristics of the fiber optics. The depth of ablation is a function of the material-specific work function, surface condition, and laser power.

1.6 Possible configuration for standoff laser ablation

By exposing only the fiber and terminal optics to the radiation field of the sample and conducting the analysis in a small volume, the ablated material can be transported to the mass spectrometer and analyzed without endangering personnel. If the fuel were cut into disks through the long axis, the fuel could be sampled from the central axis outward, providing important information about the position of fission products as a function of radius through the fuel. As burnup increases, the fuel structure becomes more complex and differentiated, with a central void forming at the core with significant cracking due to thermal expansion and a complex grain structure forming at the outer edge due to enhanced fission, a function of the average penetration depth of neutrons entering the fuel.

1.7 Simplified calculation of Pu production in LWR

The following calculation of Pu formation provides a sense of how different elements can grow in over time.

Given:

Density $\rho_{238} = 19\ \frac{\text{g}}{\text{cm}^3}$
Number density $= 19\frac{\text{g}}{\text{cm}^3} \cdot \frac{6.02 \cdot 10^{23}}{\text{mol}} = 4.8 \cdot 10^{22}$ atoms of ^{238}Pu
Capture cross-section $\sigma_{\text{U}_{238}} = 2.7$ x 10^{-24} cm^2
Reactor Flux $\phi = 10^{13}\frac{\text{n}}{\text{cm}^2 \cdot \text{s}}$
Pu production rate $= \text{N}\ \sigma\phi = 1.3$ x $10^{12}\frac{\text{atoms}}{\text{cm}^3 \cdot \text{s}}$

The reaction proceeds as:

$$^{238}\text{U}(\text{n},\gamma)^{239}\text{U} \tag{1.1}$$

$$^{239}\text{U} \rightarrow ^{239}\text{Np} + \beta^- + \bar{\nu} \tag{1.2}$$

$$^{239}\text{Np} \rightarrow ^{239}\text{Pu} + \beta^- + \bar{\nu} \tag{1.3}$$

Allow the reactions to occur inside a cylindrical region of a reactor at a radius from the central axis of 1 meter, in a core 2 meters high. This is a very rough approximation that neglects the fact that neutron capture on uranium will occur throughout the radius of the core (an underprediction), but also neglects the scatter events in which neutrons strike ^{235}U atoms but are not captured. The radial surface area of this cylinder is then the height by the circumference: 200 cm $\cdot\ 2\pi \cdot 100\,\text{cm} = 4\pi \cdot 10^4$ cm^2. Now consider Pu production over the cylindrical area after one year of reactor operation:

1.3 x $10^{12} \frac{\text{atoms}}{\text{cm}^2 \cdot \text{s}} \cdot 4\pi \cdot 10^4$ cm$^2 \cdot 3.15\text{x}10^7 \frac{\text{s}}{\text{year}} = 5\text{x}10^{24}$atoms of Pu per year, assuming 100% efficiency in β decay to Pu. This gives:

5 x $10^{24} \cdot \frac{239\text{g}}{6.02\text{x}10^{23}} \simeq 2\text{x}10^3$ grams per year, or roughly 2 kg, a reasonable value.

The preceding analysis shows the importance of rapidly analyzing spent nuclear fuel. This approach to the characterization of spent fuel can improve fuel performance and forensic analysis while building 3-D data sets of mass spectra comparable to neutron tomography. While small-scale analysis with, e.g., TEM, and large-scale analysis such as EDX are robust, the medium scales suffer from a lacuna of techniques. The small-scale techniques cannot cover large areas in reasonable time and the large-scale techniques lack the spatial fidelity (Hosemann, 2018).

1.8 Research Hypothesis

Femtosecond laser ablation mass spectroscopy could be a powerful tool to investigate the isotope distribution in matter. Because no vacuum is required and it has a small footprint, it can be a mobile and powerful tool to examine material in the field. The fact that it is laser driven allows investigation of harmful materials encapsulated in a transparent case. This makes it an ideal technique to investigate unknown and potentially hazardous materials in the field such as fresh or spent fuel pellets with unknown isotope ratios and content. However, in order to rely on it and use it on nuclear materials it is essential to know with what certainty one can determine isotope ratios and if the form and shape of nuclear fuel change the outcome of the measurement. The work here aims to prove that LAMS can provide reliable elemental and isotopic information on fresh and spent fuel pellets suitable for nuclear materials research. Furthermore, this effort aims to demonstrate that LAMS provides high local precision in all three coordinates regardless of the material or shape investigated. This work shows that LAMS is comparable to SEM/EDS surface measurements and can identify local chemical composition with the additional benefit of isotopic composition on round surrogate fuel pellets previously investigated using neutron time-of-flight resonance tomography. The work further shows that the third dimension (depth) is accessible and isotopic and elemental information can be obtained as a function of depth. This is demonstrated on TRISO surrogate fuel forms.

A secondary effort is to determine the usefulness of LAMS for finding fission products as they move through TRISO particles. An extensive body of work exists regarding fission product diffusion through SiC layers in TRISO. A brief literature review indicates that minor variations in SiC microstructure can have a strong influence on noble metal transport through SiC. Further, chemical interactions are likely between Pd and SiC (Gentile et al., 2015). While other techniques such as neutron tomography can provide 3-D elemental infor-

mation, they lack good isotopic resolution and, in the case of neutron tomography, require analysis at a neutron spallation source. For both TRISO and PWR fuel, laser ablation mass spectrometry represents a local optimum in terms of cost, analysis time, spatial and isotopic data, ease of use, and portability.

Chapter 2

Fundamentals

2.1 Mass Spectrometry

Mass spectrometry has grown steadily over the years from its easrliest form as a parabola spectrograph, built by J. J. Thompson in 1912. Most mass spectrometers were based on magnetic separation of ions moving through a vacuum. Wolfgang Paul developed a quadrupole ion guide that was much smaller than the magnetic systems. The quadrupole had the advantages of smaller overall footprint and reduced vacuum requirements. Modern sector mass spectrometers have a large electromagnet that can scan slowly through the mass range. However, this is difficult to do so the magnets are typically held at a high fixed field strength and electric lenses are used to shape the ion beam. Quadrupoles are small by comparison and don't require large magnets, but they lose resolution and detection limit as a result. The trade-off is considered worthwhile because ICP-MS is much faster and less expensive than sectors, so sectors are reserved for the most stringent analysis requirements and the most exacting isotope ratio analyses. ICP allows longer dwell time because the flow rate of argon through the torch is slow enough that ions spend up to milliseconds in the plasma (a long time compared to other techniques). The higher temperature is a result of argon's first ionization energy. He and Ne have higher first ionization energy but are more expensive, so Ar is the most commonly used gas. Incremental progress was made over a few decades until ICP was applied to the quadrupole mass spectrometer. ICP allowed ionization of almost all elements in the periodic table because of the high temperature and relatively long dwell time. The last crucial development in ICP mass spectrometry was the sampler and skimmer cone configuration. These two cones of metal have tiny pinholes at the center through which the plasma passes from atmospheric pressure to the vacuum of the mass spectrometer. Once inside the mass spectrometer, the ions enter the quadrupole itself and undergo separation according the mass-to-charge ratio of the ion. This allows the sample to be ionized at atmospheric pressure and then quickly pass to high vacuum, where isotope separation occurrs in the quadrupole. The list below gives the timeline of key mass spectrometry developments.

Key Points in the History of Mass Spectrometry

- 1913 - J. J. Thompson separates ions by mass using parabola spectrograph (J. Thompson, 1913)
- 1918 - Dempster develops magnetic sector concept with isotope ratio measurements on lead (Dempster, 1918)
- 1932 - E. O. Lawrence develops cyclotron (Lawrence & Livingston, 1932)
- 1932 - Smyth and Mattauch develop electric mass separation (Smythe & Mattauch, 1932)
- 1934 - Mattauch and Herzog develop double focusing (Mattauch & Herzog, 1934)
- 1940 Nier develops high precision mass spec (Nier (1940); Nier (1947))
- 1953 - Paul and Steinwedel develop quadrupole mass analyzer and quadrupole ion trap. (Paul & Steinwedel, 1953)
- 1964 - Greenfield uses ICP to form ions (Greenfield et al., 1964)
- 1974 - ICP Optical Emission Spectroscopy (Scott et al., 1974)
- 1976 - First commercial ICP for Optical Emission (Dawson, 1976)
- 1980 - Houk mates ICP to MS, achieves high vacuum using sample and skimmer cones (Houk et al., 1980)
- 1983 - Perkin Elmer develops first commercial ICP-MS
- 1985 - Laser Ablation-ICP-MS (Gray, 1985)

2.2 Laser Operation

Figure 2.1 shows the general principle of Chirped Pulse Amplification in which the beam is stretched in wavelength, amplified, and then recompressed. The exit pupil of the laser is large in order to keep the beam below the ablation threshold of the optics. The beam is focused onto the target using a Schwarzschild optic.

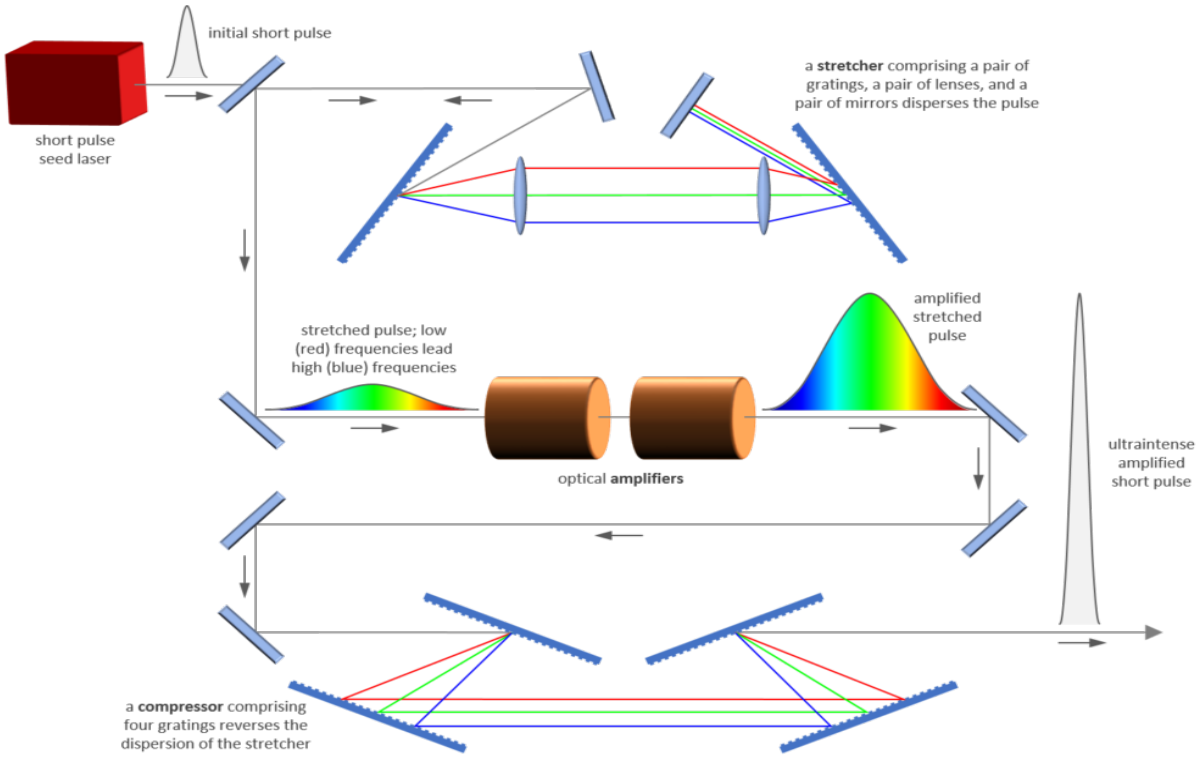

Figure 2.1: General schematic of Chirped Pulse Amplification, used with kind permission of Plymouth Grating Laboratory, Inc.

In 1985, Donna Strickland, with her PhD advisor Gérard Mourou (Strickland & Mourou, 1985), developed Chirped Pulse Amplification (CPA), a method of amplifying pulses by first stretching them in the frequency domain, amplifying them, and then recompressing the pulse (Nobel Prize, 2018). This allowed the generation of high-intensity pulses that would have otherwise exceeded the damage threshold of laser optics and in doing so accessed a new regime of physics. Because femtosecond laser pulses have a shorter duration than the phonon frequency (Section 2.14) of known materials, the energy of femtosecond and shorter pulses is not significantly dissipated (Le Harzic et al., 2002). This results in ablation or welding with a very small Heat Affected Zone (HAZ), stronger welds, and cleaner ablation. A Spectra-Physics Ti:Sapphire IR femtosecond laser was used to perform the work (Figure 2.2).

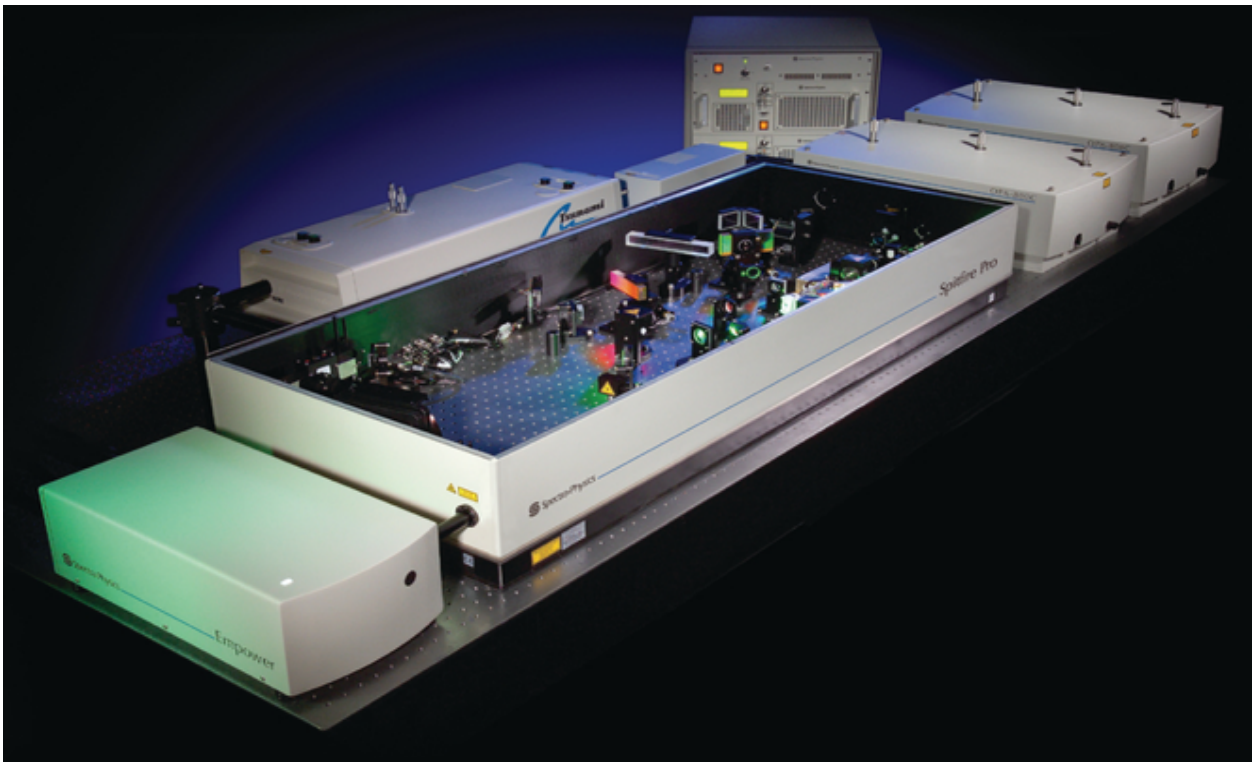

Figure 2.2: Layout of a Spectra-Physics femtosecond laser similar to that used in the experiments.

2.3 Optical Aberrations

Attendant to laser operation are optical aberrations. Aberrations can be divided into two main classes, chromatic and achromatic. Chromatic aberrations arise as a result of wavelength dependence and include transverse and longitudinal aberrations. Aberrations defocus the laser and reduce ablation efficiency. Low-order corrections are well established, after (Dereniak & Dereniak, 2008).

Monochromatic aberrations arise from the structure of the optics themselves, fundamentally a result of using simplified (paraxial) models. They include tilt, defocus, sphericity, coma, astigmatism, field curvature, and distortion, as shown in Figure 2.3. Ideally, aberrations are minimized and the system produces diffraction limited images. The diffraction limit defines the smallest resolvable object and is given by Equation 2.1.

$$\mathrm{d} = \frac{\mathrm{f} \cdot \lambda}{\mathrm{n} \cdot \mathrm{b}} \tag{2.1}$$

For:

d = Length of the smallest object that may be resolved [m]
f = Focal length [m]
λ = Laser wavelength [m]
n = Refractive index (air = 1.00)
b = Beam diameter [m]

A shorter wavelength is favored for a smaller diffraction limit. The diffraction limit is important to consider when choosing a laser system. If the purpose is to ablate the smallest area possible, such as when trying to bridge the gap between nanoscale and macroscale, then the diffraction limit will be an important guide. If the purpose is large-scale ablation, then the diffraction limit is not a driving factor. Another limit is bandwidth. Broadband capability is a factor because, by the properties of the Fourier Transform, the shorter the pulse duration in time, the wider the frequency content required to generate the pulse.

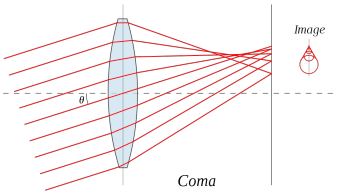

(a) Coma arises because the object lies off the optical axis. The effect is that the image is distorted in one direction.

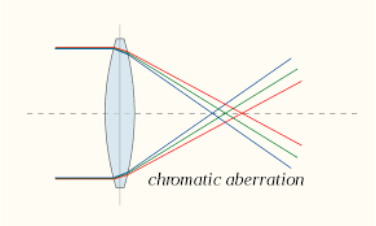

(b) Chromatic aberration occurs because each color (i.e., frequency) of light has a slightly different refractive index and is bent to a different angle.

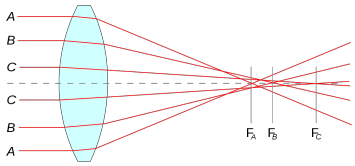

(c) Spherical aberration arises because the sphere is not the correct shape to focus light to a point. This aberration is correctable by sophisticated but expensive lens grinding and is often tolerated because of expense.

Figure 2.3: Common optical aberrations in laser optics (Paschotta, 2008). The Schwarzschild optic avoids chromatic and spherical aberrations because it reflects rather than refracts light.

Figure 2.4 shows several important parameters defined at the beam waist, the narrowest point of focus. From the relationships in Figure 2.4, to minimize the laser spot size, use the shortest focal length and shortest wavelength with the largest aperture diameter possible.

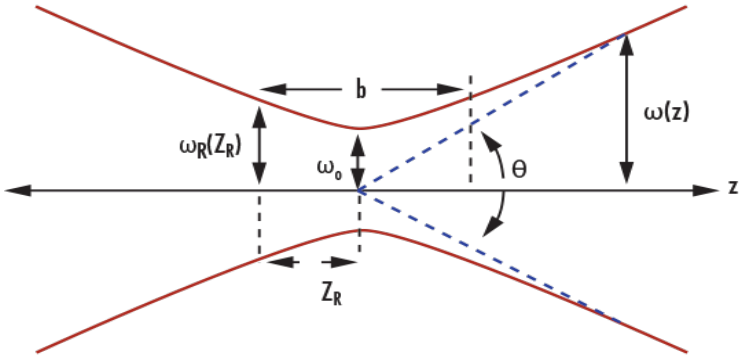

Figure 2.4: Illustration of a laser beam at the waist (Paschotta, 2008). Reprinted with permission.

In Figure 2.4:

$\omega_o = \frac{2\lambda}{\pi \cdot \theta}$ = Beam waist [m]
b = Depth of focus [m]
$Z_R = \frac{\pi \cdot w_o^2 \cdot n}{\lambda}$ = Rayleigh range [m]
n = Refractive index of medium
θ = Angular spread [degrees]

A comparison of the Rayleigh length Z_R between infrared and ultraviolet wavelengths shows that shorter wavelengths have a longer Rayleigh length:

$$Z_{R,\,IR} = \frac{\pi \cdot \omega^2}{\lambda} = \frac{\pi \cdot (20\text{x}10^{-6})^2}{800\text{x}10^{-9}} = 0.0016 \text{ m} = 1.6 \text{ mm}$$

$$Z_{R,\,UV} = \frac{\pi \cdot (20\text{x}10^{-6})^2}{193\text{x}10^{-9}} = 0.0065 \text{ m} = 6.5 \text{ mm}$$

The Rayleigh length for a UV laser is approximately four times longer than for an IR laser. This should be considered when choosing a wavelength for laser ablation. For example, a requirement for precise depth control would bias towards the infrared. This must be balanced against the diffraction limit, which is smaller for shorter wavelengths. Also, mass fractionation is found to decrease with decreasing wavelength. The beam waist is significant because it is a primary factor in determining the Rayleigh length.

2.4 Laser Ablation

Direct injection of laser-ablated aerosols into an ICP-MS device began with Gray in 1985 (Gray, 1985), who followed Thompson's first use of laser ablation for optical emission spec-

troscopy (Thompson et al., 1981). Laser ablation has found wide use in the geologic sciences, where the ability to directly sample difficult-to-digest minerals offers time and cost savings. The trend in ablation has been toward shorter pulse duration (termed "pulse width"), with a new regime of physics in the low picosecond to femtosecond range. This is because the duration of the laser pulse falls below the phonon relaxation time of most materials.

Maxwell's differential wave equations for propagation *in vacuo* (Maxwell, 1865), cast in the manner of (Silfvast, 2004):

$$\nabla \cdot \mathbf{E} = 0 \tag{2.2}$$

$$\nabla \cdot \mathbf{B} = 0 \tag{2.3}$$

$$\nabla \times \mathbf{E} = -\frac{\partial \mathbf{B}}{\partial \mathrm{t}} \tag{2.4}$$

$$\nabla \times \mathbf{B} = \mu_o \epsilon_o \frac{\partial \mathbf{E}}{\partial \mathrm{t}} \tag{2.5}$$

For:

∇ = Three-dimensional gradient operator
$\mathbf{E}$ = Electric field
$\mathbf{B}$ = Magnetic flux
μ_o = Vacuum permeability
ϵ_o = Vacuum permittivity

Maxwell's wave equations for propagation in material involve the following quantities:

ρ = Charge density [charge per unit volume]
$\mathbf{P}$ = Polarization [electric dipole moment per unit volume]
$\mathbf{J}$ = Current density [current per unit area]
$\mathbf{D}$ = Electron displacement

The Lorentz force and polarizability describe the electromagnetic response of a material to first order. For isotropic materials, ϵ and μ are scalars, but for anisotropic materials, they are tensors. Because materials are usually dispersive, these two quantities are also frequency dependent. Note that Maxwell's equations are not exact, but the classical limit of Quantum ElectroDynamics (QED). In free space, $\mathbf{D} = \epsilon_o \mathbf{E}$. In isotropic media, $\mathbf{D} = \epsilon \mathbf{E}$. In anisotropic materials, $\mathbf{D} = \epsilon \mathbf{E} + \mathbf{P}$, with $\mathbf{P} = (\epsilon - \epsilon_o)\ \mathbf{E}$ (Silfvast, 2004).

We can define a new quantity $\chi = (\frac{\epsilon}{\epsilon_o} - 1)$ to capture the nonlinear optical response of anisotropic materials. χ is scalar for isotropic materials, but when expanded in series for

anisotropic materials, it describes nonlinear optical effects.

χ is a useful parameter for optical frequencies because it captures nonlinear behavior. χ is scalar for isotropic materials and when expanded in series describes nonlinear optical effects. Maxwell's equations for propagation in material take the following modifications:

$$\nabla \cdot \mathbf{E} = -\frac{1}{\epsilon_o} \nabla \cdot \mathbf{P} \tag{2.6}$$

$$\nabla \cdot \mathbf{B} = 0 \tag{2.7}$$

$$\nabla \times \mathbf{B} = \epsilon_o \frac{\partial \mathbf{E}}{\partial \mathrm{t}} + \frac{\partial \mathbf{P}}{\partial \mathrm{t}} + \mathbf{J} \tag{2.8}$$

$$\nabla \times \mathbf{E} = -\mu_o \frac{\partial \mathbf{B}}{\partial \mathrm{t}} \tag{2.9}$$

Given that charge density ρ is zero in dielectric materials, these four expressions show the terms that arise in response to propagation through material, namely polarization $\mathbf{P}$ and charge current $\mathbf{J}$. $\mathbf{P}$ arises due to local charge buildup in dielectrics and describes optical effects such as dispersion, absorption, and double refraction. $\mathbf{J}$ arises from the flow of current through conducting materials and explains phenomena such as the high absorptivity and reflectivity of metals. Semiconductors exhibit properties of both conductors and dielectrics, which complicates their analysis. Femtosecond lasers operate on timescales faster than these optical effects to first approximation, but effects such as crystal orientation, polarizability of material and polarization of incoming laser pulses may have measurable effects on the bulk scale. The details are beyond the scope of this work, but subtle effects such as (Feng, 2022) merit further study.

2.5 Ionization Energy

Two models have been used to explain laser ablation. The Drude model (Drude, 1900) treats electrons as tiny spheres among a matrix of immovable atomic nuclei. The free electron model (Sommerfeld, 1928) is preferred because it incorporates quantum mechanics into the Drude model to give better explanatory power of electron behavior in a laser pulse:

$$\mathrm{E}_{\text{Kinetic Energy of e}^-} = \mathrm{h}\nu_{\text{X-Ray}} - \mathrm{E}_{\text{Binding Energy of Sample}} - \Phi_{\text{Work Function}} \tag{2.10}$$

2.6 Calculation of ablation energy based on crater volume and laser energy

Femtosecond lasers are known to ablate with high efficiency. This is attributed to the laser pulse being of shorter duration than the phonon frequency of most materials and demonstrating generally cleaner ablation, e.g. (Le Harzic et al., 2002). Using an approximate ablation crater diameter of 40 μm and crater depth of 20 μm, we can calculate the energy per atom needed for ablation of copper:

Ablation volume $= \pi \cdot \mathrm{r}^2 \cdot \mathrm{h} = (\pi \cdot 2\mathrm{x}10^{-3}\ \mathrm{cm})^2\,(2\mathrm{x}\,10^{-3}\,\mathrm{cm}) = 2.51\ \mathrm{x}\ 10^{-8}\ \mathrm{cm}^3$

Applying values:

$2.51\ \mathrm{x}\ 10^{-8}\ \mathrm{cm}^3 \cdot \frac{8.96\ \mathrm{g}}{\mathrm{cm}^3} = 2.25\ \mathrm{x}\ 10^{-7}\ \mathrm{g}$ ablated per pulse

$2.25\ \mathrm{x}\ 10^{-7}\ \mathrm{g} \cdot \frac{\mathrm{mol}}{63.55\ \mathrm{g}} \cdot \frac{6.02\ \mathrm{x}\ 10^{23}}{\mathrm{mol}} = 2.1\ \mathrm{x}\ 10^{15}$ atoms per pulse

$\frac{10^{-3}\ \mathrm{J\ per\ pulse}}{2.1\ \mathrm{x}\ 10^{15}\ \mathrm{atoms\ per\ pulse}} = 4.69\ \mathrm{x}\ 10^{-19}$ J per atom

$4.69\ \mathrm{x}\ 10^{-19}$ J per atom $\cdot \frac{\mathrm{eV}}{1.602\ \mathrm{x}\ 10^{-19}\ \mathrm{J}} = 2.93\,\frac{\mathrm{eV}}{\mathrm{atom}}$

This result is slightly below the work function of $\sim 4.5\ \frac{\mathrm{eV}}{\mathrm{atom}}$, but is easily within the ablated volume estimation error.

Calculation of free electron number

To determine whether there is a free electron available to begin avalanche breakdown, consider the simplified Saha equation, which assumes only one energy transition and no degeneracy:

$$\frac{\mathrm{n_e^2}}{\mathrm{n_o}} = \frac{2}{\lambda^3}\frac{\mathrm{g_1}}{\mathrm{g_0}}\,\mathrm{e}^{\left[\frac{-\epsilon}{\mathrm{k_B T}}\right]} \tag{2.11}$$

For:

$\mathrm{n_o}$ = Number density
$\mathrm{n_e}$ = Electron density
g = Quantum degeneracy, in which two or more states have the same Hamiltonian
ϵ = First ionization energy [eV]

$$\lambda = \sqrt{\frac{h^2}{2\pi m_e k_B T}} = 1.36 \text{ x } 10^{-7}\text{m at 300 K} \tag{2.12}$$

Then, assuming no degeneracy:

$$\frac{2}{(1.36 \text{ x } 10^{-7})^3} \cdot 1 \cdot e^{-\left[\frac{1.31\text{x}10^{-18}}{1.38\text{x}10^{-23} \cdot 300}\right]} = 3.0\text{x}10^{-117} \approx 0 \tag{2.13}$$

The result becomes greater than unity for temperatures above approximately 2,000 K. These high temperatures are partly the result of silicon's high ionization energy and partly because to the Saha equation applies to gases rather than solids. Nevertheless, it gives a zeroth-order expectation that no free electrons are extant in the material at the onset of ablation.

This leads to the question of how ablation begins, which is an area of active research. Multi-photon absorption probably contributes, given the high photon density in femtosecond pulses, but several IR photons would have to combine to achieve the ionization energy of Si. The intense electric fields (GV/m) of ultrashort pulses could also play a role.

Single pulse energy

The energy of a single pulse from a Spectra-Physics Ti:Sapphire 1 Watt femtosecond laser has a nominal wavelength of $\sim$ 800 nm. Using $c = \lambda\nu$:

$\nu = \frac{c}{\lambda} = \frac{2.99\text{x}10^8 \frac{\text{m}}{\text{s}}}{800\text{x}10^{-9}\text{m}} = 3.74\text{x}10^{14}\,\text{s}^{-1}$

Energy per photon = $h\nu = 6.626\text{x}10^{-34} \cdot 3.74\text{x}10^{14} = 2.48\text{x}10^{-19}$J

In eV: $2.48\text{x}10^{-19}\,\text{J} \cdot \frac{\text{eV}}{1.602\,\text{x}\,10^{-19}\,\text{J}} = 1.55$ eV.

For:

ν = Frequency of light
c = Speed of light
λ = Wavelength of light
h = Planck's constant

The energy concentration of a 1 W laser operating at 1 kHz repetition rate can be calculated for 1 mJ per pulse:

$$1\,\mathrm{W} = 1\frac{\mathrm{J}}{\mathrm{s}} \cdot \frac{\mathrm{s}}{1,000\ \mathrm{pulses}} = \frac{1\,\mathrm{J}}{1,000\ \mathrm{pulses}} = 1\frac{\mathrm{mJ}}{\mathrm{pulse}}$$

This yields $\frac{0.001\,\mathrm{J}}{\mathrm{pulse}} \cdot \frac{\mathrm{eV}}{1.602\,\mathrm{x}\,10^{-19}\,\mathrm{J}} = 6.24\mathrm{x}10^{15}\ \frac{\mathrm{eV}}{\mathrm{pulse}}$

For a spot diameter of 20 μm, area = $\pi \mathrm{r}^2 = \pi\ (0.002\ \mathrm{cm})^2 = 1.3\ \mathrm{x}\ 10^{-5}\ \mathrm{cm}^2$

Irradiance (Flux Density) = $\frac{\mathrm{J}}{\mathrm{cm}^2} = \frac{0.001\mathrm{J}}{1.3\,\mathrm{x}\,10^{-5}\mathrm{cm}^2} = 76.9\ \frac{\mathrm{J}}{\mathrm{cm}^2}$

Given silicon's 8.15 eV threshold, seven photons would have to combine at once to provide sufficient energy. This is extraordinarily unlikely, even at the high photon densities of laser pulses. Other factors such as nonlinear effects are under investigation (Feng, 2022).

Assuming that a free electron is available to begin the breakdown avalanche, the material is excited and ablated before phonons can carry away a significant fraction of the femtosecond laser. This is the key parameter that separates femtosecond lasers from longer duration systems. Transfer of energy to ions adjacent to the ablation site leads to ringdown through crystal lattice vibrations (phonon relaxation). This transfer of energy via the phonon lattice dissipates energy as heat, resulting in a Heat Affected Zone, melting, and splatter.

Ablation fractionation

(Mank & Mason, 1999) found that the geometry of the ablation crater controls sampling accuracy at depth. Elemental fractionation was observed with $\frac{\mathrm{depth}}{\mathrm{diameter}} > 6$. However, a larger crater diameter with sufficient power was found to reduce fractionation. No cleaning shots were used in this work but this could be an important step in future studies comparing cleaning shots to other surface treatments such as chemical or mechanical polishing followed by an acetone rinse.

The rate and amount of material ablated depend on many factors, including pulse energy, pulse duration, pulse repetition rate, spot size, transport gas flow rate, transport gas composition, crystal lattice type and orientation relative to the laser beam, and binding energy. These factors were largely already optimized or fixed for the experimental series and are treated topically in the mass spectrometry section. The matrix dependence of laser ablation signals has been a limiting factor in quantitative LA-ICP-MS. The commercial availability of femtosecond lasers may improve the situation if they can be shown to be free from or less prone to matrix fractionation effects (Miliszkiewicz et al., 2015). Detailed fractionation studies are beyond the scope of this work, but the results would interest a wide community.

This work used a Spectra-Physics Spitfire Femtosecond laser operated at 1 kHz repetition rate. The laser uses Chirped Pump Amplification (CPA) to amplify the high energy pulses without damaging the optics and Frequency Response Optical Gating (FROG) to measure the pulse width, which is faster than electronic response times. The output pulse width was on the order of 800 fs at 1 μJ.

The observed plasma over the sample during the experiments implies one or both of the following conditions:

1. The pulse duration of the laser is longer than the phonon frequency of the material.
2. The ablated material does not clear the beampath before the next pulse arrives.

Condition 2 is the more likely explanation. Though the calculation below shows an average velocity sufficient to remove material prior to the next pulse arriving, the actual velocities of individual aerosols will follow a Maxwellian distribution.

Ablated particle velocity

Given 1 mW per pulse and a cylindrical ablation volume of approximately 40 μm x 20 μm, the ablated volume is 2.51 x 10^{-8} cm^3 for copper metal. This corresponds to about 2.1 x 10^{15} atoms, as determined above. Then $\frac{10^{-3}\mathrm{J}}{2.1\mathrm{x}10^{15}\mathrm{atoms}}$ gives 4.8 x 10^{-19} $\frac{\mathrm{J}}{\mathrm{atom}}$, which converts to $\frac{4.8\mathrm{x}10^{-19}}{1.602\mathrm{x}10^{-19}}$ = 3 eV, implying that there is little energy left over to partition into kinetic energy of the ablated particles. However, even 1 eV of kinetic energy is sufficient to remove a nanoparticle of copper from the ablation region. Briefly, for a copper particle of 500 nm diameter, $\mathrm{v} = \sqrt{\frac{2\mathrm{E}}{\mathrm{m}}} = \sqrt{\frac{2 \cdot 1.602x10^{-19}}{5.86x10^{-22}\mathrm{kg}}} = 23\ \frac{\mathrm{m}}{\mathrm{s}} = \frac{2.3\mathrm{cm}}{\mathrm{ms}}$. The Rayleigh length for this optical system is on the order of millimeters and the interval between pulses is one millisecond, so there should be time for the bulk of ejecta to escape before the next pulse arrives. However, the velocities will follow a Maxwellian distribution and the particle sizes will vary. Thus some fraction will be within the Rayleigh length during the following pulse, explaining the observed plasma.

The following calculation of phonon frequency ω_D in copper illustrates the effectiveness of femtosecond lasers in depositing energy faster than phonons can carry it away:

$$\omega_D = \nu_s \frac{\pi}{\mathrm{a}} \tag{2.14}$$

Applying values:

5,000 $\frac{\mathrm{m}}{\mathrm{s}} \cdot \frac{\pi}{2.6\,\mathrm{x}\,10^{-10}\,\mathrm{m}}$ = 6.04 x 10^{13} s^{-1}

For:

ν_s = Speed of sound in the material [m/s]
a = Lattice parameter, the interatomic spacing of the material [m]

Taking the inverse gives 1.66 x 10^{-14} s, which is on the order of femtoseconds. This calculation shows that any laser pulse faster than this frequency will not transmit energy to adjacent atoms before the pulse ends. Energy will certainly be transferred as the ablated material radiates and adjacent material responds to the electromagnetic field, but phonon transfer will initially be limited.

2.7 Motivation for laser analysis

(Schaltegger et al., 2015) described key applications of U-Th-Pb laser ablation MS in geochemistry. While isotope dilution Thermal Ionization Mass Spectrometry (TIMS) provides the best isotope ratios, it is a bulk technique in which all spatial information about the sample is lost. SIMS and NanoSIMS provide the highest spatial resolution, but must have high vacuum with matrix matched standards and are almost always much more time consuming than laser ablation. Laser ablation fills a key niche between TIMS and NanoSIMS by providing spatial resolution to micrometer level, reasonable isotopic precision, and dramatically faster analysis.

(Puranen et al., 2017) developed a laser ablation ICP-MS system for analyzing Li and B in a fuel pin, but with a nanosecond laser. They identified ^{7}Li as the source of corrosion in a bent fuel pin using standoff laser ablation in a hot cell. Their work highlights the potential for analysis of hot fuel in a standoff configuration. This example also shows the benefits of LAMS since it can find elements that are not easy to identify using SEM-EDX, for example. The present effort builds upon (Puranen et al., 2017) on fuel pins to include isotope ratios as a measure of fuel burnup, the most recent uranium separation, and possibly the fuel source. Ca, Fe, W, Zr, Sn, Cr, Mo, Ni, V, and Cu are important indicators between natural and enriched fuel and (Marks, 2021) leads an effort to determine the trace element fingerprints of various uranium sources. Mass spectrometry is a key method in determining the trace element composition of various uranium samples. NIST glasses are reported to contain 72% SiO_2, 14% Na_2O, 12% CaO, and 2% Al_2O_3, providing a ready source for several of the background signals under ablation. Many additives are used to improve fuel performance. Development of a femtosecond LAMS system for fuel analysis could improve our understanding of the distribution of these elements in spent fuel and is the subject of this effort.

2.8 Advantages of laser ablation compared to other techniques available

Many techniques available today allow spatially resolved analysis of isotopes in matter. Starting at the smallest scale, Atom Probe Tomography addresses isotopes atom by atom with 60% efficiency. However, the volume is limited to 100 x 100 x 1,000 nm and the samples have to be in the form of needles, leading to time-consuming and costly analysis. SIMS can analyze down to the nanometer scale but requires strong vacuum and is time-consuming for large sample surface areas. Time-of-Flight Neutron Resonance Tomography has a large beam area of several square millimeters and requires a neutron spallation source with high cost and low throughput. These factors illustrate the valuae of LAMS to provide both isotopic and concentration data at the micrometer level rapidly and at less cost than other techniques.

Laser ablation has high sensitivity and is much easier than nitric acid digestion for highly radioactive spent fuel. The digested sample is often heavily diluted and spatial information is lost. Various complementary methods to ICP-MS, such as chromatography can be used to purify and concentrate analytes prior to ionization in a mass spectrometer. However, this is labor-intensive compared to laser ablation.

Ultra-high-resolution techniques such as electron ptychography (Feng, 2022) allow unprecedented resolution at the atomic scale. By using sophisticated machine learning algorithms and various time-frequency transforms, such as the Wigner Distribution Function (Wigner, 1932), ptychography can produce images at a resolution of less than half an Angstrom. However, these techniques apply only to samples a few atoms thick. Though not as precise as electron ptychography or Transmission Electron Microscopy, laser ablation spots can sample down to micrometers, sufficient to interrogate individual crystals in some instances. LAMS also offers isotopic information, which most other techniques cannot match. Laser ablation doesn't require the high vacuum of SIMS and does not contaminate the sample as with static SIMS. Static SIMS points a beam of ions such as Cs^+ at the target region. This beam of ions bombards the area, knocking free and ionizing the elements already present. Over time, however, the Cs^+ ions will accumulate in the sample and begin to contaminate the analysis signal. In contrast, an initial cleaning pass is usually sufficient surface preparation for quantitative laser ablation. Lastly, laser ablation offers the possibility of remote sampling of hot fuel pins in a shielded ablation cell. This could provide isotopic and 3-D spatial information about where particular isotopes are found within fuel after irradiation. While neutron resonance imaging offers similar capability, the facilities where it can be done are large industrial locations requiring heavy infrastructure support. By contrast, laser ablation mass spectrometry systems can be configured for portability in a vehicle, aircraft, or vessel. Applications in a hot cell would require shielding of elements such as lenses and fiber optic lines, but such measures are within present engineering capabilities.

NanoSIMS requires matrix matched standard and high vacuum, and slowly contaminates sample with the ion beam, though this is ameliorated by dynamic SIMS which drills into the material. Electron Energy Loss Spectroscopy, TEM, and Atom Probe Tomography all give higher resolution than NanoSIMS. Electron tomography stacks 2-D images to obtain a 3-D representation of the sample. (Jiang et al., 2018) obtained sub-Angstrom resolution on 2-D materials using Scanning Transmission Electron Microscopy (STEM). While the state of the art for the last decade has been sub-angstrom, the resolution and diversity of information has increased. Nano-SIMS offers nanoscale resolution, and TIMS provides superior isotope ratios. However, TIMS and solution mass spec are both time consuming and limited in their ability to characterize potential small-scale isotopic heterogeneities present in the samples, which are of great interest for some applications (e.g. seasonal variability of pH in tropical corals (Pessoa et al., 2021)) because spatial data are lost. Laser ablation can probe the migration patterns of fission products in fuel pins. Some migrate to the center (equiaxed grains) and some migrate out (e.g. ^{110m}Ag). This is one of the advantages of laser ablation.

The suite of elements of interest to nuclear fuels and nuclear forensics covers most of the periodic table, from beryllium to plutonium. Mass spectrometry offers one of the widest ranges of analysis of any technique. Though LA-ICP-MS cannot at present match the spatial precision of SIMS or the isotopic precision of TIMS, it represents a powerful optimization of many competing factors including cost, analysis time, spatial precision, elemental range, moderate vacuum requirement, and continuous flow operation. Examples of elements include Zr, widely used in nuclear reactors because of its low cross-section, and Mo, which has a higher melting point and thermal conductivity than Zr. Lower abundance isotopes of Mo have low neutron cross-sections, comparable to Zr, and are enriched for use in Russian reactors (Smirnov et al., 2015). Nd is produced in linear proportion to burnup in power reactors and is an important indicator in nuclear forensic applications (J. Kim et al., 2015). Tungsten is another key element in nuclear applications (Hickman et al., 2014). Tungsten coatings on UO_2 can reduce fuel loss. (Schnitzler & Borowski, 2012) list tungsten, molybdenum, rhenium, and tantalum as refractory metals of choice for nuclear applications. Be is often used as a radial neutron reflector. Boron carbide, usually enriched in ^{10}B, serves as a neutron absorber. Gadolinium can be mixed into fast reactor fuel, such as the blend 60% UO_2, 34% W, and 6% Gd_2O_3 as a burnable poison.

A final argument for standoff laser ablation in fuel analysis comes from looking at the process of sample preparation for aqueous mass spectrometry, which is much more time-consuming than laser ablation. Table 2.1 lists the steps for aqueous sample preparation (known as deconsolidation, e.g. Scates et al. (2007)). The steps are time and resource intensive compared to essentially one step for laser ablation. These deconsolidation steps, in combination with the labor intensive processes of NanoSIMS operation, provide motivation for the rapid analysis possible with LA-ICP-MS.

Deconsolidation Steps (Harp et al., 2014)
1. Electrolytically deconsolidate the compact
2. Leach in nitric acid
3. Oxidize to remove pyrolytic carbon
4. Perform second acid leach
5. Crush particulates to expose fuel
6. Oxidize to convert insoluble carbides to soluble oxides
7. Acid leach the residue

Table 2.1: The many steps required to prepare a fast reactor compact for aqueous ICP-MS analysis.

Secondary Ionization Mass Spectrometry with nanometer spatial resolution, or NanoSIMS, is a close competitor to LA-ICP-MS. Dynamic SIMS allows the operator to drill into material and is the most sensitive method. However, NanoSIMS is subject to several issues, as outlined in Table 2.2.

Considerations for NanoSIMS
1. Primary beam mixes with sample; reaches equilibrium unless used in dynamic mode
2. Chemistry of beam and target are important to ion yield
3. Must use matrix matched standards
4. Yields for mono-, di-, and tri-atomic molecules differ because of increasing degrees of freedom
5. Yield: Monatomic > Diatomic > Triatomic

Table 2.2: NanoSIMS is a powerful analytical technique but is limited to comparatively small search areas. The incident beam consists of atoms, not photons, so the sample may become chemically contaminated over time, especially if the incident beam remains in the same location.

The NanoSIMS considerations in Table 2.2 lead back to the issue of the most effective technique for a given application. Table 2.3 provides some attributes of common analytical techniques and allows comparison among several techniques. One disadvantage of LAMS is the inability to determine crystal structure or grain boundaries, for example.

2.9 Importance of position control

The Aerotech three-axis stage has position control to $\pm$ 0.10 μm accuracy and is programmed via G-Code. Samples are placed within the ablation cell and brought into focus along the

Instrument	**Advantages**	**Disadvantages**
Resonance Ionization Mass Spectrometry	High Sensitivity	High Vacuum
ICP-MS	Isotopics	Low Res, Imageless but x-y-z ablation
Thermogravimetry	Small Sample Size, Chem info, Kinetics	Destructive
X-Ray Diffraction	Crystal structure	Poor LOD, Must be powdered
X-Ray Photoelectron Spectroscopy	Easy to use, $E_k = h\nu - E_B$.	LOD 1 at%
Electron Diffraction	Crystal structure	No localized chemical info due to probe size
Polarized light (laser)	Crystal structure, Thickness	Amorphous materials
X-Ray Fluorescence (2^0 X-Ray)	Element specific	
Selected Area Electron Diffraction	Small spot size, crystal structure	
Transmission Electron Microscopy+EDS/WDS/EELS	Ultrahigh spatial resolution	Weak detection limit
Synchrotron Spectroscopy	High Resolution	Expensive
Soft X-rays (K-Edge)	Cost effective	Lower resolution than high energy
Scanning Transmission X-Ray Microscopy (STXM)	Redox chemistry	U often below LOD
X-Ray Absorption Near-Edge Spectroscopy (XANES)	Broadly applicable to almost any element	Poor LOD, only $\frac{1}{e}$ depth
Autoradiography	Easy to implement	Takes time for low activity samples
Ptychography	Sub - Å resolution	Computationally intensive
X-Ray Computed Tomography	3-D information	Large samples have poor resolution
Neutron Activation Analysis	Contamination insensitive	Slow (up to weeks)
Precession Electron Diffraction	Ultra high spatial resolution (sub Å)	Data interpretation still in refinement
Laser Ultrasonic Assessment	Insensitive to surface roughness	LOD limited by shot noise
Transimission Kikuchi Diffraction	High resolution, grain boundary discrimination	Small scanning area or long scan time
Secondary Ion Mass Spectrometry	Excellent LOD	2-D, interferences, time
Resonance Ionization Mass Spec	Background rejection, high signal	Must tune to Ag
Energy Dispersive X-Ray Spectroscopy	Rapid, 2-D, chemical info	Poor LOD
Alpha Particle Channeling Spectroscopy	Characteristic energies	Limited to alpha emitters
Raman	SiC polytype	Limited spatial res, Surface only
EBSD	SiC polytype	Near surface only
Rutherford alpha backscatter	Limited depth profiling (nm)	Limited chemical info
Atom Probe Tomography	Ultrahigh spatial resolution	Small search area
3-D electron tomography	Morphology, High resolution	Small area, time consuming

Table 2.3: Attributes of various analytical techniques.

z-axis. The stage is moved either continuously or by steps to create ablation tracks across a sample surface. The beam focus is sensitive to vertical change and defocuses on the order of one μm of vertical movement. (Schaltegger et al., 2015) found that the ablation chamber configuration is important, but the ablation cell was commercially available and is not treated further. The rise time and washout time of the cell were satisfactory for these experiments as shown below in Figure 2.5.

2.10 Transport Characteristics

Material Transport

Ejected material is transported by the helium gas flow from the sample to the mass spectrometer. The flow calculations below indicate that the gas should be laminar and the transport characteristics provide a clean signal onset.

The helium gas flows directly into the glass torch, where it passes through the argon plasma and becomes ionized by the high temperature (on the order of 8,000 K). The ionization temperature of argon gas is 15.759 eV, corresponding to a temperature of 182,804 K. Other effects lower the plasma temperature from that expected by the individual ionization temperature. Once ionized, the particles pass through the sampler and skimmer cones and ion optics, including a chicane in the flight path to decrease background, through the quadrupole mass filter, and on to the detector.

Turbulence

Tygon tubing is smooth and chemically nonreactive by design (Saint-Gobain, 2019). Using the Reynolds number R_e to determine if the flow is turbulent (EngineeringToolbox, 2020):

$$\mathrm{R_e} = \frac{\rho \upsilon \mathrm{L}}{\nu} = \frac{0.1664 \cdot 82.8 \cdot 1}{2.0 \text{ x } 10^{-5}} = 688.9 \tag{2.15}$$

for:

ρ = Density of the fluid $\left[\frac{\mathrm{kg}}{\mathrm{m}^3}\right]$
υ = Velocity of the fluid with respect to the object $\left[\frac{\mathrm{m}}{\mathrm{s}}\right]$
L = Characteristic linear dimension [meter]; here, the tube diameter
ν = Dynamic viscosity of the fluid $\left[\frac{\mathrm{N \cdot s}}{\mathrm{m}^2}\right]$, $\left[\mathrm{N} = \frac{\mathrm{kg \cdot m}}{\mathrm{s}^2}\right]$

Turbulence sets in at approximately $R_e = 2,300$ (Schlichting & Gersten, 2017), so transport should be laminar. The sharp signal onset supports this. Fluid behavior is sensitive to the amount of disturbance prior to the pipe flow, and $\mathrm{R_e}$ has been measured as high as 20,000

before the onset of turbulence. Given the clear signal onset in the mass spectra and the polished nature of the inner tube wall designed specifically to enhance chemical transport, it appears that the transport characteristics are sufficient to provide useful data with sharp rise times and rapid washout. Because the transport is rapid compared to the sampling timescale of the mass spectrometer, the time between laser ablation and entry into the mass spectrometer can be neglected. The initial sampling method was to fire the laser every 10 seconds with 200 μm sample translation between each shot. However, continuous translation (approximately 1 mm per minute) of the stage produced isotope ratios most closely matching declared values and was the primary method used.

Demonstration of clear signal

Figure 2.5 demonstrates rapid signal rise and washout, implying no latent material flow through the tubing. This step of the characterization process was important to show that signals from previous samples would not interfere with the signal of the following analysis. Transport of the sample material, most likely in aerosol form, is quantitative. The low background signals (essentially zero) for analytes of interest such as tungsten and zirconium support the conclusion that there is no buildup of analyte in the tubing. Periodic replacement of the tubing would further preclude any signal mixing.

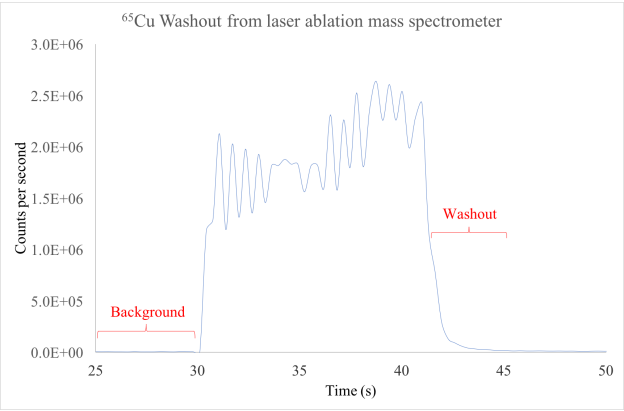

Figure 2.5: Rapid rise and washout of ^{63}Cu signal during laser ablation on a copper foil.

Transport time

In this experimental configuration, ultrapure (99.9999%) helium flows from a storage cylinder through a mass flow controller integrated with the mass spectrometer and on to the ablation chamber. From the chamber it passes directly to the mass spectrometer. The flow rate for all experiments was 624 mL $\cdot$ s^{-1}. The internal radius of the Tygon tubing is 0.2 cm with a length of approximately 1 meter from the laser ablation cell to the mass spectrometer,

with flow rate as indicated by the mass flow controller.

$$624\ \frac{\text{cm}^3}{\text{min}} = 10.4\frac{\text{cm}^3}{\text{s}}$$

Cross section of internal tubing:

$$A = \pi \cdot r^2 = \pi \cdot (0.2)^2 = 0.126\ \text{cm}^2$$

Now divide the flow rate by the cross-section of the tubing:

$$\frac{10.4\ \frac{\text{cm}^3}{\text{s}}}{0.126\ \text{cm}^2} = 82.5\ \frac{\text{cm}}{\text{s}} = 0.825\ \frac{\text{m}}{\text{s}}$$

$$\frac{1\ \text{m}}{0.825\ \frac{\text{m}}{\text{s}}} = 1.2\ \text{s}$$

This shows a 1.2 s travel time from the ablation cell to the mass spectrometer and is supported by the rapid rise times seen in the mass spectra. The limiting factor is the sampling rate of the mass spectrometer itself.

Standing waves in helium tubing

There is the possibility of standing waves in the helium transport tubing, which could negatively influence data collection in the mass spectrometer. The calculation below shows that any pressure oscillations in the tubing have time to equalize during detector integration.

To determine the sound velocity of He under laboratory conditions:

$$v = \sqrt{\frac{\gamma \text{RT}}{\text{M}}} = \sqrt{\frac{(1.67)(8.314)(293)}{.00403}} = 1,008\ \frac{\text{m}}{\text{s}} \tag{2.16}$$

For:

$\gamma = \frac{\text{C}_\text{p}}{\text{C}_\text{v}}$, the heat capacity ratio
R = Gas Constant, 8.3145 $[\frac{\text{J}}{\text{mol}\cdot\text{K}}]$

T = Absolute temperature [K]
M = Molar mass density [$\frac{\text{kg}}{\text{mol}}$]

The frequency within a tube of length L and diameter d is given by:

$$\text{f} = \frac{\text{vn}}{2(\text{L} + 0.8\text{d})} = \frac{1,008 \cdot 1}{2(1 + 0.8 \cdot 0.003)} = 504 \text{ Hz} \tag{2.17}$$

For:

v = Sound velocity in He
n = Mode
L = Length of tubing
d = Diameter of tubing

This gives an upper bound for the frequency. Compare this to a slightly different formula for the frequency within a doubly open-ended tube, where the mode-1 wavelength is π times the tube length. For wavenumber $\text{k}_\text{n} = \frac{2\pi}{\lambda}$, $k_n \cdot$ L = n $\cdot\pi$ and $\lambda = \pi \cdot$ L = $\pi \cdot$ 1 m = 3.14 meters. This gives a frequency for helium at room temperature of 321 Hz. In the expression for frequency, 2(L + 0.8d) is wavelength $\lambda \simeq 2$ meters, roughly twice the length of the tubing. Thus transit time $\frac{1}{\text{frequency}}$ is 2 to 3 ms. This is less than the shortest integration time of 10 ms for the mass spectrometer detector. By this analysis, pressure oscillations in the tubing can be neglected.

2.11 Mass Spectrometry

Table 2.4 shows some advantages and disadvantages of direct injection for mass spectrometry.

Direct Injection	
Advantages	**Disadvantages**
Potential for higher efficiency	Potential increase of matrix effects because there is no pre-treatment
Less oxide formation	Loss of sample due to settling during transport
Little or no sample pretreatment	Chemical or electrostatic adsorption inside transport tubing
Effective on hard-to-dissolve solids such as ceramics	
Potentially high (μm) spatial and depth resolution	

Table 2.4: Advantages and disadvantages of Direct Injection ICP-MS.

Similarly, ICP-MS has been preferred over ICP-Optical Emission Spectroscopy (ICP-OES) because mass spectrometers with high resolution can distinguish between interferents and analytes while ICP-OES generally cannot. However, ICP-OES remains an important tool

because of its longer period of development and thus larger assemblage of refereed work, plus lower cost (Montaser et al., 1998).

ICP Torch

The most common ICP torch configuration is the Fassel design. Advantages include a smaller internal diameter and lower argon flow rate, hence lower Radio Frequency (RF) power requirement, compared to the Greenfield design. The drawback is that because of the smaller diameter, it is more sensitive to high matrix loading and can clog more easily than the larger Greenfield design (Turner & Montaser, 1998).

The resonant frequency of the coil is given by:

$$f = \frac{1}{2\pi}\sqrt{\frac{1}{\mathrm{LC}}} \tag{2.18}$$

For:

f = Frequency
L = Inductance
C = Capacitance

Advantages of the ICP (Montaser et al., 1998) include high temperature, high electron number density, long residence time inside the plasma ($\sim$ 2 ms), low levels of molecular species, and a robust plasma.

Sample and Skimmer Cones

Sample and skimmer cones provide a way to step down from atmospheric pressure to high vacuum. When the plasma is lit, the high temperature corresponds to a decreased number density of ions. The pressure before the sampler cone drops once the plasma is lit. Using $\mathrm{PV} = \mathrm{Nk}_B\mathrm{T}$ for one cm^3 around the sampler cone:

$$\mathrm{N_{Ambient}} = \frac{\mathrm{PV}}{\mathrm{k_B T}} = \frac{101,325\mathrm{Pa}\cdot 10^{-6}\,\mathrm{m}^3}{1.38\mathrm{x}10^{-23}\cdot 300\mathrm{K}} = 2.45\,\mathrm{x}\,10^{19}\,\mathrm{atoms} \tag{2.19}$$

$$\mathrm{N_{Plasma}} = \frac{\mathrm{PV}}{\mathrm{k_B T}} = \frac{101,325\,\mathrm{Pa}\cdot 10^{-6}\,\mathrm{m}^3}{1.38\mathrm{x}10^{-23}\cdot 8,000\mathrm{K}} = 9.18\,\mathrm{x}\,10^{17}\,\mathrm{atoms} \tag{2.20}$$

The increase in temperature brings about a two decade drop in number density at the sampler cone inlet. The slide valve allows access to the inner high vacuum region only when the plasma is lit because the lower number density reduces the stress on the vacuum system.

Ionization occurs as the sample is carried into the plasma torch. The 8,000° argon plasma is sufficiently energetic to ionize virtually all elements. One drawback of this is that more volatile elements can become doubly charged. Because the torch operates at atmospheric pressure, this is also where polyatomic ions such as oxides and argides are formed. The mean free path in the sampling region is given by (Turner & Montaser, 1998):

$$L = \frac{\mathrm{k_B T}}{\sqrt{2} P \sigma} = 2\ \mathrm{m} \tag{2.21}$$

For:

k_B = 1.38 x $10^{-23} \frac{\mathrm{J}}{\mathrm{K}}$
T = 8,000 K
P = 1.0 Pa
σ = (188 pm)^2 (van der Waals radius of argon)

The mean free path is approximately 2 meters, a reasonable result at 8,000°C and roughing pressure in the sampler region.

Quadrupole Operation

The quadrupole balances time-varying electric fields on the quadrupole mass filter to allow only ions of a specific mass-to-charge ratio to pass through to the detector. The governing equations for the quadrupole are based on the Mathieu equation, itself a subset of the Hill equation.

(Turner et al., 1998) give the Mathieu Equation as:

$$\frac{\mathrm{d}^2 \mathrm{u}}{\mathrm{d}\xi^2} - [\mathrm{a} + 2\mathrm{q}\cos(2\xi)]\mathrm{u} = 0 \tag{2.22}$$

For:

u = x or y, corresponding to the different axes of the quadrupoles

$\xi = \frac{\Omega t}{2}$

Ω = Frequency of applied voltage [Hz]

t = Period [s]

$a_x = \frac{8eU}{mr^2\Omega}$ [Hz]

e = Electric charge [C]

U = Direct Current Voltage [V]

m = Mass of analyte ion [kg]

r = Radius of quadrupole rod [m]

$q = \frac{4eV}{mr^2\Omega}$ [Hz]

V = Alternating Current Voltage [V]

The region of stability for transmission through the quadrupoles happens to correlate to the stability regions for certain vibrating drum surfaces and for balancing a pendulum upright by rapid vertical oscillation. The equations for quadrupole stability are treated in detail by (Hoffmann & Stroobant, 2007), among others.

Detection

The detector measures the voltage generated by each ion that strikes the detector, emitting a few electrons that are accelerated and strike a neighboring dynode, which releases a larger pulse of electrons that in turn is accelerated to an adjacent dynode, thus amplifying the signal to detectable levels. When the signal exceeds about 2 million counts per second, the detector automatically limits the amplification to the first two dynodes, thus preventing detector burnout and maintaining the signal within operating limits.

Dead time correction (Lewis, 2018):

$$C_{true} = \frac{C_{measured}}{1 - \tau \cdot C_{measured}} \tag{2.23}$$

For:

C_{true} = True count rate
$C_{measured}$ = Measured count rate
τ = Detector dead time

(Vanhaecke & Degryse, 2012) give a lucid account of detector dead time. The precision of these initial studies was sufficiently high to not require careful dead time correction. The detector was shown to switch effectively between pulsed and analog mode, so no further work was done in this area.

Mass Spectrometry Bias

Several factors contribute to signal variations in mass spectra. These effects are described here but did not play a significant role in this initial investigation of the system's capabilities.

- Ablation fractionation occurs because work functions differ by element and matrix. The energy required to ionize a given element varies across the periodic table. While femtosecond lasers decrease the effect, they do not completely eliminate it. For example, differences between SiC and metals such as Zr are evident in Figures 4.14 on page 79 and 4.15 on page 80. Figure 4.14 shows deep ablation in the SiC and pyrolytic carbon in contrast to Figure 4.15 which shows virtually no ablation in the zirconium/hafnium core of the TRISO surrogate.

- Transport fractionation (not observed with this system) results as heavier particles fall out from the helium gas stream while lighter particles remain suspended in the gas flow. Femtosecond lasers generally produce smaller particles, down to nanometers. The isotope values were within 1% for expected values, sufficient for these initial investigations.

- Ionization fractionation in plasma results from the variability in the first ionization energy of analytes. For example, the first ionization energy of argon is 15.76 eV, compared to 3.89 eV for Cs. One advantage of argon as ICP gas is that it gives a high ionization fraction for most elements. Doubly charged ions may arise from this strong ionization capability but were not significant in this study, demonstrated by appropriate isotope fractions and $< 5\%$ $\frac{CeO}{Ce}$.

- Mass fractionation in mass spectrometry is the effect of lower-mass ions being preferentially cast out from the beamline due to Coulomb repulsion between positive ions, especially through the skimmer cone and early in the quadrupole. Additionally, for quadrupoles, heavier ions tend to be transmitted with higher efficiency, partly because it takes more energy to throw a heavier ion out of the beamline than a lighter ion.

Early testing with this system showed there was no significant fractionation, even at very high values ($>10^{10}$ counts per second).

- Detection fractionation is a condition in which certain ions are detected more efficiently than others.

  Fractionation Factor: $\frac{\text{Measured - Accepted}}{\text{Accepted}}$

  Based on acceptably accurate isotope ratio results, this type of fractionation was not a significant factor in this work.

- Polyatomic interference arises as the result of chemical recombination, such as argon recombining with oxygen, because the ICP torch operates at atmospheric pressure. Again, isobaric-interference-free istope ratios gave expected results and polyatomic interference was not an issue. In some early runs, the $\frac{\text{CeO}}{\text{Ce}}$ ratio was less than 5%, adequate for this initial study. If they become a problem, oxides can be reduced through tuning, especially of the nebulizer, sampling depth, plasma screen, and collision cell.

- Isobaric interference results from different elements having isotopes of the same mass, such as ^{40}Ar and ^{40}Ca. By identifying isotopes that are unique to a given element, isobaric interference can be ruled out, leaving only polyatomic considerations.

Numerous signal variations are possible. Beginning with ablation, the ability of lasers to faithfully ablate all material in equal fractions has improved steadily over the decades. Femtosecond lasers in particular offer clear advantages over lasers with longer pulse durations. This is because femtosecond lasers deposit their energy pulses faster than the phonon relaxation time of materials. This means that the material surrounding an ablation crater does not have time to heat up significantly before the material is ejected. Further, differential ablation between materials of different ionization energy is seen, such as between metals (e.g. titanium) and dielectrics (e.g., SiC). Somewhat counter-intuitively, metals are more difficult to ablate than dielectrics. At any rate, the difference in number of atoms produced per unit energy varies by element.

The concentration of silver as a function of depth through a silicon carbide matrix could be challenging. The issue of differential ablation of various materials can be overcome using calibrations, but the calibrations will be specific to the analyte and matrix.

Different ionization energies will influence the fraction of each element ionized in the argon plasma. Elements with higher ionization energy are expected to have a smaller fraction ionized. Again, this is accounted for to some extent by the calibrations, but different matrices and different analyte concentrations will influence the ionization fraction.

Once ionized, mass fractionation is possible, especially for high ion concentrations in the ion optics and quadrupole. Here, mass bias is introduced by Coulomb repulsion of like positive

charges in the ion stream. At high concentrations, lighter ions will be preferentially ejected from the beam, since with less mass they are more easily accelerated than heavier ions.

The final consideration is detector efficiency. This too is accounted for by the calibration curve, but at high ion count rates, detector dead time becomes a factor.

Treatment of Isobaric Interference

One method of working around isobaric interference is outlined below.

Isobaric interference between ^{114}Cd and ^{114}Sn presents the following situation:

$$\mathrm{I}(\frac{\mathrm{m}}{\mathrm{z}}) = \mathrm{I}(^{114}\mathrm{Cd} + ^{114}\,\mathrm{Sn}) \tag{2.24}$$

Rearrange:

$$\mathrm{I}(^{114}\mathrm{Cd}) = \mathrm{I}(\frac{\mathrm{m}}{\mathrm{z}}) - \mathrm{I}(^{114}\mathrm{Sn}) \tag{2.25}$$

To find I(^{114}Sn), measure the intensity of an isotope with no interference, here ^{118}Sn.

Then:

$$\mathrm{I}(^{114}\mathrm{Sn}) = \frac{\mathrm{Abundance}(^{114}\mathrm{Sn}) \cdot \mathrm{I}(^{118}\mathrm{Sn})}{\mathrm{Abundance}(^{118}\mathrm{Sn})} \tag{2.26}$$

In practice, software programs such as Glitter do most of the corrections. Modern high-performance mass spectrometers are able to resolve most interference, making the calculations unnecessary. The objectives of this work did not require high precision.

Vacuum Systems

A key development in the viability of mass spectrometry came with the sampler and skimmer cone concept by (Houk et al., 1980). This allowed the transfer of ions from production at atmospheric pressure in the argon plasma to the high vacuum of the ion flight path. To maintain vacuum against the small leak in the vacuum chamber, both roughing pumps and turbomolecular pumps are used. Roughing pumps operate by mass transfer. Turbomolecular pumps consist of counter-rotating blades that transfer gas out of the chamber by momentum transfer. Because there are no one-way valves, they are limited by the backpressure and require the use of a roughing pump to bring them down to sufficient vacuum that the mean

free path of gas molecules is large enough to span the distance between consecutive rotors within the pump.

(Alvarede & Beard, 2004) compared TIMS with MC-ICP-MS. Though the present work uses a single collector, the comparison is illustrative. In essence, thermal ionization and inductively coupled plasma represent opposite ends of a spectrum. Thermal ionization is slow and gentle, imparting very little excess energy to the ions. The temperature ramp may take hours, allowing chemical and structural changes to occur in the sample. More volatile elements vaporize first, and within an element, lighter isotopes are volatilized first. This imparts a strong fractionation over time. In contrast, argon plasma ionizes virtually all of the analytes simultaneously, though to varying degrees based on ionization energy. However, the high thermal energy of the plasma also imparts a wide range of kinetic energy to the ions. This range of kinetic energy must be filtered, either through double focusing involving an electrostatic filter or by the use of a collision cell. The advantages of argon plasma are vastly greater throughput and decreased mass fractionation over time, at the cost of polyatomic, isobaric, and doubly charged ions, which complicate spectral analysis.

This method provides isotope ratios within 1% of declared values for CRM-125A and holds promise for remote characterization of spent fuel.

Table 2.5: A comparison of ICP-MS versus TIMS (after Vervoort & Mueller (2020)).

ICPMS Advantages	**ICPMS Disadvantages**
Greater ionization efficiency than TIMS	Polyatomics and doubly charged ions
Wide variety of sample introduction methods	Plasma instabilities limit precision
Mass fractionation is time invariant	Sampler and skimmer cones are inefficient
TIMS Advantages	**TIMS Disadvantages**
High ionization efficiency	Lengthy preparation and run times
Low kinetic energy	Mass fractionation changes continuously

2.12 Nuclear Materials

One priority with nuclear fuel is to know the isotope content of the uranium fuel. Mass spectrometers are well suited to measure the $\frac{^{235}\mathrm{U}}{^{238}\mathrm{U}}$ ratio. After going through a power reactor, this ratio is altered. Knowing specifically how the ratio has changed is important for reactor operators to optimize the remaining fuel load. However, spent fuel is extremely radioactive and often remains for a few years in a pool before it is analyzed. LAMS offers a potential method to remotely interrogate spent fuel soon after it leaves the reactor, providing more up-to-date information for operators. Of increasing interest is the ability to achieve

higher burnups, into 60 GWd/tHM (GigaWatt-days per ton Heavy Metal) to further increase profitability and decrease the spent fuel load. Nuclear reactors are severe environments in terms of temperature, radiation, and corrosion. Material toughness is a primary factor in determining the reactor lifetime, which directly equates to profitability. (Rondinella & Wiss, 2010) examined the high burnup structure and rim structure.

Materials important to the nuclear industry include cerium, lanthanum, neodymium, stainless steel, and tungsten. Cerium was found in all five LANL samples examined in this work. Neodymium is an indicator of burnup important to forensic analysis. Tungsten is an important additive in certain Ceramic-Metal (CERMET) nuclear fuels and surrogates. For example, (Hickman et al., 2014) and (Schnitzler & Borowski, 2012) investigated tungsten as a matrix for depleted uranium dioxide in space propulsion applications. These are akin to the MAX phases initially discovered by Nowotny (Nowotny, 1970) in the 1960s. Here, MAX stands for:

M = Early transition metal, e.g. Ti
A = Group 12 or 13 element, e.g. Si
X = C or N

Both CERMET and MAX phase materials continue to play important roles in the nuclear industry in applications ranging from reactor cores to turbine blades. Investigating tungsten in depleted uranium oxide surrogates can inform present-day nuclear and aerospace applications (Hickman et al., 2014). To this end, five surrogate fuel pellets composed of depleted uranium (as UO_2) with tungsten impurities were analyzed. The primary objective was to investigate the pellets using laser ablation mass spectrometry to confirm the results of a previous neutron tomography experiment at Los Alamos National Laboratory.

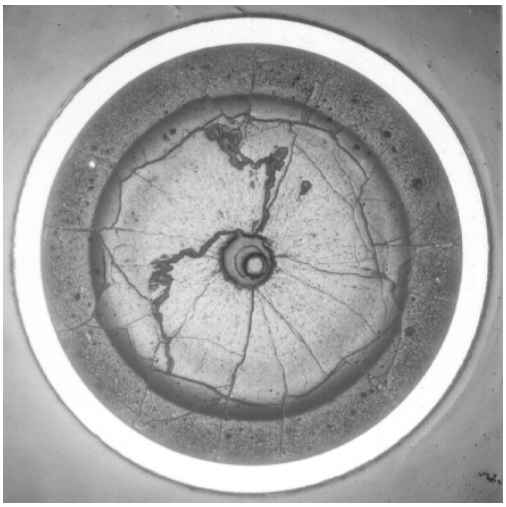

Figure 2.6: PWR fuel showing burnup structure, from the Halden Boiling Heavy Water Reactor in Norway (Nakamura, 1998).

One example of the changes that occur in light water reactor fuel is shown in Figure 2.6; here, the reactor fuel was irradiated to 63 MWd/kgU. The cladding (white), porous outer ring, heavily fractured intermediate ring, and off-axis central void demonstrate the dynamic environment of high burnup nuclear fuel. (Rondinella & Wiss, 2010) studied the formation of rim structure in high burnup fuel. In addition to studying the rim structure with LAMS, the use of Integral Fuel Burnable Absorbers (IFBA) in some Westinghouse fuels would be another application (Lee, 2002). The ZrB_2 coating could be readily analyzed along with the rim structure for both elemental and isotopic composition.

2.13 Tri-Structural Isotropic Fuel (TRISO)

Chapter 1 described the importance of TRISO to the nuclear industry. This section presents results of laser ablation on surrogate TRISO particles. To begin, Figure 2.7a shows the internal structure of a typical TRISO particle. Porous pyrolytic carbon is designed to contain fission products, while the outer SiC layer provides a mechanical and chemical boundary, both to keep fission products within the particle and to keep contaminants out of the particle. Figure 2.7b illustrates a simplified decay scheme for ^{110}Ag. This isotope appears to escape from High Temperature Gas Reactors (HTGR) with unexpected ease (IAEA, 2010), (Sawa & Tanaka, 1995). Cadmium is used as an absorber in some nuclear reactor ducting and could act as a source for ^{110}Ag through neutron capture. However, ^{110}Ag is found even where cadmium is not present. Figure 2.8a demonstrates an intact surrogate particle prior to ablation. Figure 2.8b provides a closeup of the surface granularity.

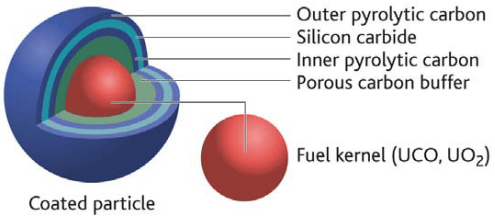

(a) A typical TRISO particle in cross section showing pyrolytic carbon to trap fission gases and silicon carbide to provide mechanical strength (Hales et al., 2013). Reproduced with permission.

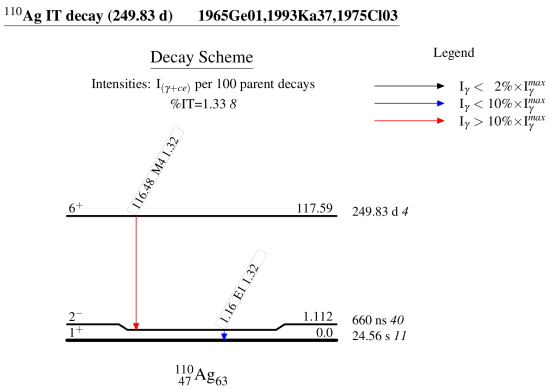

(b) ENSDF decay scheme for ^{110m}Ag (Gurdal & Kondev, 2012) showing the 249.83 day half-life that poses a threat to reactor maintenance workers.

Figure 2.7: Overview of the main research point with TRISO as a nuclear fuel. ^{110m}Ag escapes the fuel kernel, passes through the pyrolytic carbon and SiC layers, and plates out in the reactor where its gamma emission threatens worker safety. The last two figures show an intact surrogate with a closeup of a surrogate TRISO particle.

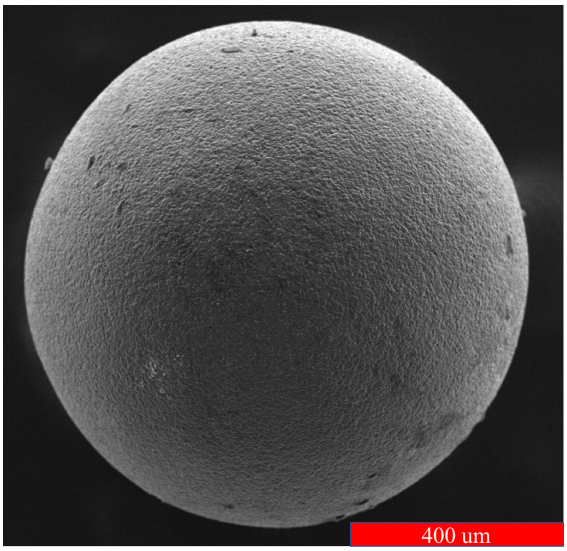

(a) Surrogate TRISO particle prior to laser ablation showing the granular surface.

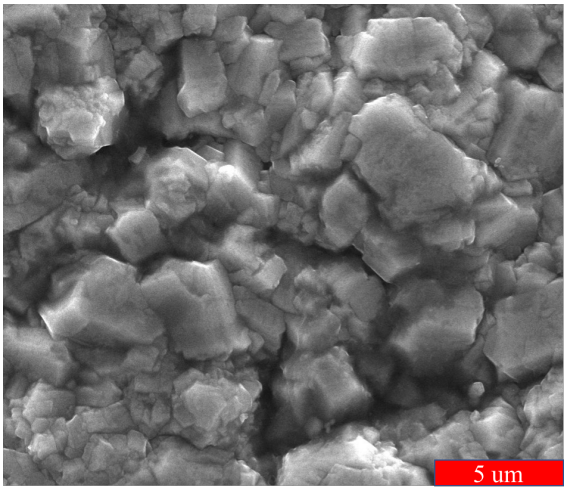

(b) Closeup of the granular surface of a surrogate TRISO particle.

Figure 2.8: Overview of the main research point with TRISO as a nuclear fuel. ^{110m}Ag escapes the fuel kernel, passes through the pyrolytic carbon and SiC layers, and plates out in the reactor where its gamma emission threatens worker safety. The last two figures show an intact surrogate with a closeup of a surrogate TRISO particle.

Production of ^{110m}Ag

(Friedland et al., 2011) found a stable fission yield of 0.03% for ^{109}Ag from ^{235}U, with a 0.1% conversion rate to ^{110m}Ag by neutron capture. Decay chains from ^{107}Y, ^{108}Y, ^{110}Zr, and ^{112}Cs also feed ^{110}Ag:

^{238}U (n, γ) ^{239}U $\rightarrow$ ^{239}Np + β^- + $\overline{\nu}$ $\rightarrow$ ^{239}Pu + β^- + $\overline{\nu}$

^{239}Pu (n, fission) ^{109m}Ag, fission yield = 0.0167

^{109m}Ag (γ decay) ^{109}Ag, 88.0 keV, $t_{\frac{1}{2}}$ = 39.8s

^{109}Ag (n, γ) ^{110m}Ag, 657.8 keV, $t_{\frac{1}{2}}$ = 24.6s (Gurdal & Kondev, 2012)

^{110m}Ag $\rightarrow$ ^{110}Cd + β^- + $\overline{\nu}$, branching ratio = 0.9864

^{110m}Ag $\rightarrow$ ^{110}Ag + 117.6 keV γ, branching ratio = 0.0136, $t_{\frac{1}{2}}$ = 249.7 days (This is the key reaction because of the comparatively long half-life.)

Diffusion coefficients for Ag in reactors

Many attempts have been made to determine the diffusion coefficient for silver and its mechanism of escape from SiC, e.g. (Carter et al., 2018). At present, the argument can be narrowed to two different pathways.

1. ^{110m}Ag has been observed outside of intact TRISO particles, refuting (MacLean, 2004), unless the damage is below detection limits. Given that the state-of-the-art for microscopy has been sub-nanometer for over a decade, this explanation seems unlikely.

2. Kim (B. G. Kim et al., 2015) asserts that neutron damage at high temperature could account for the ability of silver to exit the fuel. However, this does not explain why other fission products remain contained, unless a different material such as PyC can be shown to remain a trapping agent even at high temperature and high neutron flux. If neutron flux is a key factor, then release rates should scale with neutron flux, as found by (Meher et al., 2019).

For IG-110, $D_o = 6.6 \times 10^{-4}$ $\frac{m^2}{s}$ and $E_a = 174$ $\frac{kJ}{mol}$. This is a very high diffusion coefficient compared to other TRISO configurations. However, (B. G. Kim et al., 2015) noted that Ag is still found to escape even from intact particles with much lower diffusion coefficients.

Preliminary work was done on surrogate TRISO particles taped to a sacrificial surface and ablated. Visual reference of the plasma through the video camera provided the only means to position the laser shots. A quantitative positioning system would be necessary for precise work in future studies. Of particular interest is the transport of ^{110m}Ag out of the TRISO particles, after which it plates out inside the cooling ducts of the High Temperature Gas Reactors. This plated material presents a health hazard to workers performing maintenance on the reactor and complicates decommissioning.

In High Temperature Gas Reactors the neutrons are unmoderated, thus the mean free path is longer and fission occurs throughout the TRISO spheres or graphite prism. The SiC of the TRISO spheres is generally effective at retaining fission products, but silver (especially ^{110m}Ag) and a few other elements are able to escape the SiC confinement layers and plate out within the reactor. One goal of this work is to develop a diagnostic capability to ablate into TRISO particles in fine increments to determine where the highest concentration of silver is found. (Gerczak et al., 2015) suggested that the SiC layer microstructure influences the release of silver by particles with large columnar-grained SiC layers. These large columnar-grained SiC layers have been observed to release a larger fraction of Ag fission product inventory relative to particles with fine-grained SiC layers. Gerczak conducted SIMS analysis using a Cameca IMS 7f-GEO. Depth profiles were obtained for Ag in SiC by rastering over a 200 x 200 μm area. They found that Ag release from TRISO fuel was much higher than from diffusion experiments but did not posit a reason. More recently, (van Rooyen et al., 2018) found that Ag release from SiC depended on the pore size, ranging

from approximately two nm pore diameter (high fraction of Ag retained) to seven nm, with almost complete release of the Ag burden. These results tie in with Kim (B. G. Kim et al., 2015) and (MacLean, 2004), where a combination of neutron flux, high temperature, and nanocracking (equivalent to nanopores) may explain the observed Ag release.

Diffusion of Silver through SiC

Ag is found in pipes and turbines, implying that it leaves the fuel particle as a vapor or that Ag is extant and activated in the piping. This is unlikely but possible because some materials were intentionally doped with Cd and Ag as neutron absorbers. Nevertheless, research shows that Ag can escape from intact TRISO. Regardless of whether neutron activation of extant Ag occurs in the piping, the diffusion of Ag through the SiC layer in TRISO is the primary issue and has vexed workers for over four decades. Despite all manner of experiments (van Rooyen et al., 2014) plus many years of computational effort (Seibert et al., 2018), the mechanism of Ag transport through SiC remains unclear. (Morris et al., 2004) report that high thermal gradients ($>1{,}000\frac{\mathrm{K}}{\mathrm{mm}}$) can drive thermal diffusion (known as thermophoresis or the Soret effect) of fission products across the layer. However, such high gradients are unlikely during normal operations. Research over the years allows a focus on Ag alone moving through intact SiC. Indeed, (van der Merwe, 2009) found that intact TRISO was the primary source of Ag. Enhancing effects such as cracks in the SiC or Pd as a corrosive, while important and relevant, are not central issues. The most difficult scenario to understand is the escape of Ag by itself from intact TRISO. (Neethling et al., 2012) found that annealing strongly enhanced Ag transport. Impurities at lattice faults may increase the high void concentration along the (111) planes of SiC. (López-Honorato et al., 2011) showed that the deposition process to make TRISO particles can strongly influence Ag transport through it. (López-Honorato, Yang, et al., 2010) also noted the presence of liquid and the possibility of a eutectic between Ag and Pd-Si. These points are interesting but do not address the most fundamental question of how pure Ag moves through intact SiC.

Reactor piping was sometimes made with Ag-Cd-In for mechanical and thermal stability, high neutron absorption cross section, and corrosion resistance. If such piping was used in the construction of the high temperature reactors, neutron activation of the silver would explain the high activities observed in multiple experiments such as the Advanced Gas Reactor (AGR) test at Idaho National Laboratory. Nevertheless, the issue of Ag escape from intact TRISO particles must be addressed, even if only as a palliative measure, in order to attain the greater efficiency, reduced fuel load, reduced cost per kiloWatt, and reduced high level waste burden that High Temperature reactors promise.

Diffusion

As recently as 2020, efforts were under way to identify fission product migration through fuel and cladding using high resolution EDX and High-Angle Annular Dark Field (HAADF) spectroscopy (Clark et al., 2020).

Fick's First Law

Fick's Law for diffusion is analogous to Darcy's Law for hydraulic flow, Ohm's Law for charge transport, and Fourier's Law of heat transport. Begin with the diffusion coefficient D, derived by Einstein (Einstein, 1905):

$$D = \mu \mathrm{k_B T} \tag{2.27}$$

for:

D = Diffusion coefficient
$\mu = (6\pi\eta \mathrm{r})^{-1}$ = Particle mobility
η = Dynamic viscosity
r = Particle radius
$\mathrm{k_b}$ = Boltzmann constant
T = Temperature

This equation relates the diffusion constant D to particle mobility, μ, which is the ratio of the particle's terminal drift velocity to an applied force, e.g. an electric field. Thermal diffusion results from the thermal motion of particles across a temperature or concentration gradient after overcoming the activation energy of the lattice.

$$D = \mathrm{D_o e^{-\frac{Q}{RT}}} \tag{2.28}$$

Taking the log of both sides:

$$\ln(\mathrm{D}) = \ln(\mathrm{D_o}) - \frac{\mathrm{Q}}{\mathrm{R}} \cdot \frac{1}{\mathrm{T}} \tag{2.29}$$

which takes the form of a line: $\mathrm{y = m \cdot x + b}$

For:

D = Diffusion Coefficient
D_o = Diffusion coefficient at STP

Q = Activation energy for diffusion ($\frac{\mathrm{J}}{\mathrm{mol}}$)
R = 8.31 $\frac{\mathrm{J}}{\mathrm{mol \cdot K}}$

Plot log D versus $\frac{1}{\mathrm{T}}$ to obtain a straight line of slope $\frac{-\mathrm{Q}}{\mathrm{R}}$. Note that this doesn't work because the variable is in the denominator of the exponent, rendering the expression nonlinear unless the equation follows a power law to exponent (-1), in which case taking the inverse converts the equation to a linear form.

Vacancies and interstitials play a key role in material behavior. The number of vacancies can be calculated by:

$$N_{\mathrm{v}} = Ne^{\frac{-\mathrm{Q}}{\mathrm{k_b T}}} \tag{2.30}$$

The diffusion of vacancies and interstitials can be calculated to first order using:

$$J = -D\frac{\mathrm{dC}}{\mathrm{dx}} \tag{2.31}$$

For:

D = $D_o \mathrm{e}^{\frac{-\mathrm{Q_d}}{\mathrm{RT}}}$
$\mathrm{Q_d}$ = Activation energy for diffusion = [$\frac{\mathrm{J}}{\mathrm{mol}}$].
Taking the logarithm gives ln(D) = ln($\mathrm{D_o}$) - $\frac{\mathrm{Q_d}}{\mathrm{R}}\frac{1}{\mathrm{T}}$, which is linear if T is to power -1. Plot ln(D) vs $\frac{1}{\mathrm{T}}$ to determine $\mathrm{Q_d}$ and $\mathrm{D_o}$. The graph has slope $\frac{-\mathrm{Q_d}}{\mathrm{R}}$ with intercept ln($\mathrm{D_o}$).

Combined effect of concentration gradient and thermal gradient

(Morris et al., 2004) show that:

$$J = -D(\nabla C + \frac{\mathrm{CQ}}{\mathrm{RT^2}} \cdot \nabla T) \tag{2.32}$$

For:

J = Diffusive flux [$\frac{\mathrm{g}}{\mathrm{cm^2 \cdot s}}$]
D = Diffusion coefficient [$\frac{\mathrm{m^2}}{\mathrm{s}}$]
C = Concentration [$\frac{\mathrm{g}}{\mathrm{cm^3}}$]
Q = Heat of transport [$\frac{\mathrm{J}}{\mathrm{m^2}}$]
R = Gas constant [8.314 $\frac{\mathrm{J}}{\mathrm{mol \cdot K}}$]
T = Temperature [K]

where the first term represents flux due to concentration gradient and the second is the Soret Effect, in which a high thermal gradient can drive diffusion. Most substances move across the thermal and concentration gradient as with Ag, which is found in pipes and turbines. Ag may leave the fuel particle as a vapor and then condense in the ductwork or it may be extant in the piping and activated in place by the neutron flux.

Note that Fickian diffusion assumes steady state concentration gradients, which does not hold with the nanoscale deposits of Ag considered here. Many mechanisms have been proposed, and many may play a role, but transport due to a chemical concentration gradient is not supported.

Compact deconsolidation and AGR-1 testing

Fuel compacts require substantial effort to render for analysis. Table 2.1 gives the steps to deconsolidate a fast reactor compact, in contrast to the comparatively straightforward method of laser ablation.

Table 2.6 shows that the reactor conditions for AGR-1 Compact 4-1-1 were sufficient to cause significant release of silver.

Table 2.6: AGR-1 reactor conditions.

AGR-1 Parameters	
Quantity	Value
Enrichment	19.26% ^{235}U
Fluence	4.13 x 10^{25} $\frac{n}{m^2}$
Average T	1072 ^{o}C

Results of AGR-1, Compact 4-1-1

Of the several compacts tested in the Advanced Gas Reactor at Idaho National Laboratory, Compact 4-1-1 was among the most interesting from the perspective of Ag release and is the focus of discussion here. Analysis of Advanced Gas Reactor Compact 4-1-1 at Idaho National Laboratory yielded several insights intoTRISO behavior under irradiation. Significant silver release occurred during AGR-1 (Scates et al., 2007), from 0 to 100%, for various compacts. Pd nanoparticles were found at stacking faults. Ag deposits occurred at triple points and grain boundaries. Ag was always found in the presence of Pd in 4-1-1 but occurred by itself in compact 6-3-2. This makes the Pd-assisted Ag transport hypothesis not directly relevant;

while Pd may in fact assist Ag transport, it is not a necessary condition. Though over three decades of work have tried to solve the silver transport problem, it remains an issue for high temperature TRISO-fueled reactors (van Rooyen et al., 2014).

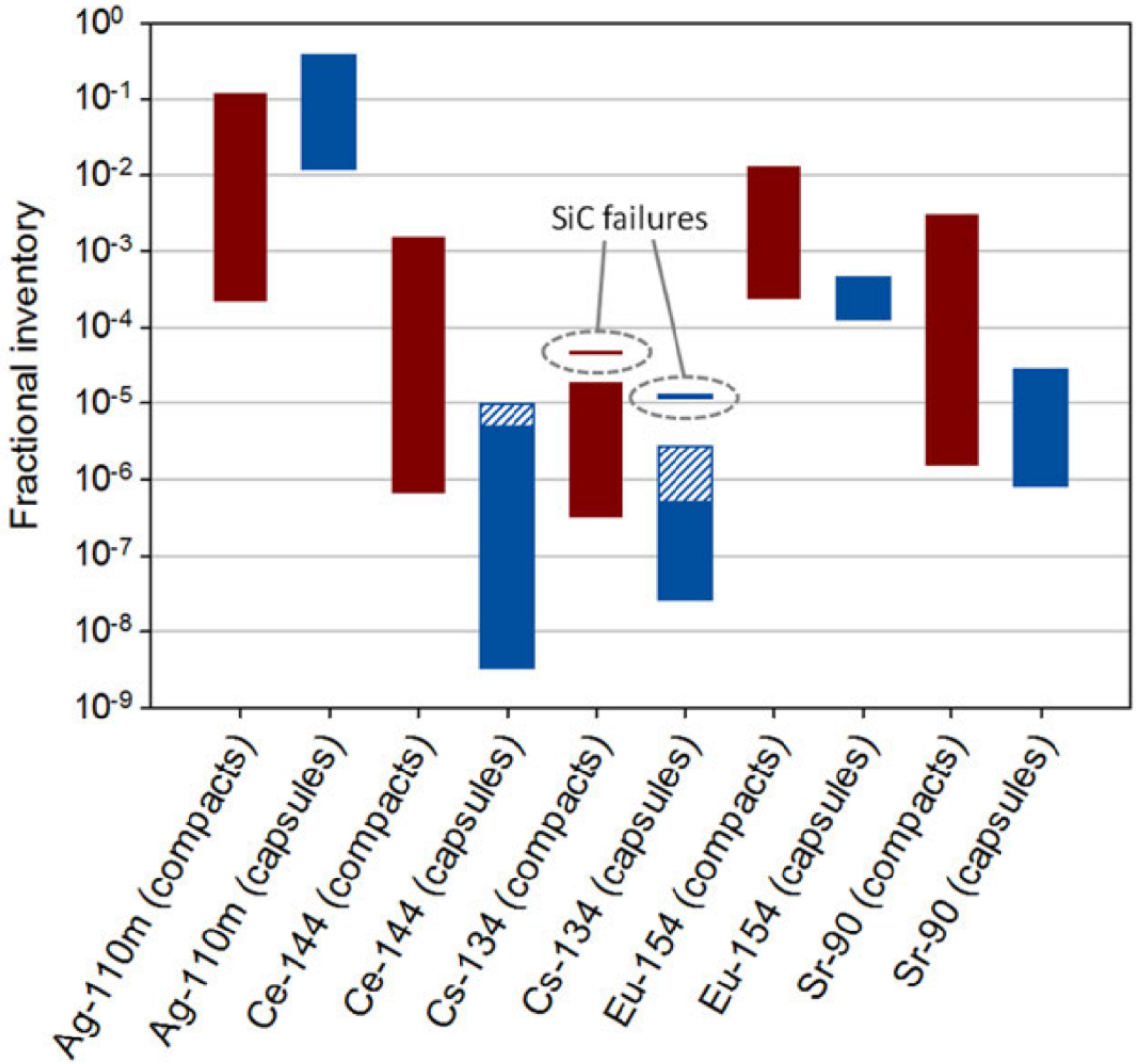

Figure 2.9: Plot showing significant release of silver from test 1 of the Advanced Gas Reactor (AGR-1) TRISO capsules (Vanderheyden et al., 2021). Image used with permission.

The release of silver shown in Figure 2.9 is complemented by the data in Figure **??**, which shows the softening of SiC with temperature and porosity, from (Snead et al., 2007). This

demonstrates how TRISO can become more porous at high temperature but then self-anneal as it cools down, making it difficult to detect the reason why silver can escape. The reason why silver escapes more readily than other noble metals remains unclear and invites further research.

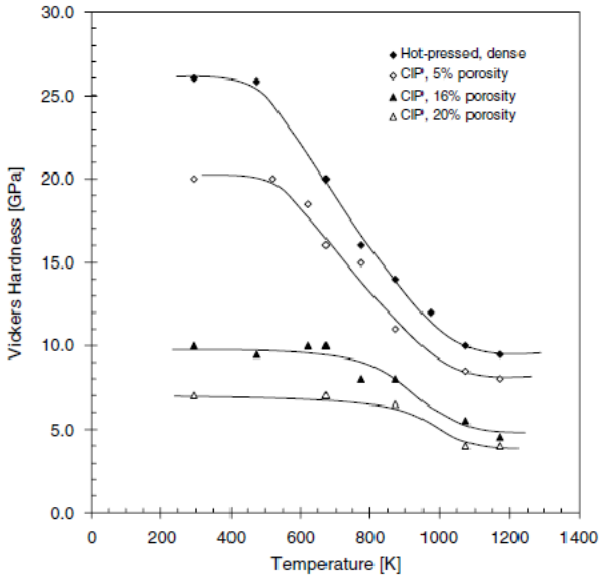

Figure 2.10: SiC hardness as a function of temperature and porosity (Snead et al., 2007), reprinted here under Elsevier license number 5295390502512.

High Temperature Gas Reactors (HTGR) offer many advantages over Pressurized Water Reactors (PWR). Higher operating temperatures allow greater burnup, thus greater fuel efficiency. Higher burnup may also reduce the fraction of long-lived waste. With a sufficiently high operating temperature, energy-intensive industrial processes such as ammonia production, distillation, and desalination become more economical. A persistent issue with the fuel for high temperature reactors has been the loss of certain fission products, especially ^{110m}Ag, for reasons that remain unclear. The favored candidate for HTGR fuels is Tri-Structural Isotropic (TRISO) spheres composed of a uranium core surrounded by layers of pyrolytic carbon to absorb fission products and SiC as a barrier both to contain fission products and to provide mechanical strength against deformation (Hosemann et al., 2013). Despite over 40 years of literature surrounding the transport of silver and other fission products through SiC, the issue persists (Cancino et al., 2018). The next chapter describes a possible method for laser ablation mass spectrometry that may be applied to spent fuel to determine isotopic distribution and concentration of fission products.

Chapter 3

Method

The approach taken for this work consisted of fundamental studies on standards with planned work for enriched fuel and a fiber laser. The NIST 125-A reference for uranium isotopics, NIST 610 series glasses for an array of trace element concentrations, and Los Alamos surrogate nuclear fuel samples provided by Professor Peter Hosemnn, chair of the Nuclear Engineering Department at UC Berkeley, composed the analysis regimen. Though a full system setup and calibration was not conducted, the results of the NIST calibration curves provide a useful baseline.

3.1 NIST Glass

Ideally $\frac{\text{CeO}}{\text{Ce}}<1\%$ for oxides. Because Ce has one of the highest oxygen affinities, it serves as a proxy for the presence of oxygen. The ratio for the NIST Glass data was measured at 5% for one early data set and received no further treatment.

(Gaboardi & Humayun, 2009) showed the difference in transparency between NIST 610 and NIST 616 glass. They also pointed out the preference for geologically relevant samples such as BHVO-2G and BCR-2G because of the improved matrix matching. (Evans & Müller, 2018) investigated NIST glasses and found variations in concentration, but this subtlety lies beyond the present study. NIST glasses provide calibration for a low precision investigation as proof of principle. (Wojciech & Huneke, 1991) state that for high–resolution mass spectrometers, only the slope of the calibration line is needed, which itself constitutes what is known as the Relative Sensitivity Factor (RSF). However, it has become common practice to define the RSF as a multiplicative factor applied to the measured ion current ratio to calculate the declared concentrations. The Thermo-X calibration curves, though showing high R^2 values greater than 0.99, fail to produce meaningful concentration values for most analytes. The use of raw counts and ratios for matrix elements such as silicon in NIST glass and uranium in the LANL samples provides semi-quantitative information. The detailed

steps of the RSF calculation are given in Appendix 7.3.

3.2 Laser ablation instrumentation

Figure 3.1 shows the major components of the Spectra-Physics Tsunami femtosecond laser used in these experiments. The Tsunami laser is pumped longitudinally via a continuous wave diode laser. Titanium ions (Ti^{3+}) are doped into an Al_2O_3 matrix to provide the lasing medium (**?**).

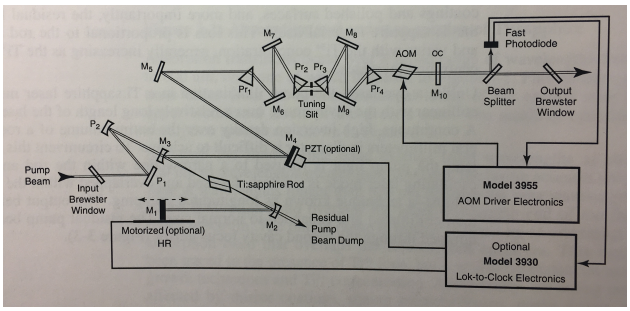

Figure 3.1: Spectra-Physics Tsunami laser layout. The pump laser is a tunable continuous wave diode laser pumped at 810 nm, corresponding to an absorption window in Nd^{3+}. The output is an optical comb allowing broadband pumping of the Tsunami laser (Spectra-Physics, 1998). Image courtesy of MKS Instruments, Inc.

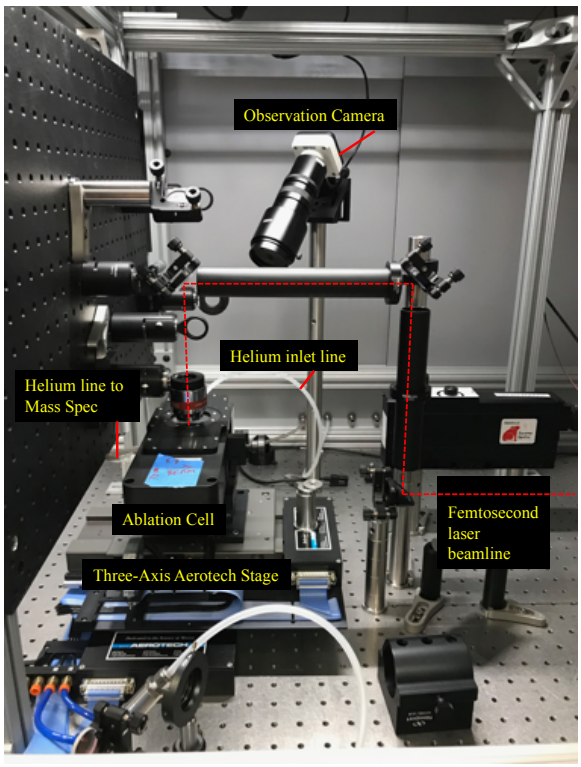

Figure 3.2: Three-axis Aerotech stage with ablation cell and observation camera. The beam approaches from the right side of this figure and enters the ablation cell from above.

Ablation Method

Figures 3.3a and 3.3b show typical ablation tracks in NIST glass. Tracks in other materials appear generally similar, except for TRISO surrogates. The TRISO surrogate particles exhibited much deeper cratering for a given laser power compared to metals. Another key finding was the sensitivity to changes in sample height relative to the laser focus. The use of a Schwarzschild lens to minimize chromatic aberrations resulted in a narrow Rayleigh length (Figure 2.4). This sensitivity to the sample height could be employed to advantage for certain experiments but required care with cylindrical samples. Ideally, even the NIST glasses would be polished with front and back surfaces exactly parallel.

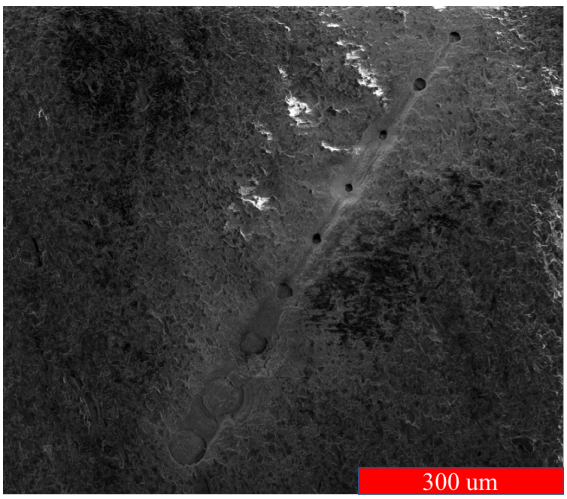

(a) Z-axis sensitivity in NIST 610 showing the increase in crater diameter and annularity as the surface falls out of focus with sample curvature.

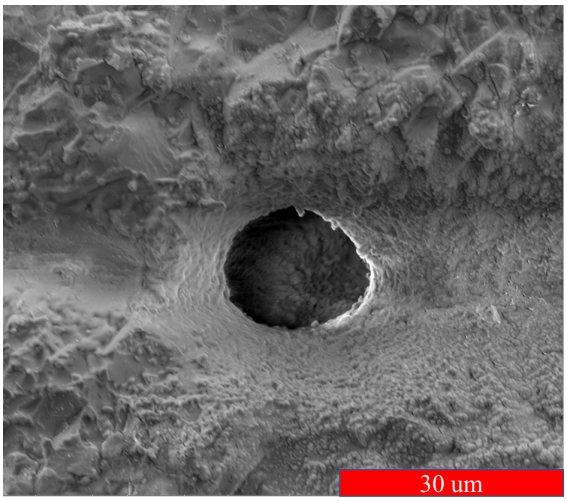

(b) Crater closeup of NIST 612 showing a typical ablation pattern after a 30 second dwell.

Figure 3.3: (a) Typical ablation craters in NIST glass showing the effect of curvature on the ablation. Note the marked decrease in ablation effectiveness with a slight change in vertical position of the surface. (b) Closeup of an ablation crater.

Elements of interest to the nuclear industry

The nuclear industry employs a broad range of elements in reactors and weapons. Examples include TiO_2, Nb_2O_5, CrO_2, CaO, C, W, and V_2O_5, which can be doped into materials to increase grain size, porosity, and mean free path (Radford & Pope, 1983). This is important because increased porosity creates space for fission gases. Further, zinc stearate can be added to improve homogeneity in the sintering process (Ohai, 2002). Quantification of B, Be, Li, C, the rare earths, and fission products is important for nuclear applications. Hydrogen embrittlement plays a role in material failure. Hydrogen analysis can be done using Residual Gas Analyzer Mass Spectrometry. The ability to detect elements from lithium to plutonium is desired. ICP-MS systems generally perform best with high masses such as uranium, but high-resolution systems can be successful wih even lighter masses. ^{56}Fe demonstrates polyatomic interference with $^{40}Ca^{16}O$ and $^{40}Ar^{16}O$ because all three are approximately 56 atomic mass units (amu). By looking at other isotopes of iron that do not share polyatomic or isobaric interferences (where isobaric interference comes from a different element with the same mass, such as ^{40}Ar and ^{40}Ca), the overlap can be avoided. Though high-resolution systems mitigate most of the polyatomic interferences, awareness of the major analytes and their interferents is important. Table 3.1 shows those analytes of interest to the nuclear enterprise free from isobaric interferences with their corresponding polyatomic interferences,

after (May & Wiedmayer, 1998) and (Yang et al., 2018).

Polyatomic and isobaric overlap

Another difficulty with ICP-MS systems is their decreased sensitivity to lighter masses. For elements below copper, this sensitivity can decrease sharply. In some cases, mass bias for elements such as Li and B can be greater than 10%, while the same instrument can show less than 1% for heavy isotopes. Early efforts with this system showed positive results with light elements such as boron. However, later calibrations failed to reproduce this fidelity for light masses below strontium. Cleaning, maintenance, and recalibration could restore the earlier capability for low masses. Table 3.1 shows isobaric interference-free isotopes with applications and polyatomic interferents. Dajie Sun (LBNL) wrote a Python code to automatically graph the mass spectra. Given the variability in data formats, the code was not used exetensively but it offers a strong foundation for future automation. The full code is given in Appendix 7.1.

Isobaric interference-free isotopes to search for in LANL Samples with corresponding polyatomic interferents

Analyte	Application	Interferent
^{6,7}Li	^{3}H production, Corrosion control	$^{12}C^{2+}$
^{9}Be	Neutron source/reflector, Tracer	$^{18}O^{2+}$
^{10,11}B	Moderator, pH, Alloy	Borosilicate glass torch
^{23}Na	Fast reactors	$^{7}Li^{16}O$
^{24,25,26}Mg	Cladding, Structural material	$^{12}C_2$ $^{12}C^{14}N$ $^{12}C^{14}N$
^{27}Al	Fuel cladding	$^{11}B^{16}O$
^{28,29,30}Si	SiC, Alloy	$^{14}N_2$, $^{12}C^{16}O$, $^{14}N^{1}_{2}H$, $^{14}N^{16}O$
^{42,43,44}Ca	Reduction of U metal, surface contaminant	$^{26}Mg^{16}O$, $^{27}Al^{16}O$, $^{28}Si^{16}O$, $^{12}C^{16}O_2$
^{47,49}Ti	Structure, H getter	$^{30}Si^{16}O^{1}H$, $^{14}N^{16}O^{1}_{2}H$, $^{12}C^{35}Cl$, $^{32}S^{16}O^{1}H$,$^{14}N^{35}Cl$, $^{33}S^{16}O$
^{51}V	Alloy, Corrosion resistance	$^{35}Cl^{16}O$, $^{34}S^{16}O^{1}H$
^{52,53}Cr	Alloy, Corrosion resistance	$^{35}Cl^{16}O^{1}H$ $^{40}Ar^{12}C$, $^{37}Cl^{16}O$
^{55}Mn	Alloy, Corrosion resistance	$^{40}Ar^{14}N^{1}H$, $^{23}Na^{32}S$
^{57}Fe	Structure	$^{40}Ar^{16}O^{1}H$, $^{40}Ca^{16}O^{1}H$, $^{23}Na^{32}S$
^{60,61,62}Ni	Alloy	$^{44}Ca^{16}O$
^{59}Co	Alloy	$^{43}Ca^{16}O$, $^{42}Ca^{16}O^{1}H$, $^{24}Mg^{35}Cl$
^{60,61,62}Ni	Structure	$^{44}Ca^{16}O$, $^{43}Ca^{16}O^{1}H$, $^{45}Sc^{16}O$, $^{46}Ti^{16}O$
^{63,65}Cu	Structure, Waste	$^{40}Ar^{23}Na$, $^{47}Ti^{16}O$, $^{40}Ca^{23}Na$, $^{12}C^{16}O^{35}Cl$
^{66,67,68}Zn	Alloy	$^{48}Ti^{16}O$, $^{50}Ti^{16}O$, $^{34}S^{16}O_2$, $^{35}Cl^{16}O_2$, $^{35}Cl^{16}O_2$
^{69}Ga	Plutonium alloy	$^{53}Cr^{16}O$
^{90,91}Zr	Fuel Cladding, H getter	$^{84}Sr^{16}O$, $^{84}Kr^{16}O$, $^{85}Rb^{16}O$
^{93}Nb	Alloy	$^{77}Se^{16}O$
^{95,97}Mo	Fission Product, Structure, U-Mo fuel	$^{40}Ar^{39}K^{16}O$, $^{79}Br^{16}O$, $^{57}Fe^{40}Ar$, $^{40}Ar^{16}_{2}O^{1}H$
^{105}Pd	H getter	$^{45}Ar^{65}Cu$
^{107,109}Ag	Fission product	$^{91}Zr^{16}O$, $^{92}Zr^{16}O^{1}H$
^{111}Cd	Neutron absorber, Fission product	$^{95}Mo^{16}O$, $^{94}Zr^{16}O^{1}H$
^{117,118,119}Sn	Alloy	$^{102}Pd^{16}O$
^{121}Sb	SbBe neutron source	$^{105}Pd^{16}O$
^{127}I	Fission product	$^{111}Cd^{16}O$
^{140}Ce	Measure of burnup, CeO as Pu surrogate	$^{124}Sn^{16}O$
^{142,143,145,146}Nd	Measure of burnup	$^{126}Te^{16}O$, $^{127}I^{16}O$, $^{128}Te^{16}O$, $^{128}I^{16}O$, $^{129}Xe^{16}O$
^{147,149}Sm	Neutron absorber	$^{131}Xe^{16}O$, $^{133}Cs^{16}O$
^{151,153}Eu	Neutron absorber	$^{135}Ba^{16}O$, $^{137}Ba^{16}O$
^{155,157}Gd,	Neutron absorber	$^{141}Pr^{16}O$
^{177,178,179}Hf	Control rod, H getter	$^{161}Dy^{16}O$, $^{162}Dy^{16}O$, $^{163}Dy^{16}O$
^{182,183}W	Refractory	$^{166}Er^{16}O$, $^{167}Er^{16}O$, $^{168}Er^{16}O$
^{200,201,202}Hg	Contaminant	$^{184,185,186}W^{16}O$
^{203,205}Tl	^{235}U decay product	$^{187}Re^{16}O$, $^{189}Os^{16}O$
^{206,207,208}Pb	Coolant, Shielding	$^{190}Ir^{16}O$, $^{191}Ir^{16}O$, $^{192}Ir^{16}O$
^{209}Bi	Coolant	$^{193}Ir^{16}O$
^{232}Th	Fuel	None
^{234,235,238}U	Weapons, Fuel	$^{195}Pt^{40}Ar$, $^{198}Pt^{40}Ar$
^{239}Pu	Weapons, Fuel	$^{238}U^{1}H$

Table 3.1: Polyatomic interferences and some applications for isobaric interference-free analytes.

3.3 Samples

The steps taken to analyze the data followed the method given by Dr. Josh Wimpenny (LLNL). This approach is preferred over the Relative Sensitivity Factor method of Dr. David Weisz (LLNL) because it incorporates outlier rejection and internal normalization, but the methods are largely parallel. The RSF method is described in Section 7.3.

Novel nuclear forensics techniques were investigated at UC Berkeley and Los Alamos National Laboratory (Tremsin et al., 2013); (Losko et al., 2014); and (Spano et al., 2019). Using neutron tomography at the Los Alamos Neutron Science Center (LANSCE) Spallation source, researchers detected and mapped the locations of intentional tungsten doping in depleted uranium surrogate fuel pellets using 3-D neutron tomography. Neutron tomography offers a powerful capability but requires a neutron spallation source. Professor Hosemann provided analogues for this analysis.

3.4 Experimental

CRM 125-A, NIST glasses, tungsten metal, and five surrogate fuel pellets composed of depleted uranium (as UO_2) with tungsten impurities were analyzed. The primary objective was to investigate the five uranium pellets using laser ablation mass spectrometry to confirm the results of a previous neutron tomography experiment at Los Alamos National Laboratory.

Samples were placed in an ablation cell with helium as the transport gas. The Spectra-Physics femtosecond laser ablates material which is swept by the helium gas flow from the cell to the mass spectrometer. The mass spectrometer measures the mass-to-charge ratio of detected ions with a limit of detection of $\sim$ 800 ppb, which is more sensitive than the neutron tomography method (Tremsin et al., 2013). The mass spectrometry data serve as initial confirmation of the tomography results. Ablation occurred in continuous mode (1 Watt at 1 kHz), meaning the laser was not shuttered during translation. Continuous stage motion at a rate of either 2.5 or 5.0 mm/minute would yield a stable mass flow under ideal conditions, given that the repetition rate of 1 kHz was much too fast to produce individual peaks in the mass spectra, which took on order of 1 second to integrate.

Wimpenny Method

The steps to calculate calibration curves using the Wimpenny method are outlined in Section 7.2 of Appendix I. This approach was found to give the highest R^2 values, but ultimately failed to provide reasonable concentrations. The exact reasons for this failure are unknown but they could be related to the different matrices (Si for NIST glass and U for the LANL

samples). The Wimpenny method originally used the calculation of exponential decay of the signal rather than a continuous average, so this may have also contributed to the observed discrepanices in measured versus expected concentrations.

LANL Surrogate Pellets

The LANL surrogate PWR fuel pellets are cylindrical in shape. Laser ablation line scans were conducted along the axis and across one end face of each sample. Early work in pulsed mode can be seen in the images as a linear series of small craters. Strictly speaking, all work was in pulsed mode but the laser ran at 1 kHz which, for these studies, was effectively continuous. The pulsed mode referred to here means that the stage moved quickly from one location to the next, remained motionless for 30 seconds, then moved again, resulting in distinct craters. Continuous ablation left narrow trenches in the sample surface.

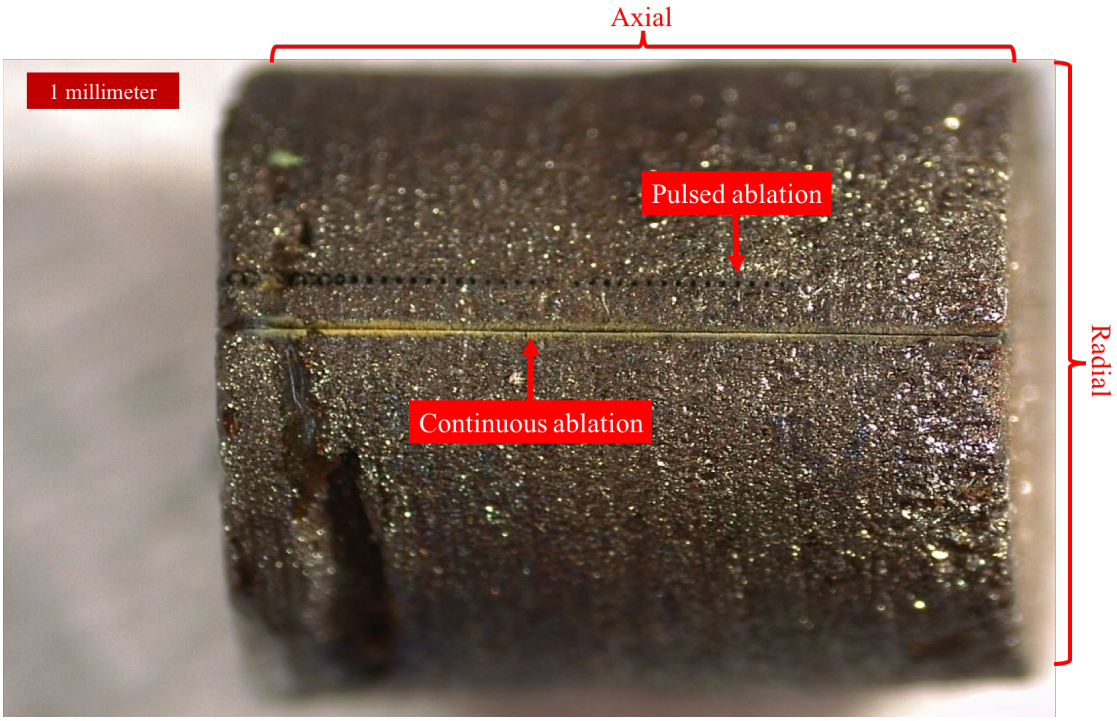

Figure 3.4: Definition of axial and radial orientations for the LANL surrogate fuel samples.

Special consideration was given to the LANL pellets because of radioactivity on the order of 1 microCurie. Laser ablation was conducted on each pellet using the Spectra-Physics femtosecond laser and Thermo-X inductively coupled plasma mass spectrometer. The laser pulse rate was 1 kHz at 1 mJ per pulse. In order to maintain As Low As Reasonably Achiev-

able (ALARA) exposure, the pellets were imaged only after ablation.

Actual radiant energy per pulse is then:

$1 \frac{\text{J}}{\text{s}} \cdot \frac{\text{s}}{1000} = 1$ mJ per pulse.

The spot size diameter is 30 μm, thus:

Spot area = π (1.5x10^{-5} cm)^2 = 7.1 x 10^{-6} cm^2

$\frac{1\text{mJ}}{7.1\text{x}10^{-6}\ \text{cm}^2} = 140.85\ \frac{\text{J}}{\text{cm}^2}$. This is well above the ablation threshold of common materials. For example, the ablation threshold for a 1 micrometer wavelength picosecond laser on stainless steel is less than 1 $\frac{\text{J}}{\text{cm}^2}$ (Liu et al., 2019).

The surrogate fuel pellets are right circular cylinders approximately 0.46 cm long and 0.5 cm in diameter. Runs are named by sample number and whether ablation occurred on the long axis of the pellet ('Axial') or across the diameter of one end ('Radial'). Table 3.2 shows experimental parameters.

Experimental Parameters	
Laser power	∼0.7 Watts at target
Laser repetition rate	1 kHz
Helium gas flow rate	624 mL per minute
Pulsed ablation	Shutter open for 2 seconds, manually activated using stopwatch
Continuous ablation	Stage translates at 2.5 mm or 5 mm per minute.

Table 3.2: Experimental parameters for mass spectrometry of CRM 125-A, NIST glass, tungsten wafer, and LANL samples.

The following results were plotted as a function of position only for continuous runs because the pulsed runs had slight variations in time between translation. Some unexpected elements such as gadolinium and neodymium, may have been present in certain samples. Samples 2 and 3 in this study contained the widest array of elements and represent the most interesting cases for this effort. These were compared against the neutron tomography images obtained at LANSCE. The method for neutron tomography includes high-speed electronic gating to determine the velocity of the neutrons. The ruling equations follow from a consideration of energy and momentum (Vogel, 2021):

$$\text{p}_{\text{classical}} = \text{mv} = \text{m}\frac{\text{L}}{\text{t}} \tag{3.1}$$

$$\mathrm{p_{quantum}} = \hbar \mathrm{k} = \frac{h}{2\pi}\frac{2\pi}{\lambda} = \frac{h}{\lambda} \tag{3.2}$$

$$\text{but } \mathrm{p_{classical}} = \mathrm{p_{quantum}}, \text{therefore:}$$

$$\mathrm{m}\frac{\mathrm{L}}{\mathrm{t}} = \frac{h}{\lambda} \tag{3.3}$$

Solving for lambda:

$$\lambda = \frac{h\mathrm{t}}{\mathrm{mL}} \tag{3.4}$$

$$\mathrm{E} = \frac{\mathrm{p}^2}{2\mathrm{m}} = \frac{\mathrm{m}^2\mathrm{L}^2}{2\mathrm{m}\ \mathrm{t}^2} = \frac{\mathrm{m}\ \mathrm{L}^2}{2\mathrm{t}^2} = \frac{1}{2}\mathrm{mv}^2 \tag{3.5}$$

Thus, if mass m, distance traveled L, and time t needed to travel distance L are known, the wavelength λ and energy E of the neutron can be determined. Since the neutron mass and distance traveled are known, time of flight is the only measurement needed. These measurements were made at the Los Alamos National Laboratory Lujan Neutron Scattering Center (LANSCE) facility. These femtosecond laser ablation mass spectrometry experiments were conducted to confirm the neutron tomography results.

Five surrogate fuel pellets of depleted uranium were received from Professor Hosemann at the University of California, Berkeley. They were fabricated as three batches of fuel pellet surrogates at Los Alamos National Laboratory (LANL) with intentional variations in density, tungsten inclusions (as wires and particles), and polymethylmethacrylate (PMMA) inclusions to simulate voids. These five samples represent aliquots from each category, though density and voids were not quantified in this study (Tremsin et al. (2013); Spano et al. (2019)). The purpose of this study was to quantify the elements present in the surrogate fuel pellets using LAMS as a reference against neutron tomography studies conducted at LANL. Tungsten was a known inclusion, though mass-to-charge ratios corresponding to gadolinium, zirconium, and several other elements were observed.

Chapter 4

Results

Results from four campaigns are given below. CRM 125-A is a Certified Reference Material produced by New Brunswick Laboratory and was used as a basic measure of system accuracy via the isotope ratios. NIST glass calibration curves show that the system is capable of analysis across a broad range of elements, making it competitive with Energy Dispersive X-Ray Spectroscopy (EDX) and similar techniques. The tungsten wafer provides confirmation of accuracy by producing natural isotopic abundance. Lastly, the surrogate fuel samples provided by Los Alamos National Laboratory were analyzed to confirm the neutron tomography results obtained at the Los Alamos Neutron Science Center (LANSCE).

4.1 CRM 125-A

(Rolison et al., 2017) found that CRM 125-A provides values within experimental error and verified that it can be used with confidence. The data in Table 4.1 show that the system as built is capable of determining isotope enrichment to within 1% and confirm system stability over several weeks.

CRM 125-A, 60 mW, 1 mm per minute translation	
Run	^{235}U / ^{238}U
1	0.043
2	0.042
3	0.043
4	0.042
5	0.043
Average	0.043 ± 0.001
Declared value (Kraiem et al., 2013)	0.042301 ± 0.000025

Table 4.1: Isotope ratios for CRM 125-A showing long-term stability of the laser and mass spectrometer across different surface areas over time.

Multiple runs were completed at low laser power (20 mW to 100 mW) to obtain the ^{235}U signal in pulse counting mode while simultaneously obtaining ^{238}U in analog mode (threshold at approximately 2 million counts per second according to the manufacturer). Five out of six runs showed an isotope ratio within the error of the reported value and all within 1%, showing that analog and pulse counting modes record counts per second with sufficient accuracy for these experiments. Table 4.2 shows uranium isotope ratios within expected tolerance, demonstrating reliable pulse counting mode for the ^{235}U signal and analog mode for the ^{238}U signal.

CRM 125-A detection in pulse and analog mode	
Laser Power (mW)	^{235}U / ^{238}U
60	0.043
60	0.043
60	0.031
50	0.043
50	0.042
50	0.042
Average	0.041 ± 0.005
CRM 125-A Published value (Kraiem et al., 2013)	0.042301 ± 0.000025

Table 4.2: CRM 125-A comparison between pulse and analog mode for the MS detector. The counts per second for ^{238}U are in the range for analog detector operation, while the ^{235}U counts per second fall in the pulse counting range. The ^{235}U / ^{238}U ratio remains within 1% of the declared value.

This marked the culmination of the CRM 125-A experiment and shows that the system is capable of 1% accuracy in the ^{235}U / ^{238}U ratio, sufficient for this study.

4.2 NIST Glass

With the basic characteristics of the LAMS system established, the next step was to establish calibration curves for elements of interest. NIST Standard Reference Materials (SRM) 610, 612, and 614 were used to develop calibration curves. The SiO_2 matrix of the NIST SRMs is not directly comparable to the UO_2 matrix of the LANL samples, but curves of sufficient accuracy for this study were developed. Table 4.3 shows the data used to build the NIST glass calibration curve for tungsten, plotted in Figure 4.1. These experiments show that the system can detect a broad spectrum of isotopes, offering advantages over complementary techniques such as EDX.

NIST Glass Calibration		
NIST glass	Counts per second	Declared W concentration [ppm]
610	$3x10^5$	444
612	$2x10^4$	38
614	401	0.806
Calibration curve	y [ppm] = 0.0013x [cps]	

Table 4.3: Calibration data of NIST glass for tungsten concentration in the LANL samples.

The data above are plotted in Figure 4.1 below to give the tungsten calibration curve based on NIST glasses.

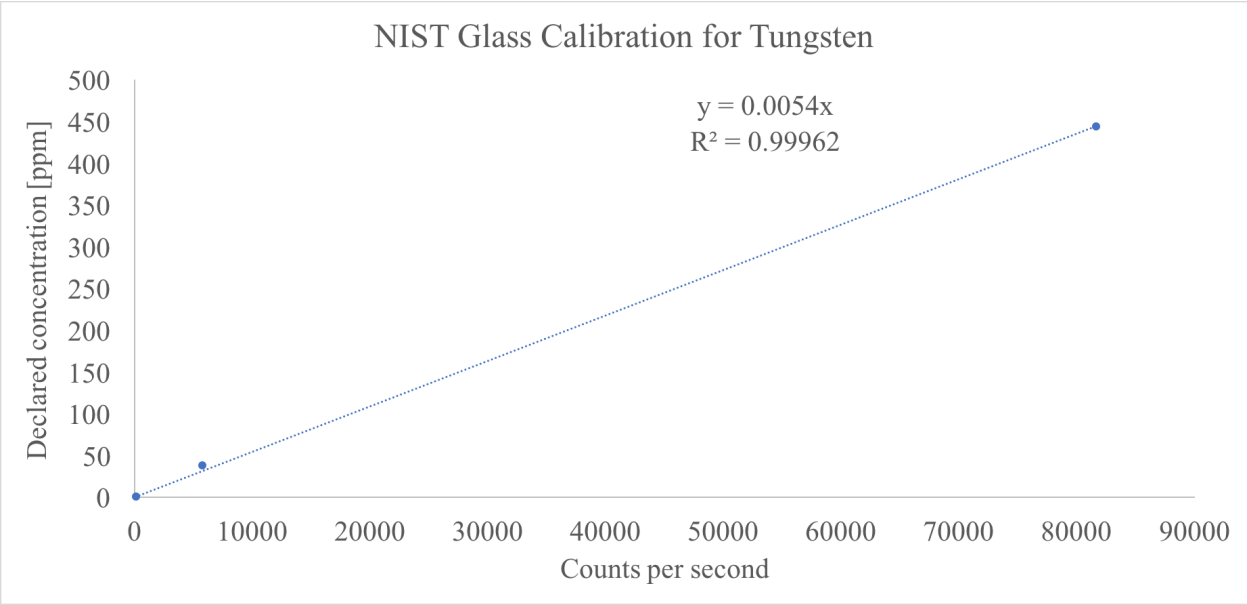

Figure 4.1: Calibration curve for tungsten in NIST glass.

The same process was used to build calibration curves for gadolinium, below, and several other elements of interest to the nuclear industry. The measured concentrations of the various elements are given in Table 4.11 of Section 4.4, below.

Calibration data for Gd in LANL samples		
610	449	$4x10^4$
612	37.3	$3x10^3$
614	0.763	46

Table 4.4: The calibration curve for Gd in the LANL samples based on NIST Glasses.

A calibration curve for Gd is given in Figure 4.2 below based on the data from Table 4.4 above.

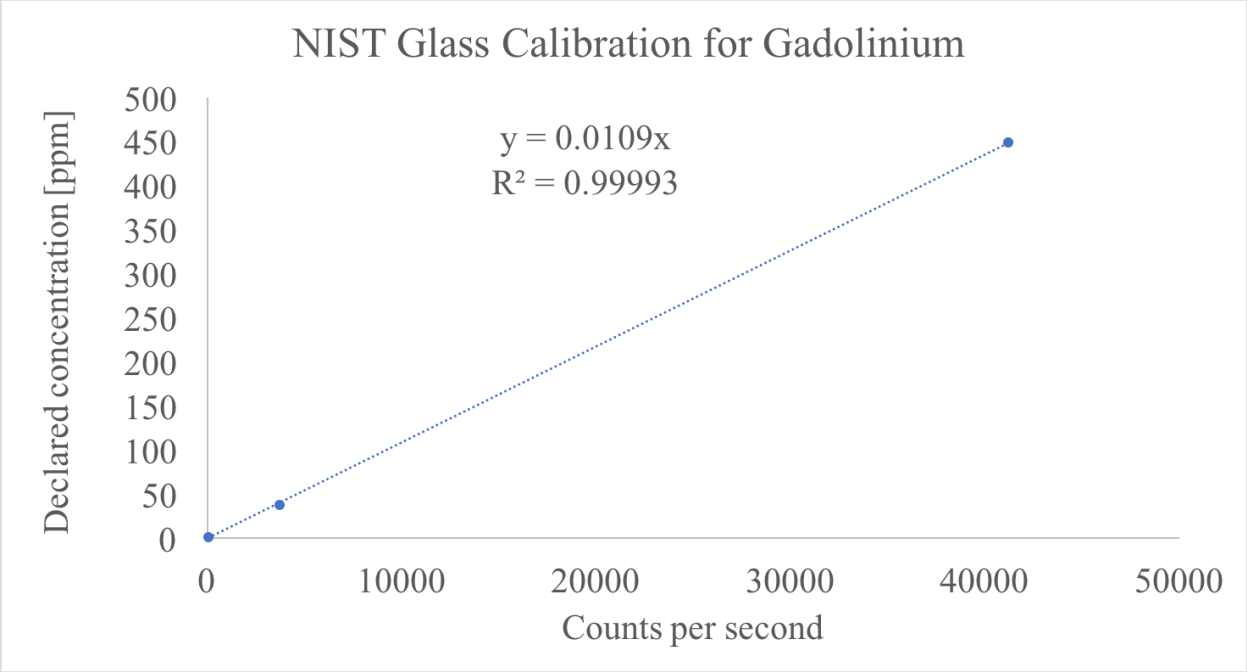

Figure 4.2: Calibration curve for gadolinium in NIST glass.

The data were processed using three calibration methods: Relative Sensitivity Factors, the Wimpenny method, and Counts-per-second versus Declared concentration. The method to calculate the Relative Sensitivity Factor is given in Appendix 7.3. An initial NIST glass experiment yielded high R^2 values for an array of elements by the Wimpenny method, which is outlined in Appendix 7.2. Calibrations are given in Appendix **??**. Next, a tungsten wafer was analyzed to provide a 100% pure tungsten calibration point.

4.3 Tungsten Wafer

A second calibration curve was developed for the element tungsten. The curve was based on a pure tungsten wafer and the tungsten value for CRM 125-A from the work of (Bavio et al., 2019). This two-point calibration curve was developed because of the difficulties encountered using NIST glasses to build reasonable curves. The issues included learning to use the system repeatably, helium gas flow, mass spectrometer settings, and sample positioning. The second calibration curve for tungsten differs slightly from that of the NIST glasses but is adequate for this initial effort. This second calibration curve is shown in Figure 4.3.

The data in Table 4.5 show that polyatomic interferences are negligible in this study because all isotopes reflect expected natural abundances. This adds confidence in the basic perfor-

mance of this LAMS system.

Tungsten Wafer Isotope Fractions					
Run	180	182	183	184	186
1	0.0011	0.2576	0.1422	0.3062	0.2929
2	0.0011	0.2573	0.1423	0.3062	0.2930
3	0.0011	0.2575	0.1425	0.3060	0.2929
Average	0.0011 ±0	0.2575 ±0.0002	0.1423 ± 0.00015	0.3062 ± 0.03148	0.2929 ± 0.0001
Natural fraction	0.00120	0.26500	0.14310	0.30640	0.28430

Table 4.5: Isotope ratios as measured by LAMS on a tungsten wafer. The close matches for all isotopes indicate that polyatomic and isobaric interferences are acceptably low (<1%).

Table 4.6 uses counts per second from ^{183}W converted to whole tungsten: 9.2x10^8 x $\frac{1}{0.2653}$ = 3.5x10^9 counts per second. This gives a second approach to determining the concentration of tungsten in the LANL samples.

Tungsten Wafer Calibration		
Tungsten wafer	Whole W Counts per second	Declared W concentration [ppm]
Tungsten wafer	3.4x10^9	10^6
CRM 125-A	3435	0.895
Calibration equation	y [ppm] = 0.0003x [cps]	

Table 4.6: Data from the tungsten wafer and CRM 125-A used to develop a second tungsten calibration curve.

Figure 4.3 below gives the calibration curve based on the data from Table 4.6 above.

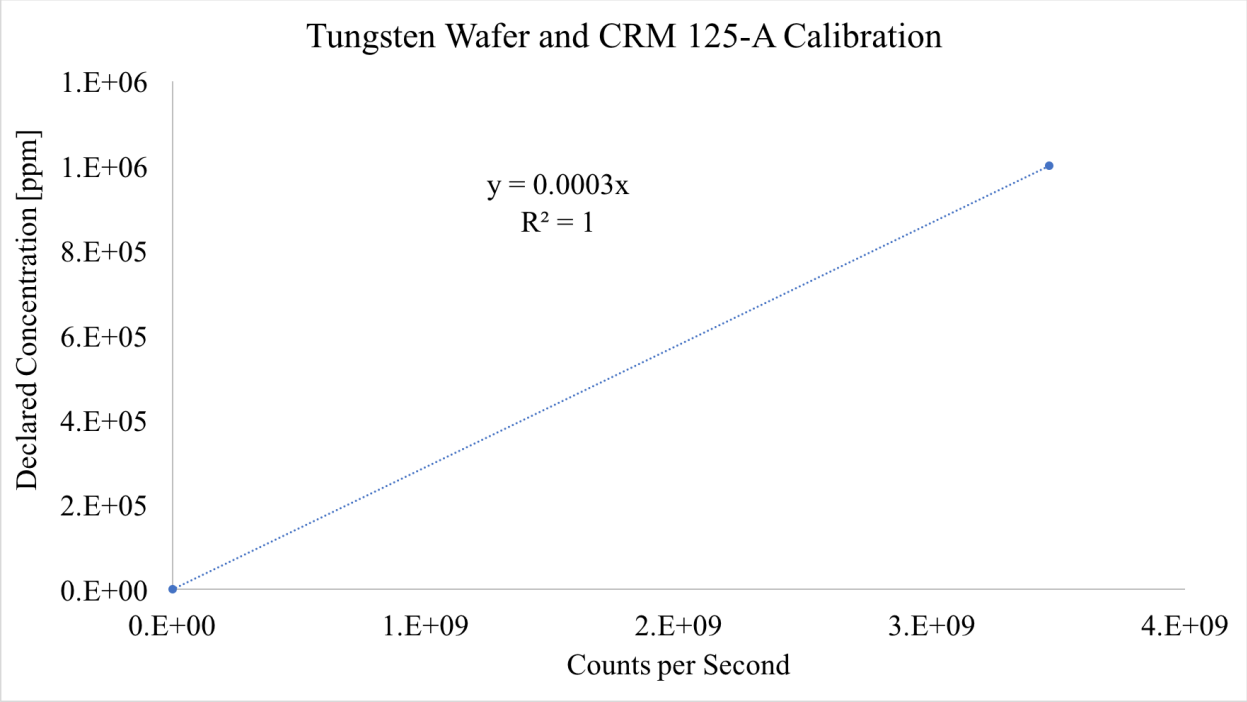

Figure 4.3: Calibration curve using a tungsten wafer and CRM 125-A, based on (Bavio et al., 2019).

Figures 4.1 and 4.3 compare the calibration curves generated from the NIST glasses and from the tungsten wafer with CRM 125-A. The two calibration curves are close but distinct, with the curve from the NIST glass providing slightly more accurate results for tungsten.

4.4 LANL Surrogate Fuel Pellets

The LANL surrogate fuel pellets were treated as unknown samples and analyzed for a variety of elements relevant to the nuclear industry. Appendix 7.5 catalogues optical microscope images of each pellet showing the effects of ablation. Table 4.8 shows the differences in concentration between axial and radial transects in the isobaric interference-free isotopes of Gd. This suggests that gadolinium was not spread uniformly throughout Sample 2, which was the most complex of the five. Gd may have been heterogeneously doped into the sample. The same holds for tungsten. ^{155}Gd and ^{157}Gd are used as neutron absorbers in power reactors (Chow et al., 2012). Table 4.10 lists elements relevant to the nuclear industry that were detected in the LANL samples.

Figure 4.4 shows the $\frac{^{235}\mathrm{U}}{^{238}\mathrm{U}}$ signal along the axis of Sample 1, demonstrating the long-term stability of the system and further demonstrating that Sample 1 is not a graded form.

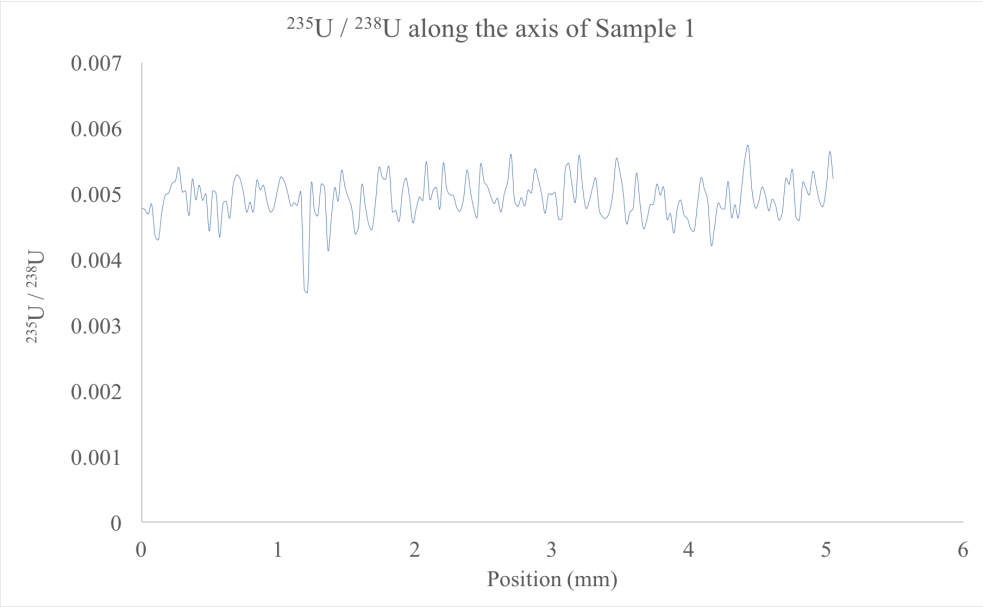

Figure 4.4: $\frac{^{235}\mathrm{U}}{^{238}\mathrm{U}}$ under continuous ablation along the axis of Sample 1, showing acceptable stability over time.

$$\frac{\text{Average signal for specific isotope}}{\text{Sum of average signals for all isotopes measured of a given element}} = \frac{\mathrm{m_i}}{\sum_1^{\mathrm{n}} \mathrm{m_n}} \tag{4.1}$$

For:

m = Isotope mass
i = The i^{th} index of n measured isotopes of mass m
n = Range of isotopes 1 through n as listed in the table

This calculation was done for the two isotopes of gallium below. Low-confidence calibration curves for select elements of interest to the nuclear enterprise are shown below.

Table 4.7 gives the uranium isotope fraction on the axis of Sample 2, showing good agreement with the declared depleted value of 0.004.

Uranium isotope fraction in Sample 2 Axial		
Uranium	235	238
Measured Ratio	0.0038	0.9962
Actual Ratio (Hosemann, 2022)	0.0040	0.9960
Natural Ratio	0.0072	0.9938

Table 4.7: Uranium isotope fraction in Sample 2.

The differences between isotope ratios from continuous versus pulsed ablation were negligible. The ^{235}U fraction under continuous ablation was measured as 0.0046 versus 0.0038 from pulsed ablation, see Table 4.12. A different approach measuring the exponential decay of the ion signal over time could yield more accurate results. However, for the purpose of this study, continuous ablation was easier to convert from time to position and was used for most analyses.

The LANL samples were delivered with only basic information regarding their provenance. Many elements were found in the samples (See Table 4.10), with gadolinium below as one example. In situations where not all isotopes were measured, the expected fractions were calculated according to the following mass fraction relation:

Gd	155	157
Axial	Not detected	Not detected
Radial	0.1816	0.180
Natural	0.187	0.197

Table 4.8: Gadolinium isotope fractions as measured by LAMS on Sample 2. Note that gadolinium was seen radially but not axially, implying a heterogeneous distribution throughout the sample.

The following tables show various isotope fractions as measured by LA-ICP-MS in Sample 2, the most complex of the five. The results illustrate the complex nature of the samples, with small implants of tungsten and several other elements. LAMS successfully identified a suite of elements suggested by neutron tomography. Other elements, including Ce, Hf, Nd, Pb, and Zr, were also identified by LAMS but were not seen in the neutron tomography study, see Table 4.10.

Pb isotope fractions in Sample 2 Axial		
Isotope	206	208
Abundance	24.1	52.4
Natural ratio	0.315	0.685
Measured ratio	0.305	0.695

Table 4.9: Pb isotope fractions as measured in Sample 2 Axial showing agreement within 1% of declared values.

Table 4.10 shows elements corresponding to measured mass over charge found in each sample, with low signals ($< 1{,}000$ counts per second, but signal-to-noise > 5) denoted by parentheses. Table 4.11 shows the concentration of selected elements detected along the diameter of one end of Sample 3, which had the greatest diversity of elements.

Elements indicated by mass over charge in samples		
Sample	Axial	Radial
1	Zr, Ce, W	Ce, (W)
2	(Zr), W, Hg, Pb, Ce, (Hf), (Gd), (Tl), (Nd)	Zr, Gd, W
3	W, Zr, Ce, Hf	Zr, Gd, W, Hf, Nd, Ce, (Sm), Hg, Pb
4	(Ce), (W), Nd, Hf, (Zr)	Zr, Ce, Nd, Hf, W
5	(W), (Zr), Ce, (Pb)	W, Ce, Zr, (Pb), Nd

Table 4.10: Elements corresponding to measured $\frac{\text{mass}}{\text{charge}}$ by sample.

The concentration of select elements along the end diameter of Sample 3 exhibit a range of values, from Pb near the detection limit to tungsten at almost one percent. Calibration data were not taken for Hg or Sm.

Concentrations on one end of Sample 3	
Element	Measured concentration [ppm]
Gd	1
Zr	17
Hf	1
Nd	20
Ce	34
W	7,249
Pb	0.7

Table 4.11: Calculated concentration of selected elements across the end of Sample 3. The end of Sample 3 had the highest diversity of elements. Calibration data were not taken for Hg and Sm but their presence is indicated qualitatively by counts-per-second measured. Sm had less than 1,000 cps but the background was zero before and after the run, so Sm is considered present near the threshold of detection.

Table 4.12 below shows the axial and radial $\frac{235}{238}$ isotope ratio, indicating that the samples are composed of depleted uranium.

LA-ICP-MS of Depleted U Samples		
Pulsed		
Sample	Condition	Measured $\frac{235}{238}$
1	Axial	0.0040
1	Radial	0.0049
2	Axial	0.0050
2	Radial	0.0050
3	Axial	0.0047
3	Radial	0.0037
4	Axial	0.0046
4	Radial	0.0046
5	Axial	0.0048
5	Radial	0.0048
Pulsed Average		0.0046 ± 0.0004
Continuous		
Sample	Condition	Measured $\frac{235}{238}$
1	Axial	0.0040
1	Radial	0.0038
2	Axial	0.0038
2	Radial	0.0038
3	Axial	0.0049
3	Radial	0.0036
4	Axial	0.0037
4	Radial	0.0036
5	Axial	0.0041
5	Radial	0.0045
Continuous Average		0.00398 ± 0.00042

Table 4.12: Measured $\frac{^{235}\mathrm{U}}{^{238}\mathrm{U}}$ for each sample from pulsed and continuous ablation. The data in this table show that there is no fundamental difference between the two. However, continuous ablation is easier to process and was used for the rest of the experiments. The accepted $\frac{^{235}\mathrm{U}}{^{238}\mathrm{U}}$ value is 0.004 (Hosemann, 2022).

The average ^{235}U / ^{238}U ratios along the axis of Sample 1 are within 1% between pulsed and continuous modes. The comparison to the previous run of 0.0040 in March 2020 is also within 1% agreement, demonstrating the long-term stability of the LAMS system.

Tungsten Isotopes in LANL Samples

Table 4.13 shows tungsten isotopes at a point on the axis of Sample 1. According to (Tremsin et al., 2017), the LANL samples contain various impurities such as tungsten wire. These impurities can be detected using LAMS, as shown below.

$\frac{183}{182}$W isotope ratios in LANL Samples	
Sample	$\frac{183}{182}$
1	0.54
2	0.55
3	0.54
4	0.55
5	0.54
Natural ratio	0.5400

Table 4.13: The tungsten isotope ratios in the LANL Samples show close agreement with those of natural tungsten.

The LANL samples contain intentional impurities, primarily tungsten. Table 4.13 shows that the tungsten added to the samples reflects a natural isotopic composition. ^{182}W and ^{183}W have no major isobaric interferents. Table 4.15 shows the peak axial tungsten concentrations in the LANL samples.

Table 4.14 gives the maximum tungsten concentration along the axis of each LANL sample using the NIST calibration curve.

Measured average tungsten concentration in LANL samples (ppm = 0.0013 cps)		
LANL Sample	Counts per second	Calculated concentration
1	$2.6x10^5$	0.13 a%
2	$1.3x10^6$	1.9 a%
3	$1.7x10^6$	0.85 a%
4	1,253	6.14 ppm
5	2,020	9.9 ppm

Table 4.14: The calculated concentration in each LANL sample based on the NIST calibration curve. The results match LANL's statement that Samples 2 and 3 contain the highest concentrations.

The distribution of tungsten within a given sample is seen to be highly asymmetric in three different aspects. First, as a function of position along a given axis. Second, as a difference between axial and radial locations within a given sample. Third, as a difference between various samples. The samples are reported to have various tungsten impurities, such as small bits of wire, doped into them. The vaiation in surface roughness between samples and the presence of a hollow core in some samples indicates wide variability. Table 4.15 below shows the peak tungsten concetration along the axis of each LANL sample. These can be compared to the mass spectra beginning with Figure 4.5 beginning on page 72.

Peak axial tungsten concentration* in LANL samples		
Sample	CPS	W [ppm]
1	$3.4x10^5$	444
2	$1.9x10^7$	25,311
3	$3.6x10^6$	4,700
4	22,310	29
5	2,020	2
*NIST calibration curve: (ppm = 0.0013 cps)		

Table 4.15: Peak tungsten concentration measured along the axis of LANL samples.

In summary, the $\frac{\text{mass}}{\text{charge}}$ ratios corresponding to the listed elements demonstrate the higher elemental sensitivity of LAMS compared to neutron tomography. Table 4.12 shows the background-subtracted average $\frac{^{235}\text{U}}{^{238}\text{U}}$ ratio for each sample, illustrating the difference between pulsed and continuous ablation ratios. Continuous ablation was slightly easier to process and was used exclusively for the remaining experiments.

The images below show the laser ablation tracks along the surrogate fuel pellets with the corresponding mass spectra. The key point with the spectra is that the variation in tungsten concentration suggests that small amounts of tungsten were doped into Samples 2 and 3, as expected. Figure 4.5 shows an early increase in tungsten along the axis of Sample 1, implying a tungsten impurity at the surface.

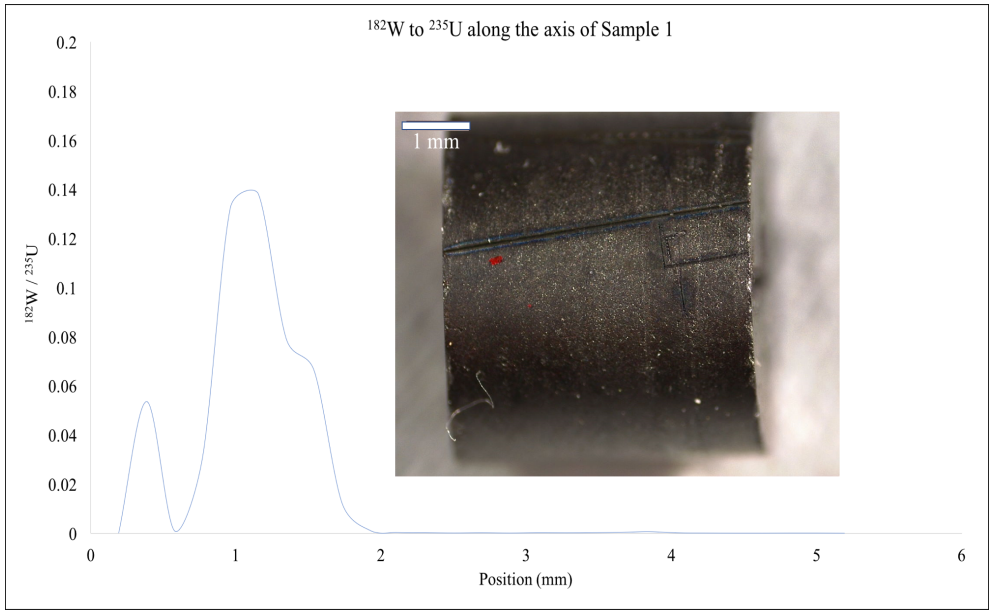

Figure 4.5: Tungsten under continuous ablation along the axis of Sample 1 indicating increased concentration at one end.

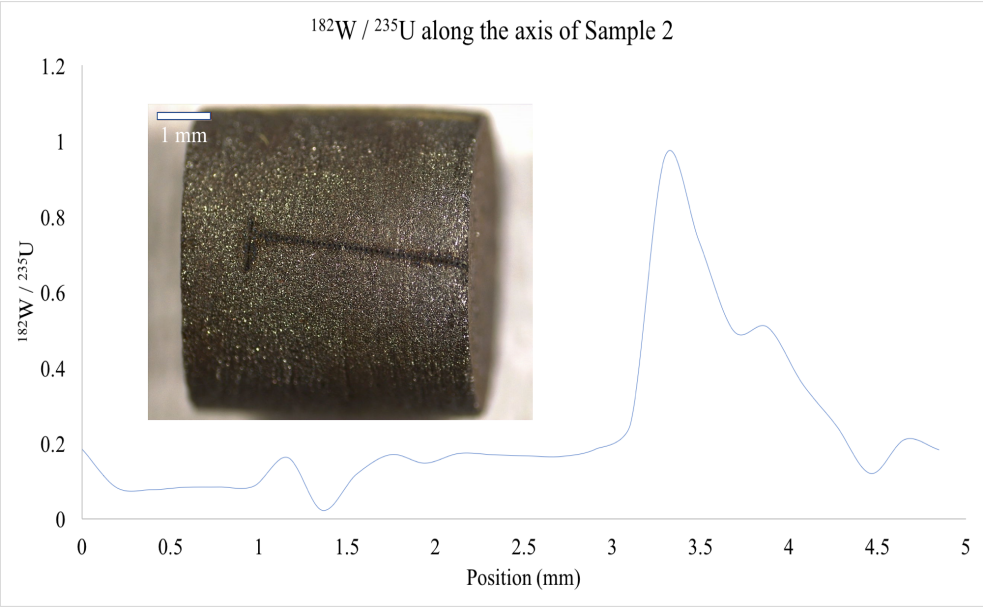

Figure 4.6: Tungsten under continuous ablation along the axis of Sample 2.

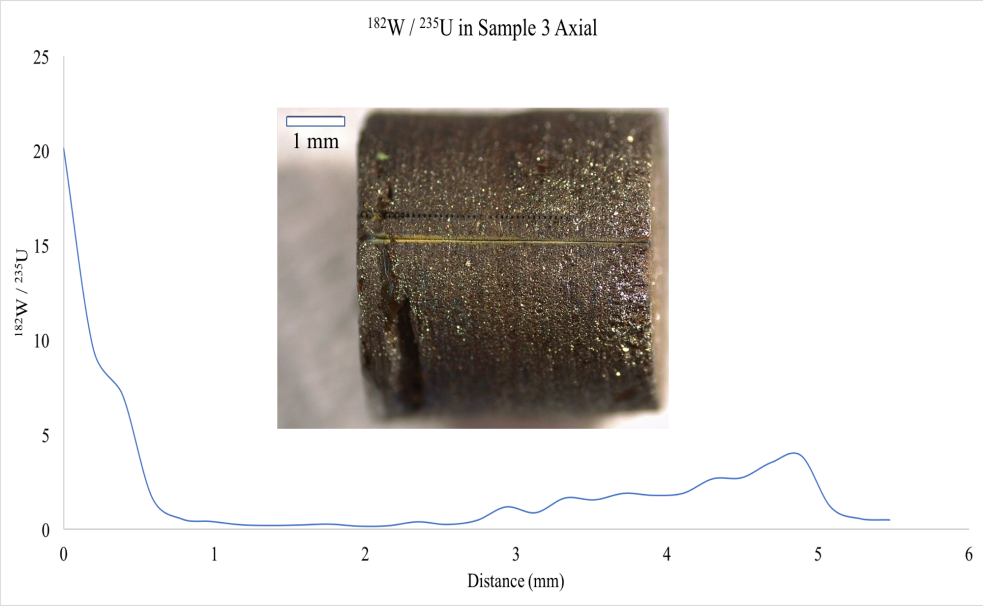

Figure 4.7: Tungsten under continuous ablation along the axis of Sample 3.

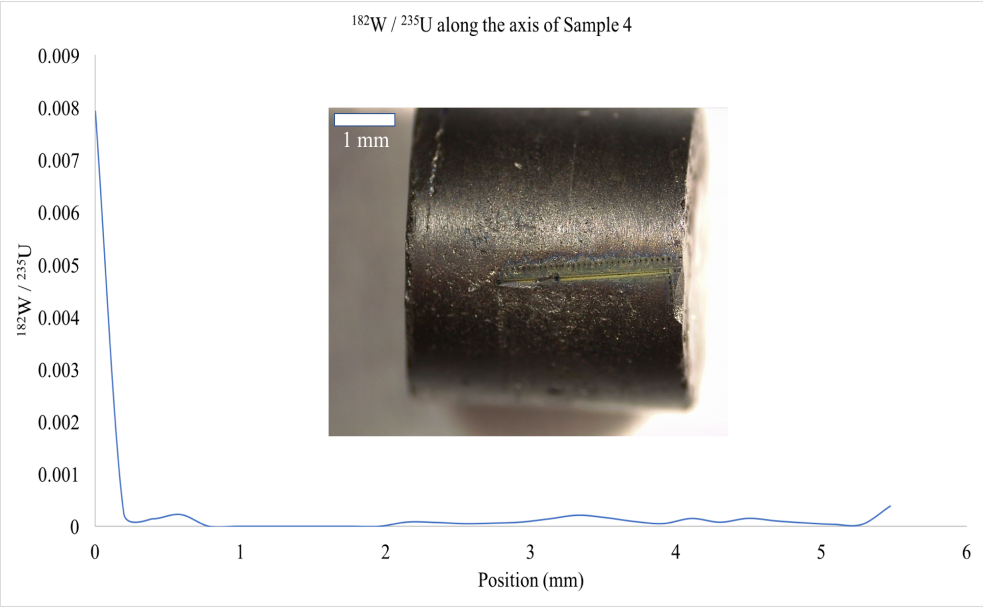

Figure 4.8: Tungsten under continuous ablation along the axis of Sample 4.

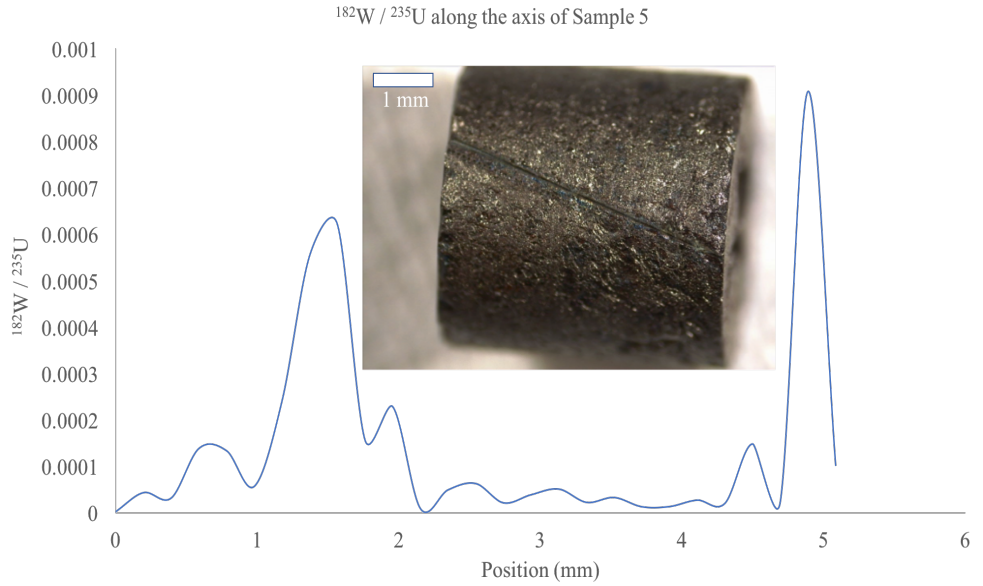

Figure 4.9: Tungsten under continuous ablation along the axis of Sample 5.

Figures 4.6, 4.7, and 4.9 (Samples 2, 3, and 5, respectively) indicate elevated tungsten along the ablation track. Samples 2 and 3 were expected to contain elevated tungsten levels but tungsten was detected in all five samples. Surface contamination is unlikely but cannot be ruled out. Figures 4.7 and 4.8 show immediately elevated tungsten levels that would be

expected with diffusion from the tungsten hot plate into the samples. This is taken as an external source of tungsten and not as an example of intentional doping. However, other indications, such as the EDX spectrum showing tungsten mid-axis on sample 2 indicates possible doping.

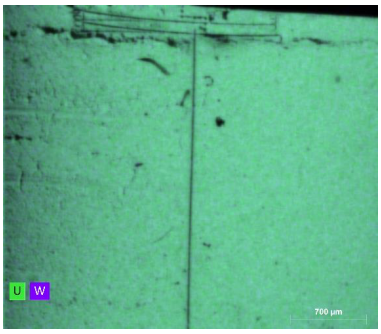

(a) Uranium and tungsten mapped with EDX in Sample 1.

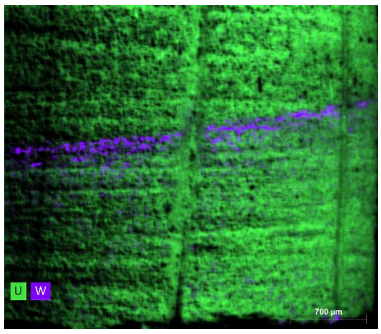

(b) EDX map of Sample 2 showing uranium and tungsten.

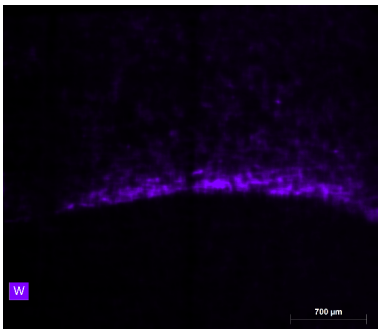

(c) EDX map showing tungsten in Sample 2.

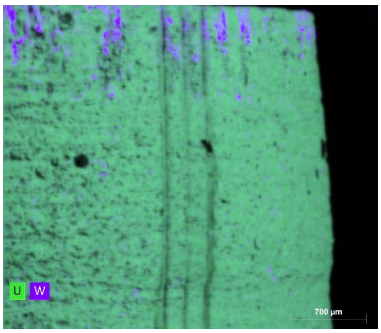

(d) EDX map of uranium and tungsten at one end of Sample 3.

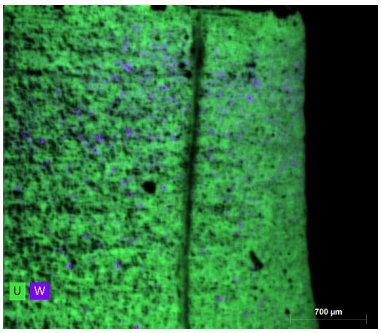

(e) EDX map of uranium and tungsten in Sample 3.

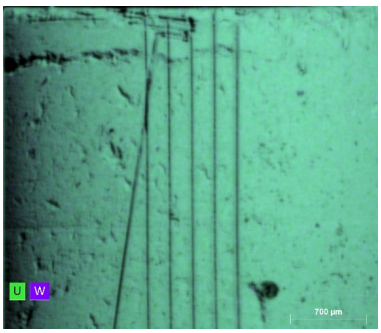

(f) EDX map of uranium and tungsten in Sample 4.

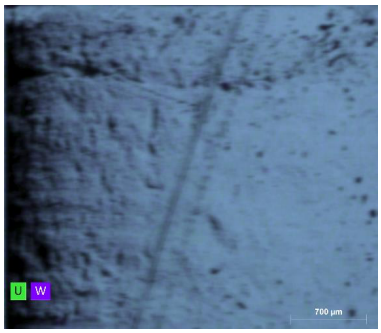

(g) EDX map of uranium and tungsten in Sample 5.

Figure 4.10: EDX images and one spectrum of the five LANL samples. Note the tungsten signal near the middle of the pellet in Images 4.10b and 4.10c. This rules out the hypothesis of diffusion of tungsten from the hot plate into the pellet. Images courtesy of Peter Boone, UCB/LLNL.

Figure 4.11 below shows an EDX spectrum for Sample 3, indicating the presence of tungsten. LAMS was able to detect a strong tungsten signal in Sample 3 as shown in Table 4.15 on

page 71.

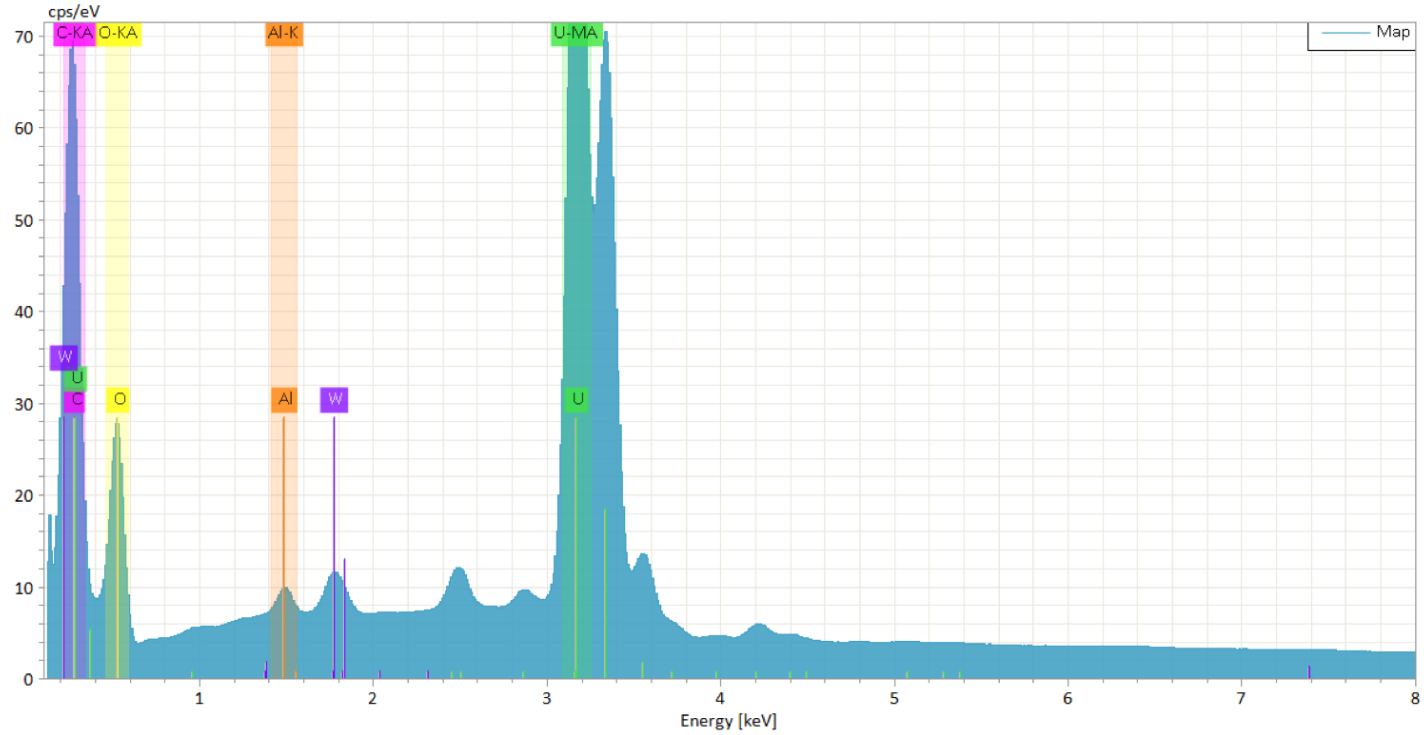

Figure 4.11: EDX spectrum of Sample 3 showing a modest tungsten signal. This demonstrates the power of LAMS, which had a strong average tungsten signal for Sample 3.

Figure 4.12 shows an EDS spectrum on NIST 610 glass, where major constituents such as calcium and sodium are only weakly apparent. LAMS offers better detection limits and isotopics than EDX. The light blue area surrounding the ablation track is most likely surface contamination from oxides of ablation debris rather than a heat-affected zone. The width of the debris from the trench was approximately 150 μm on either side. A separation of approximately 500 μm was used as a minimum separation distance, and often much more, up to several mm.

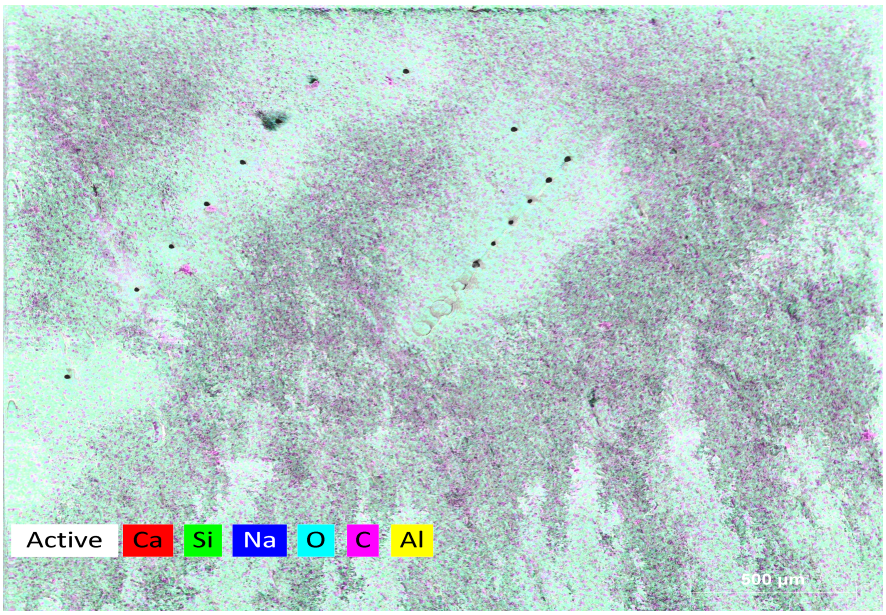

Figure 4.12: EDX map of NIST Glass 610 showing the debris field from laser ablation.

Figure 4.13 shows the SEM image corresponding to the EDX image in Figure 4.12. The debris from ablation is more easily seen under EDX analysis.

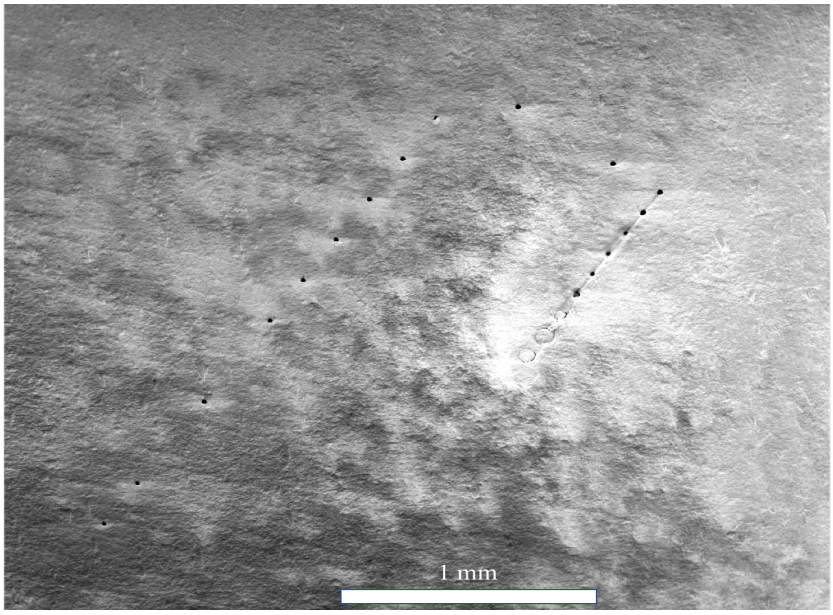

Figure 4.13: SEM image corresponding to Figure 4.12.

4.5 TRISO surrogate fuel particles

The final effort included surrogate TRISO particles from the UC Berkeley Materials Science inventory. Both whole particles and polished hemispheres were interrogated. Figure 4.14 shows preliminary ablation efforts on a whole surrogate TRISO particle (approximately 0.5 mm in diameter) secured by clear cellophane tape, which has been mostly ablated away, though its edge is still visible. One issue with the current stage configuration is the ability to orient the sample to the laser focus in the x, y, and z dimensions. At present, the only way to determine if the beam is in focus is to observe the brightness of the plasma formed during ablation.

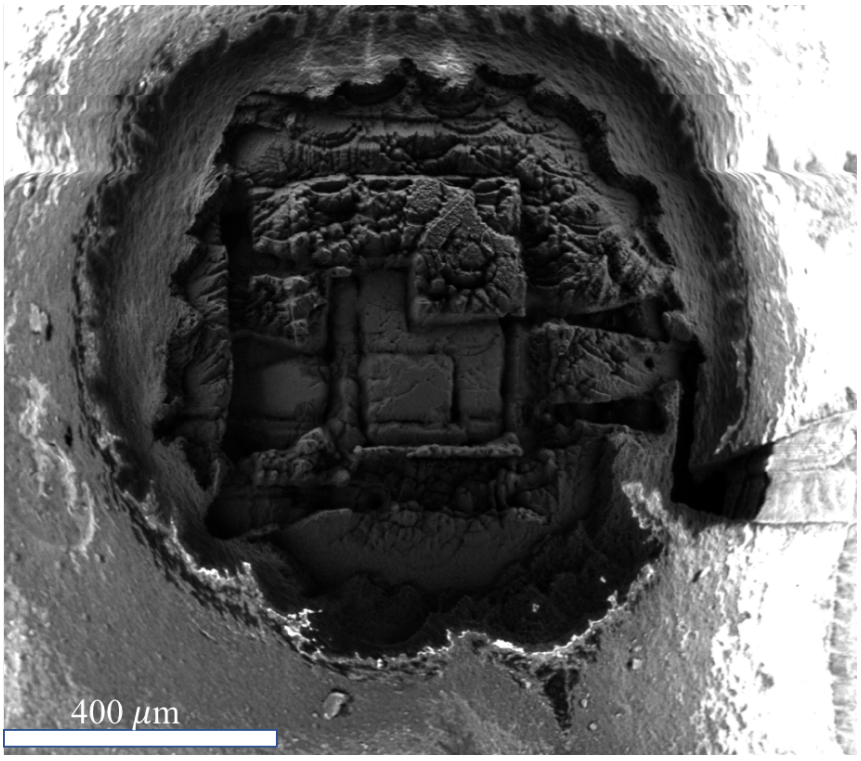

Figure 4.14: Initial effort to ablate an area of a surrogate TRISO particle.

The difficulty with sample position for the whole particle was alleviated by fixing the TRISO surrogate particle in epoxy and polishing. This provided a flat surface for ablation. Figure 4.15 shows ablation across the hemisphere of a surrogate TRISO particle. Femtosecond ablation removes much larger volumes of carbonaceous (pyrolytic carbon, epoxy) material compared to metals at equivalent power (see Figure 4.14). Though the experiments were only preliminary, the ability to ablate into the volume of TRISO particles is demonstrated. A method for securing the samples in the ablation chamber in a quantitative way so that the stage can be programmed in a repeatable manner would be needed for more advanced

work, but initial results are promising.

Figure 4.16 below shows that a large fraction of the surrogate TRISO core is composed of Hafnium.

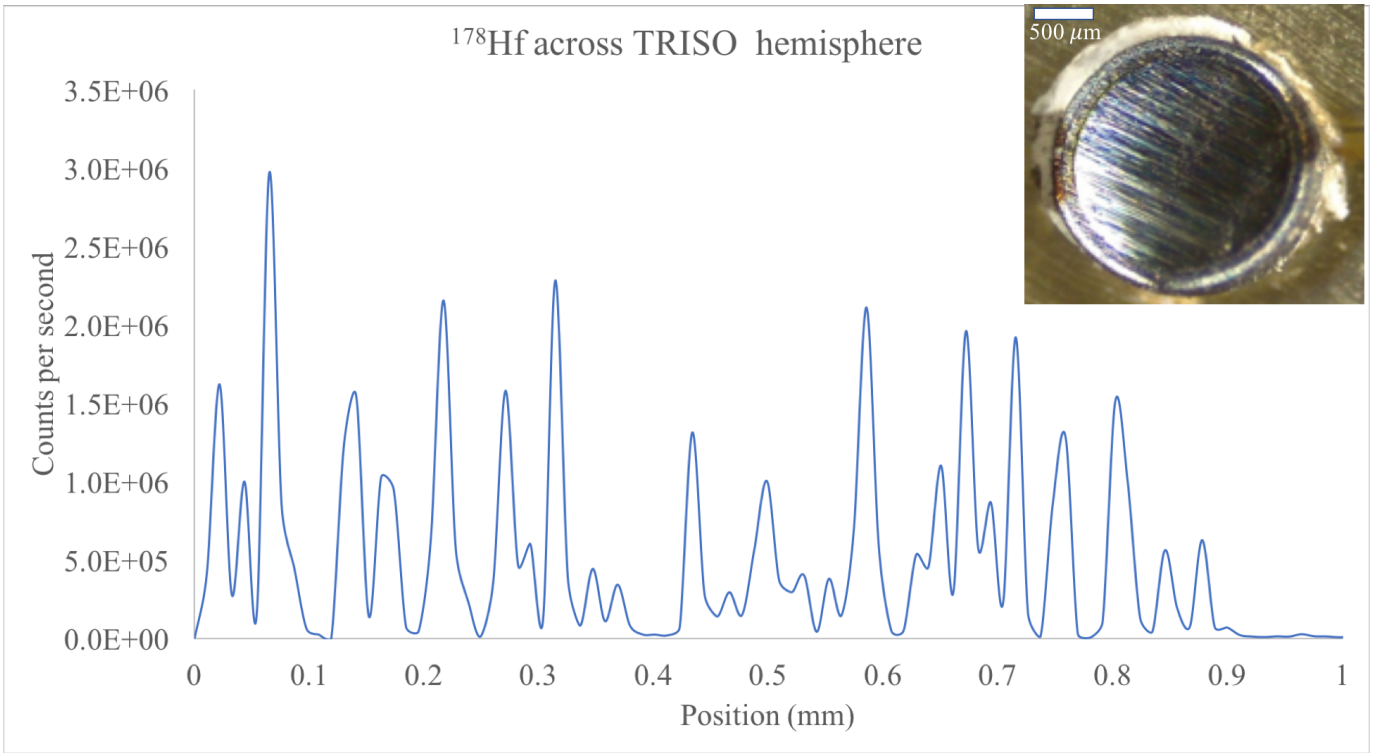

Figure 4.15: The isotope ^{178}Hf was found across the TRISO surrogate hemisphere, even though the laser had no observable impact on the surface.

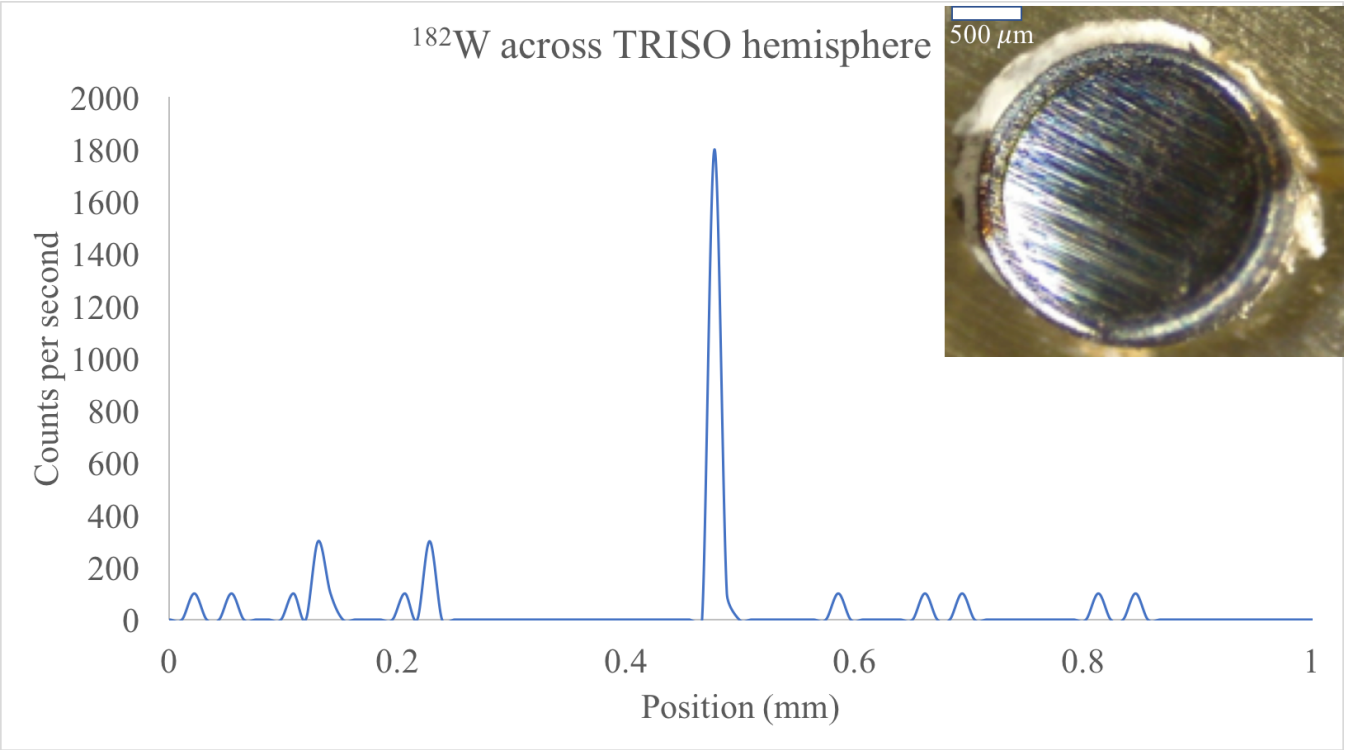

Figure 4.16: The isotope ^{182}W was found across the TRISO surrogate hemisphere, but at very low concentration. This could be an example of contamination.

To develop stable fuel, zirconium has been alloyed to hafnium and cerium, with the general formula $Ce_xHf_yZr_{1-x-y}O_2$. One such proportion is 15 mol% ceria and 40% hafnia, where ceria and hafnia refer to the oxides of each element and has been shown to improve fracture toughness (Becher & Funkenbusch, 1990). This specific sample of TRISO does not contain measurable quantities of cerium, but many experiments have been done with metal alloys in nuclear fuel (Janney, 2017). These samples may play a role in the testing and development of similar fuels.

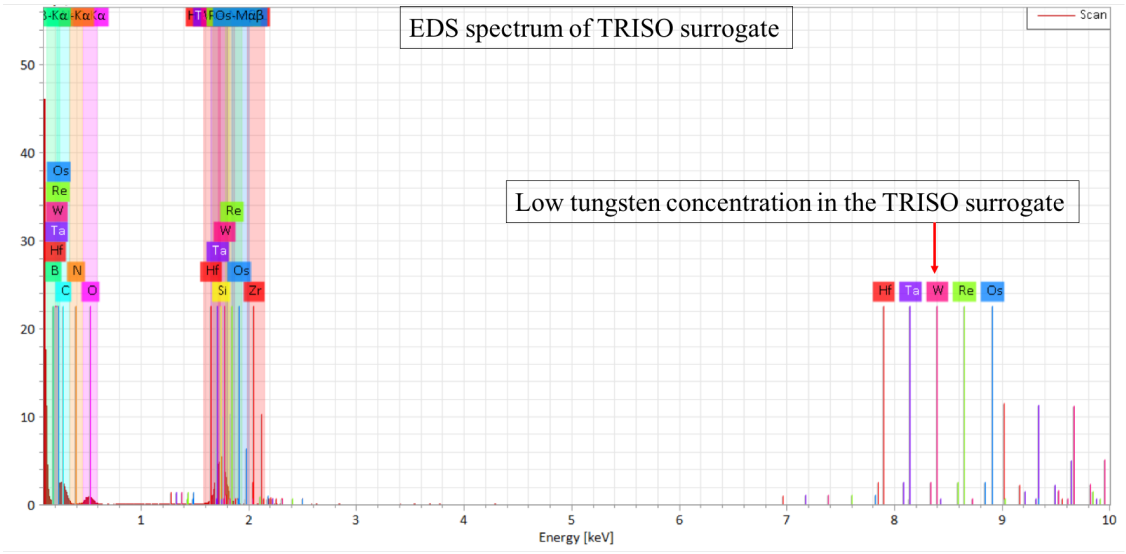

Figure 4.17: Typical EDX spectrum of surrogate TRISO showing the absence of tungsten in the TRISO surrogate, as confirmed by the mass spectrum in Figure 4.16.

Chapter 5

Discussion

The research hypothesis that a femtosecond laser could ablate material into a mass spectrometer and produce mass spectra as a function of laser position for standards, metals including uranium, and surrogate TRISO samples was demonstrated. A Spectra-Physics Ti:Sapphire laser coupled to a Thermo-X mass spectrometer was used to investigate the effectiveness of LAMS on various standards, tungsten metal, surrogate TRISO particles, and surrogate PWR fuel pellets. The system reproduced isotope ratios of uranium and tungsten to ± 1 a% and obtained calibration curves for NIST glass with R^2 better than 0.99. This is sufficient to determine the overall enrichment of the surrogate fuel (depleted uranium, 0.4% ^{235}U) and to detect gradients as a function of radius. ^{155}Gd and ^{157}Gd are used as neutron absorbers in power reactors. Both were detected across the end radius but not in significant amount ($<$ 1,000 cps) along the axis of LANL Samples 2, 3, and 4. Along with the other elements identified in Table 4.10, this shows the usefulness of LAMS compared to neutron tomography, which provides neither this level of sensitivity nor isotopic information.

The ability to drill into an intact TRISO particle was tested. With an alignment laser, full-thickness ablation (from the surface all the way through a sample) should be feasible given a known and repeatable starting position. The challenge is to account for any deviations in surface height that result from differences in ablation on subsequent passes while systematically drilling into the material. Either a feedback mechanism for the local height or an overdetermined ablation regime, in which more laser energy is delivered than is needed, could ensure smooth and complete surface vaporization. For cylindrical samples, a quantitative sample holder that ensures precise and repeatable alignment would allow the use of a pre-programmed ablation algorithm, which would almost certainly improve the quality of the data.

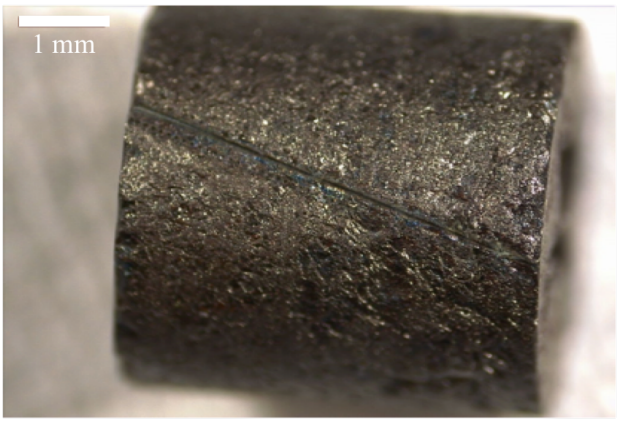

Figure 5.1: Optical microscope image of Sample 5 showing the effect of misalignment in the sample chamber. The LANL samples have a curved surface and the Schwarzschild optic results in a short Rayleigh length, so a small change in vertical position of the ablation surface results in a sharply reduced ablation signal.

System characterization and current limitations

The Spitfire laser was operated within stated limits of power and stability. The lens system remained largely unchanged over the course of work. The Schwarzschild objective reduced optical aberrations because it functioned as a mirror rather than a lens. The most important issue regarding the system configuration was the sample position and the ability to see the sample during trials. The ablation chamber was a few centimeters on a side and allowed some variability in sample placement. In order to produce the best data possible, the ablation chamber needs a sample holder precisely aligned to the axes of travel. Figure 5.1 shows one example of misalignment, a slanted ablation track along Sample 5.

The Aerotech stage can be programmed using G-Code to follow a precise ablation program, but samples must be held uniformly and the program initiated from a set point so that comparisons between runs are as accurate and quantitative as possible. This is especially true if the sample has variable height and the Rayleigh length is short, as was the case here. An active feedback mechanism may be important to optimize signal strength while also ensuring complete sample ablation.

An important step in future work would be to operate the laser in single pulse mode. This would provide a better understanding of the extent of the heat-affected zone. The laser operated at 1 kHz in this study, leading to debris in and around the ablation trench. Operation in single pulse mode would better demonstrate the ability of femtosecond lasers to ablate material with minimal debris and heat-affected zone, at the cost of lower signal strength.

A final area for development is the variability of laser spot size. By changing the lens, the

spot size has been reduced to the nanometer scale (Kuznetsov et al., 2015). However, a vacuum system would be required due to UV absorption by air molecules. At the other end of the scale, macroscopic spot sizes are also possible. Given a laser of sufficient power, this could bridge the gap between nanoscale and macroscale (Hosemann, 2018). Techniques such as SIMS and TIMS excel at nanoscale. Techniques such as neutron tomography provide powerful nondestructive 3-dimensional capability at the macro level. LAMS holds potential to bridge the gap.

The Thermo-X mass spectrometer performed adequately but better results should be possible with retuning and careful calibration. The data showed reasonable precision for the purpose of this study. The ability of mass spectrometry to provide both isotopics and concentrations (given matrix-matched standards) makes it especially suitable for nuclear fuel and nuclear forensics analyses. The next section discusses this in more detail. The ultimate goal of using a femtosecond laser to ablate spent fuel and analyze the fission products as a precise function of position remains for future research. The high radiation fields around spent fuel would require careful engineering of the laser and ablation cell, but such a system is conceivable for both PWR and TRISO fuel. Another advantage of LAMS is the fact that disposable cells can contain the contamination leaving the laser system, leaving the stage clean and easily accessible after the active samples have been removed.

Expected decay products in fresh fuel as investigated

The samples showed activity on the order of microCuries and contain the daughter products of ^{238}U and ^{235}U decay. Depending on when the isotopes were last separated, the daughter concentrations may not reach detection thresholds. A separation date in the year 1980 places the detection of ^{234}Th from the decay of ^{238}U and ^{231}Th from the decay of ^{235}U below the detection limit of the mass spectrometer in the configuration at the time (800 ppb for tungsten), even neglecting the decay of the parent (i.e., assuming a fixed source term) and the decay of the daughter into granddaughter nuclides. The signal from daughter products could also be confounded by pre-existing quantities of the same isotopes as impurities from the separation process. Further, ^{222}Rn occurs in the decay chain of ^{238}U. The release of radon gas in mineral samples is typically limited to the region within micrometers of the surface, unless fission tracks or grain boundaries provide an escape path (Nielson & Sandquist, 2011). The ablation craters are on the order of a few micrometers, so the gas could have escaped, and the predicted ^{222}Rn concentration is below the estimated detection limit because of the long time (thousands of years) necessary for sufficient ingrowth from the alpha decay of ^{226}Ra ($t_{\frac{1}{2}} = 1,599$ y). As a result, radon and its daughter products are not expected in detectable amounts unless extant as impurities from incomplete separation. Considering only ^{238}U because it is present in highest concentration and disregarding ^{234}Th and ^{234}Pa because of their short half-lives (24.10 d for ^{234}Th), then ^{234}U would be the best candidate for isotopic comparison to ^{238}U. Its concentration is almost certainly below detection limits,

but it would be the most viable isotope to determine a date of separation for the parent material. Because of its low natural abundance, ^{234}U was not considered during initial data collection. ^{234}U was measured in the standard CRM 125-A, but Th was not measured.

System parameters such as helium flow rate, RF power, and torch position influence the sensitivity. This system had a maximum helium flow rate of 624 mL per minute, which is lower than the industry standard of $\sim$ 1 liter per minute. There was no clear way to increase the flow rate beyond this threshold, though several colleagues attempted to increase it. Future work may include finding a way to increase this rate. The RF power was high to improve sensitivity at the cost of increasing oxides. Oxides are a known issue with ICP-MS because the ionization process occurs at atmospheric pressure. Oxide content for $\frac{\text{CeO}}{\text{Ce}}$ remained below 5% and did not influence the outcomes in this work (demonstrated, for example, by acceptable isotope ratios). The $\frac{\text{CeO}}{\text{Ce}}$ ratio is used as an indicator for all other elements because the oxygen affinity of Ce is higher than most other elements. Thus the ratio of CeO to Ce is used as a proxy for the presence of oxygen as oxides in other elements. Stated differently, if oxygen is present, the CeO to Ce ratio is assessed to be the highest. If CeO to Ce ratio is less than a given acceptable value (usually a few percent), then all other oxide to element ratios are assumed to be no higher. The ease of use, broad applicability, spot size range bridging the nanoscale and macroscopic regimes, and potential for use in a high-radiation environment make this system worthy of continued development.

5.1 CRM 125-A

The investigation of LAMS capabilities on various standards, tungsten metal, TRISO surrogates, and PWR fuel pellet surrogates provided a basic understanding of femtosecond laser capabilities. The Spectra-Physics Ti:Sapphire laser obtained $\pm$1 a% accuracy with uranium and tungsten isotope ratios and calibration curves with $R^2 > 0.99$. Different calibration approaches were tested, but acceptably accurate concentration results on standards were developed only with difficulty. This hampered the final analysis and led to the consideration of further testing using high-performance mass spectrometry. Semiquantitative concentrations, isotope ratios, and EDX comparisons served to corroborate the LANL neutron tomography results Tremsin et al. (2013) and surrogate TRISO particle data.

Tungsten Wafer

Figure 5.2 shows the tungsten wafer with ablation track. The wafer provided one of two tungsten calibration points, with CRM 125-A providing the second point. This served as an alternative to the NIST glass calibration curve specifically for tungsten.

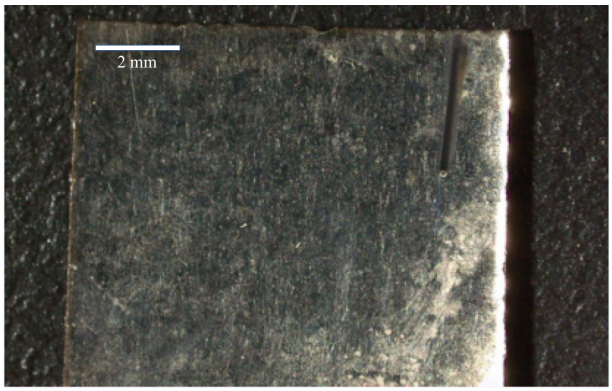

Figure 5.2: An unprovenanced tungsten wafer used to develop the tungsten calibration. An ablation track is visible in the upper right of the image.

In combination with CRM 125-A, the wafer provided a two-point calibration for tungsten. This served as a workaround given the difficulties in developing a curve for tungsten using NIST glass. A NIST glass curve was eventually developed using a simplified background subtraction approach. Tungsten was particularly important because impuritites were found in the actual fuel pellet as well (see Section 5.3).

5.2 NIST Glass challenges and opportunities

Developing a calibration curve for the NIST glasses proved challenging for a variety of reasons. Systems like laser ablation mass spectrometers are composed of multiple devices that must work in concert reliably. However, due to the system complexity small errors and unforseen software or hardware failures can lead to work stoppage. This led to multiple signifcant delays during this research and highlights the importance of strong debugging and troubleshooting procedures, espcially if deployed in the field.

One such instance was the loss of mass spectrometry signal during ablation despite no known change to any settings between runs. Even though ablation was clearly occurring, the counts-per-second did not change from background level. This delayed work for several weeks while various colleagues tried to identify the issue. Eventually, by accident, the issue was discovered. The helium gas flow was shutting off automatically as the runs began. Once this was identified, the procedure was to manually ramp the helium flow back to operating level before collecting spectra. The same procedure was used throughout the rest of the analyses because the root cause was not identified. Another issue was finding data that produced reasonable calibrations with sufficiently high R^2 values of at least 0.99. Many NIST glass samples were analyzed, but many errors early on created uncertainty. The fact that NIST 614 was at the detection limit for several elements, including tungsten, further complicated

the initial development because the system had be tuned to optimize the signal. The last factor was the calibration method itself. Several were tried, including the Relative Sensitivity Factor method of Dr. David Weisz (Section 7.3). This approach was sometimes effective but inconsistent. The approach given by Dr. Josh Wimpenny (Section 7.2) was more rigorous but more labor-intensive and also gave inconsistent results. After considering several different data treatment approches it was found that the simplest way (background subtraction calibrations) yielded the most accurate results and were used for the final development of the NIST glass calibrations.

5.3 LANL Surrogate Fuel Samples

The PWR fuel elements provided by LANL were treated as a blind test with no further information in order to demonstrate how LAMS can be used to characerize and verify fresh fuel elements. The surrogate PWR fuel pellets from LANL gave mass-over-charge ratios indicative of unexpected elements such as W, Zr, and Ce. These elements could be correlated with the manufacturing data to determine if the observed elements were dopants or surface contamination. The manufacturing process for the LANL samples involved processing in the inert atmosphere of a glovebox. Contamination from previous work in the globebox could have fallen on the outer surfaces of the samples. Thus it is interesting to note the possibility of determining elements and isotopes present in the facility in the past based on the surface contamination detectable by LAMS.

While analysis of surface contamination in this instance is valuable in its own right, in other applications it may not be valuable. One technique to overcome surface contamination when it is not part of the analysis is to take multiple runs over the same ablation path to ablate away any surface contamination and then analyze the bottom of the trench as a fresh surface. Some caution must be used with this approach. Research shows that trenches which are deep relative to the beam focal length can contribute to isotope fractionation (Mank & Mason, 1999). The system used on the LANL samples generated a 40 μm deep trench, which is negligible compared to the 1.6 mm focal length. Therefore the practice of ablating surface material and then conducting a second run over the ablated trench is viable for this configuration. The multi-pass method can be a problem if the sample is heterogeneous in terms of ablation efficiency. For example, the outer layers of SiC and pyrolytic carbon ablated much more readily than the Zr core or the depleted UO_2 surrogate fuel at equivalent power and translation speed.

The surrogate PWR fuel pellets from LANL showed various concentrations of unexpected constituents such as zirconium, cerium, and neodymium. These anomalies could be correlated with the manufacturing specifications to determine if the observed elements were dopants or surface contamination. Sample custody was fastidious and surface contamina-

tion while at LLNL was unlikely. The presence of tungsten in certain samples, especially Sample 2, was clear given the high counts, reaching millions of counts per second in certain sections. While all samples showed at least low levels of tungsten, Samples 2 and 3 had much higher counts than the others. Sample 2 showed an increase in tungsten signal near, but not at, one end. This more closely matched the description of sample preparation in a study by (Tremsin et al., 2013), which states that small pieces of tungsten may have been added to the samples. This particular spike could be an example of the ablation zone reaching a small piece of tungsten. Sample 3 shows the highest counts at one end and could be an example of tungsten diffusion from the sample holder, itself also made of tungsten. Why the other samples did not also exhibit this signal is unknown. It may be that this specific sample was sintered at a higher temperature, allowing more tungsten diffusion.

5.4 TRISO surrogate fuel particles

The surrogate TRISO particles exhibited notably different behavior from the metals, in that they ablated much more readily at comparable laser power. The craters in TRISO were deeper than those in metal, making depth control more of an issue, though this could be ameliorated by using lower laser power settings. Silver appears to escape TRISO as a function of temperature and neutron fluence, as (B. G. Kim et al., 2015) found. The escape of fission products from TRISO increases exponentially with temperature and is not limited to Ag (Lillo et al., 2017). Xe and Kr are used to monitor PWR cores for pin failure. A square-root rise in fission gas release implies fuel cladding failure (Vanderheyden et al., 2021).

For several decades, it has been known that silver can escape silicon carbide. The precise mechanism remains unclear, but the search has narrowed over the years. Specifically, (B. G. Kim et al., 2015) found that high temperature and high neutron fluence lead to increased Ag release from SiC. The related question was why other fission products didn't also show a higher release fraction given high temperature and high neutron fluence. The answer, in part, is that they do, but Ag appears to be more prone to do so. The reasons may be due to some as-yet unknown electrical property of silver. Recent research with room-temperature semiconductors has shown that unexpected electronic behavior can arise from specific geometries between carbon atoms. This is not to say that a similar effect occurrs with silver and SiC, only that some unexpected electronic or mechanical property may explain the observed behavior.

The most stressing case is the escape of Ag from intact TRISO with no Pd present. MacLean proposed that this is due to micro/nanocracking that hasn't been detected or fully appreciated yet. The state-of-the art in microscopy has been sub-Angstrom for over a decade, so this seems unlikely but cannot be ruled out. (B. G. Kim et al., 2015) posited that high temperature and high neutron fluence create conditions where Ag can escape more read-

ily. Nanocracking (MacLean, 2004) may well occur under these extreme conditions, only to be annealed out as the material cools. Future research will address why silver is able to escape. Recent work with the superconducting properties of graphene by Cao and Khalaf may offer an interesting new approach to thinking about Ag escape through SiC (Cao et al., 2018); (Khalaf et al., 2019); (Park et al., 2021), and (Tarnopolsky et al., 2019). Some unique combination of material properties must provide reduced resistance specific to Ag while passing through the SiC barrier. A certain angle of rotation, roughly 1.1°, between sheets of graphene provides radically different electronic behavior compared to most any other angle. While the concept of superconductivity itself almost certainly has no bearing on Ag transport in SiC, the idea that there is an as-yet undiscovered electronic or chemical property between Ag and SiC may yield insight into Ag transport.

The goals of this effort were to determine if femtosecond laser ablation mass spectrometry offered an optimized solution for standoff fuel analysis by characterizing the spatial and mass precision of the LAMS system. If sufficiently accurate, a secondary objective was to confirm the Neutron Tomography study done at LANCSE (Tremsin et al., 2013). A tertiary goal was to determine if LAMS would be effective at finding fission particles through the thickness of TRISO fuel. This section addresses each aspect in turn and concludes with the potential for future research.

Chapter 6

Summary

The purpose of this effort was to characterize a laser ablation mass spectrometry system and determine the potential for standoff LAMS to determine the elemental and isotopic composition of spent nuclear fuel and possibly to conduct nuclear forensics. (Puranen et al., 2017) conducted similar studies looking at Be in spent fuel to better understand corrosion. The role of various dopants in nuclear fuel has been studied intensively since the Fukushima accident. The work of (Riglet-Martial et al., 2014) has shown that chromium, for example, may stabilize nuclear fuel against corrosion. (Bischoff et al., 2018) found improved wear resistance and corrosion resistance with the coating of Cr on zirconium cladding and on UO_2 fuel. These studies are two of many examples that would be excellent test cases for a refined LAMS system.

The ability to ablate into spent PWR and TRISO fuel to identify isotopic constituents by position from the outer surface to the center of a fuel element would be a powerful capability. Additionally, the use of femtosecond lasers for micromachining and additive manufacturing is undergoing continued growth (McCulloch et al., 2020). The use of chromium in Accident Tolerant Fuels has been shown to improve the corrosion resistance of Zr Femtosecond and faster lasers bring the potential for clean, efficient ablation, permitting analysis of spent fuel earlier in the post-power phase. Such early analysis could provide higher fidelity understanding of the location and distribution of fission products as a function of radius from the central axis out through the cladding. This would provide rapid insight into the condition of fuel remaining in the reactor compared to current practice. This early analysis could optimize fuel performance in the core. In addition, the ability of femtosecond lasers to bridge the nanoscale and mesoscale in material testing provides important areas of further research (Hosemann, 2018).

Preliminary work was done to show the feasibility of laser ablation on surrogate TRISO. With a quantitative reference system, accurate determination of trace and isotopic particle content by area ablation or across polished hemispheres is possible. The advantages of laser ablation ICP-MS could help determine the migration of Ag through SiC. The mass spectrom-

eter has better limits of detection than the neutron tomography method used in the parallel work and serves as confirmation of the tomography results. Analysis of surrogate fuel pellets of depleted U provided by Los Alamos National Laboratory gave an opportunity to test the system against a facsimile of nuclear fuel. The ability to determine isotope ratios and concentrations of a variety of elements showed that this LAMS configuration has applicability in analyzing spent nuclear fuels. The detection limits with this system were approximately 1 ppm based on analysis of counts-per-second and signal-to-noise. Using a more intense beam spot could increase the signal to noise and improve detection limits. Also, the use of a more precise and quantitative sample holder may also improve the detection limit by optimizing sample position and thus the beam energy. In this effort, the beam focus was very sensitive to vertical changes, so subtle misalignment could lead to a decrease in ablation efficiency. Precise sample alignment would optimize the beam focus across the entire sample length. Optical and SEM images from these samples show clean ablation in some instances with heavy ablation debris in others. The heavy debris is likely a consequence of using excessive laser power, in accordance with the findings of (Shaheen et al., 2013).

These initial investigations show that LAMS can provide a faster and more efficient means to analyze samples such as spent fuel and forensic material than other commonly used techniques such as SIMS and EDS. LAMS could play an important role in quickly analyzing TRISO particles to determine the location of silver as a function of depth into the particle. The advantage of LAMS over EDS was clearly demonstrated, for example, in Figure 4.11 compared to Figure 4.7 and Table 4.14. The EDX spectrum of Sample 3 showed tungsten barely above background, whereas the LAMS system measured tungsten at almost 1%.

The data also support a more nuanced interpretation of the nuetron tomography data. Diffusion of tungsten into the LANL samples from the tungsten end plates that held the samples in place during sintering was one explanation for the presence of tungsten. However, the discovery of strong, isolated tungsten signals within the samples suggests intentional doping of tungsten as a virtually pure metal. Samples 1, 2, and 5 all demonstrate tungsten peaks at some distance from the end. The possibility of extended diffusion cannot be ruled out, but the presence of almost pure tungsten metal as a dopant is further supported by the high peak concentrations found in Samples 2 and 3 of approximately 1% (see Table 4.15, page 71.

Future Work

A potentially valuable step in this research would be to investigate single pulses to carefully map out the ablation thresholds of various materials to this system. After that, determining the optimum laser energy for finding the detection limits of the mass spectrometer by element would help to optimize routine analyses and provide guidelines for analysis of unknown samples.

Future projects may include developing a precise sample holder, fabricating a scaled demonstration chamber for high radiation samples and either a robotic arm or multi-axis sample holder that allows for volumetric ablation of highly active samples. Other potential applications could include elemental and isotopic analysis in dangerous environments. The comparatively small size and potential to make the system robust could allow deployment on board vehicles, ships, and aircraft. The power, vacuum, and gas flow requirements limit portability to vehicles, but the potential for portable high-fidelity analysis in the field offers a strong incentive to continue research.

The possibility of passing an intense laser pulse past the tip of an AFM needle to pull electrons off in a precise fashion may also be a useful path. The femtosecond pulse could also be used as a sharp impulse to 'ring' structures at various levels, from mesoscopic samples of metals with clean crystal lattices down to microscopic grains. The phonon excitations (and possibly other channels such as surface plasmons) could potentially be measured to gain an understanding of the dimensions and character of a given crystal or structure. This follows the work of (Feng, 2022) but would be applied on the microscopic scale. In terms of pulse duration, ultrafast lasers are now available in the attosecond regime (Teng et al., 2018). Faster lasers in combination with high performance mass spectrometers will almost certainly lead to new capabilities for nuclear applications.

References

Alvarede, F., & Beard, B. (2004). Analytical methods for non-traditional isotopes. *Reviews in Mineralogy and Geochemistry*, *55*, 113-152.

Bavio, M., Treinen, K., & Lindvall, R. (2019, February). IAEA Residential Assignment. *LLNL-TR-768545*.

Becher, P. F., & Funkenbusch, E. F. (1990, 11). Ternary ceramic alloys of zr-ce-hf oxides.

Bischoff, J., Delafoy, C., Vauglin, C., Barberis, P., Roubeyrie, C., Perche, D., ... Nimishakavi, K. (2018, January). Areva np's enhanced accident-tolerant fuel developments: Focus on cr-coated m5 cladding. , *50*, 223-228.

Cancino, F., Navarro-Solis, D., López-Honorato, E., Rabone, J., Walker, R., & Salomon, R. (2018, October). Grain boundary complexions in silicon carbide. *Journal of the American Ceramic Society*, *101*, 1009-1013.

Cancino-Trejo, F., Navarro-Solis, D., López-Honorato, E., Rabone, J., Walker, R., & Salomon, R. (2018, October). Grain boundary complexions in silicon carbide. *Journal of the American Ceramic Society*, *101*, 1009-1013.

Cao, Y., Fatemi, V., Demir, A., Fang, S., Tomarken, S., Luo, J., ... Jarillo-Herrero, P. (2018, April). Correlated insulator behaviour at half-filling in magic-angle graphene superlattices. *Nature*, *80*(84).

Carter, L., Seelig, J., Brockman, J., Robertson, J., & Loyalka, S. (2018, January). Icp-ms measurement of silver diffusion coefficient in graphite ig-110 between 1048k and 1284k. *Journal of Nuclear Materials*, *498*, 44-49.

Chow, J. C., Adams, F., Roubstov, D., Singh, R., & Zeller, M. (2012). Nuclear data and the effect of gadolinium in the moderator. *AECL NUCLEAR REVIEW*, *1*(1).

Clark, R., Conroy, M., Lach, T., Buck, E., Pellegrini, K., McNamara, B., & Schwantes, J. (2020). Distribution of metallic fission product particles in the cladding liner of spent nuclear fuel. *npj Materials Degradation*, *4*(4).

Dawson, P. (1976). *Quadrupole mass spectrometry and it applications*. Elsevier.

Dempster, A. J. (1918, April). A new method of positive ray analysis. *The London, Edinburgh, and Dublin Philosophical Magazine and Journal of Science*, *11*(316). doi: 10.1080/14786441208636004

Dereniak, E., & Dereniak, T. (2008). *Geometrical and trigonometric optics*. Cambridge University Press. Retrieved from `https://books.google.com/books?id=FKguseVDPFoC`

Drude, P. (1900, January). Zur Elektronentheorie der Metalle. *Annalen der Physik*, *306*(3), 566-613.

Einstein, A. (1905). On the Movement of Small Particles Suspended in Stationary Liquids Required by the Molecular-Kinetic Theory of Heat. *Annalen der Physik*, *17*(4), 549.

EngineeringToolbox. (2020). *Engineering Toolbox.* Retrieved from `EngineeringToolBox,(2003).AbsoluteorDynamicViscosityOnlineConverter .[online]Availableat:https://www.engineeringtoolbox.com/dynamic-viscosity -d_571.html[Accessed23January2020].`

Evans, D., & Müller, W. (2018). Automated extraction of a five-year la-icp-ms trace element data set of ten common glass and carbonate reference materials: Long-term data quality, optimisation and laser cell homogeneity. *Geostandards and Geoanalytical Research*, *42*(2), 159-188. doi: 10.1111/ggr.12204

Feng, G. H. H. Q. J., T.; Chen. (2022). Femtosecond-laser-ablation dynamics in silicon revealed by transient reflectivity change. *Micromachines*, *13*(14).

Friedland, E., Berg, N., Malherbe, J., Hancke, J., Barry, J., Wendler, E., & Wesch, W. (2011, 03). Investigation of silver and iodine transport through silicon carbide layers prepared for nuclear fuel element cladding. *Journal of Nuclear Materials - J NUCL MATER*, *410*, 24-31. doi: 10.1016/j.jnucmat.2010.12.243

Gaboardi, M., & Humayun, M. (2009, 08). Elemental fractionation during la-icp-ms analysis of silicate glasses: Implications for matrix-independent standardization. *Journal of Analytical Atomic Spectrometry - J ANAL ATOM SPECTROM*, *24*. doi: 10.1039/b900876d

Gentile, M., Xiao, P., & Abram, T. (2015, March). Palladium interaction with sic. *Journal of Nuclear Materials*, *462*, 100-107.

Gerczak, T., Leng, B., Sridharan, K., Hunter, J., Giordani, A., & Allen, T. (2015, March). Observations of ag diffusion in sic. *Journal of Nuclear Materials*, *461*, 314-324.

Gray, A. (1985). Solid sample introduction by laser ablation for inductively coupled plasma source mass spectrometry. *Analyst*, *110*, 551-556.

Greenfield, S., Jones, I., & Berry, C. (1964).
Analyst, *48*(713).

Gurdal, G., & Kondev, F. (2012). COMPILATION 110Zr, 110Nb, 110Mo, 110Tc, 110Ru, 110Rh, 110Pd, 110Ag, 110Cd, 110In, 110Sn, 110Sb, 110Te, 110I, 110Xe; compiled evaluated nuclear structure data. *Nuclear Data Sheets*, *113*(1315).

Hales, J. D., Williamson, R. L., Novascone, S. R., Perez, D. M., Spencer, B. W., & Pastore, G. (2013, November). Multidimensional multiphysics simulation of TRISO particle fuel. *Journal of Nuclear Materials*, *443*(1), 531-543. doi: 10.1016/j.jnucmat.2013.07.070

Harp, J., Demkowicz, P., Winston, P., & Sterbentz, J. (2014, October). An analysis of nuclear fuel burnup in the agr-1 triso fuel experiment using gamma spectrometry, mass spectrometry, and computational simulation techniques. *INL/JOU-13-30458 PREPRINT*.

Hickman, R., Broadway, J., Trent, D., & Dziubanek, A. (2014). Hot hydrogen testing of tungsten-uranium dioxide (w-uo2) cermet fuel materials for nuclear thermal propulsion.

Hoffmann, E., & Stroobant, V. (2007). *Mass spectrometry: Principles and applications, 3^{rd} edition*. San Francisco, CA: John Wiley and Sons, Ltd.

Hosemann, P. (2018, January). Small-scale mechanical testing on nuclear materials: Bridging the experimental length-scale gap. *Scripta Materialia*, *143*.

Hosemann, P. (2022, January). Personal communication.

Hosemann, P., Martos, J., Frazer, D., Vasudevamurthy, G., Byun, T., J., H., ... Okuniewski, M. (2013). Mechanical characteristics of sic coating layer in triso fuel particles. *Journal of Nuclear Materials*, *442*, 133-142.

Houk, R., Fassel, V., Flesch, G., & Svec, H. (1980).
Anal. Chem.(52), 2283 - 2289.

IAEA. (2010, March). High temperature gas cooled reactor fuels and materials. *IAEA TECDOC*, *1645*.

Janney, D. (2017, August). Metallic fuels handbook, part 1. (INL/EXT-15-36520 Revision 2 Part 1).

Jiang, Y., Chen, Z., Han, Y., Deb, P., Gao, H., Xie, S., ... Muller, D. A. (2018). Electron ptychography of 2d materials to deep sub-ångström resolution. *Nature (London)*, *559*(7714), 343-349.

Jochum, K., Nohl, U., Herwig, K., Lammel, E., Stoll, B., & Hofmann, A. (2007, 05). Georem: A new geochemical database for reference materials and isotopic standards. *Geostandards and Geoanalytical Research*, *29*, 333 - 338. doi: 10.1111/j.1751-908X.2005.tb00904.x

Khalaf, E., Kruchkov, A. J., Tarnopolsky, G., & Vishwanath, A. (2019, Aug). Magic angle hierarchy in twisted graphene multilayers. *Physical Review B*, *100*(8). Retrieved from `http://dx.doi.org/10.1103/PhysRevB.100.085109` doi: 10.1103/physrevb.100.085109

Kim, B. G., Yeo, S., Young, W., & Moon, S. (2015). Comparison of diffusion coefficients and activation energies for ag diffusion in silicon carbide. *Nucl Eng Technol*, *47*, 608-616.

Kim, J., Jeon, Y., Park, S., Ha, Y., & Song, K. (2015). Analysis of high burnup pressurized water reactor fuel using uranium, plutonium, neodymium, and cesium isotope correlations with burnup. *Nuclear Engineering Technology*, *47*, 924-933.

Kraiem, M., Essex, R., Mathew, K., Orlowicz, G., & Soriano, M. (2013, May). Re-certification of the crm 125-a uo_2 fuel pellet standard for uranium isotopic composition. *International Journal of Mass Spectrometry*, *352*, 37-43.

Krane, K. (1988). Introductory nuclear physics. *John Wiley and Sons*.

Kumar, S., Chen, J., & Kondev, F. (2016). . *NDS*, *1*.

Kuznetsov, I., Filevich, J., Dong, F., Woolston, M., Chao, W., Anderson, E., ... Menoni, C. (2015, April). Three-dimensional nanoscale molecular imaging by extreme ultraviolet laser ablation mass spectrometry. , *6*.

Lawrence, E. O., & Livingston, M. S. (1932, Apr). The production of high speed light ions without the use of high voltages. *Phys. Rev.*, *40*, 19–35. Retrieved from `https://link.aps.org/doi/10.1103/PhysRev.40.19` doi: 10.1103/PhysRev.40.19

Lee, R. (2002, March). Study of the effect of integral burnable absorbers for PWR burnup credit. *ORNL/TM-2000-321*.

Le Harzic, R., Huot, N., Audouard, E., Jonin, C., Laporte, P., Valette, S., ... Fortunier, R. (2002). Comparison of heat-affected zones due to nanosecond and femtosecond laser pulses using transmission electronic microscopy. *Applied Physics Letters*, *80*(21), 3886-3888. doi: 10.1063/1.1481195

Lewis, L. (2018). The origin of agglomerates and their role in forming near-surface glassy fallout. *Doctoral Dissertation, UC Berkeley*.

Lillo, T., van Rooyen, I., & Aguiar, J. (2017, December). Silicon carbide grain boundary distributions, irradiation conditions, and silver retention in irradiated agr-1 triso fuel particles.

Liu, W., Sun, M., Guo, Y., Jiao, Z., Wu, R., & Pan, X. (2019). Ablation characteristics of aluminum alloy and stainless steel induced by picosecond laser pulses. In J. Shao, T. Jitsuno, & W. Rudolph (Eds.), *Pacific rim laser damage 2019: Optical materials for*

high-power lasers (Vol. 11063, pp. 319 – 325). SPIE. Retrieved from `https://doi.org/10.1117/12.2539907` doi: 10.1117/12.2539907

López-Honorato, E., Fu, K., Meadows, P., Tan, J., & Xiao, P. (2010). Effect of microstructure on the resilience of silicon carbide to palladium attack. *Journal of the American Ceramic Society*, *93*(12), 4135–4141.

López-Honorato, E., Yang, D., Tan, J., Meadows, P., & Xiao, P. (2010, October). Silver diffusion in coated fuel particles. *Journal of the American Ceramic Society*, *93*(10), 3076-3079.

López-Honorato, E., Zhang, H., Yang, D., & Xiao, P. (2011, September). Silver diffusion in silicon carbide coatings. *J. Am. Ceram. Soc.*, *94*(9), 3064-3071.

Losko, A., Vogel, S., Tremsin, A., & Hosemann, P. (2014, February). *Energy dispersive neutron imaging of nuclear fuel pellets.* `https://TMSPresentation2014`.

MacLean, H. (2004). Silver transport in cvd silicon carbide. *MIT PhD Thesis*.

Mank, A., & Mason, P. (1999). A critical assessment of laser ablation icp-ms as an analytical tool for depth analysis in silica-based glass samples. *J. Anal. At. Spectrom.*, *14*, 1143-1153. doi: 10.1039/A903304A

Marks, N. (2021, January). Personal communication.

Mattauch, J., & Herzog, R. (1934). Uber einen neuen massenspectrographen. *Z. Physik*, *89*(0), 786-7995.

Maxwell, J. (1865). A dynamical theory of the electric field. *Philosophical Transactions of the Royal Society of London*, *155*, 459-512.

May, T., & Wiedmayer, R. (1998, October). A table of polyatomic interferences. *Atomic Spectroscopy*, *19*(5).

McCulloch, Q., Gigax, J., & Hosemann, P. (2020). Femtosecond laser ablation for mesoscale specimen evaluation. *Journal of Materials*, *72*.

Meher, S., van Rooyen, I., & Jiang, C. (2019). Understanding of fission product transport in sic layer of triso fuels by nanoscale characterization and modeling. *Journal of Nuclear Materials*, *527*.

Miliszkiewicz, N., Walas, S., & Tobiasz, A. (2015). Current approaches to calibration of la-icp-ms analysis. *Journal of Analytical Atomic Spectroscopy*, *30*.

Montaser, A., McLean, J., & Huiying, L. (1998). An introduction to ICP spectrometries for elemental analysis. In *Inductively coupled plasma mass spectrometry.* New York: Wiley–VCH.

Morris, R., Petti, D., Powers, D., Boyack, B., & Rubin, M. (2004, July). Triso-coated particle fuel phenomenon identification and ranking tables (pirts) for fission product transport due to manufacturing, operations, and accidents: Main report (nureg/cr-6844, volume 1). *NUREG/CR-6844*, *1*.

Nakamura, J. (1998). *Thermal diffusivity of high burn-up uo_2 pellet irradiated at hbwr.*

Neethling, J., O'Connell, J., & Olivier, E. (2012, October). Palladium assisted silver transport in polycrystalline sic. *Nuclear Engineering and Design*, *251*, 230-234.

Nielson, K., & Sandquist, G. (2011, February). *Radon emanation from disposal of depleted uranium at clive, utah.* `http://ibilabs.com/pdf/Nielson_Sandquist2011.pdf`.

Nier, A. (1940). A mass spectrometer for routine isotopic abundance measurements. *The Review of Scientific Instruments*, *11*(212).

Nier, A. (1947, June). A mass spectrometer for isotope and gas analysis. *The Review of Scientific Instruments*, *18*.

Nowotny, H. (1970). Struktuchemie Einiger Verbindungen der Ubergangsmetalle mit den elementen C, Si, Ge, Sn. *Solid State Chemistry*, *2*(27).

Ohai, D. (2002). Technologies for manufacturing UO2 sintered pellets to fuel burnup extension. *Technical and economic limits to fuel burnup extension*, 193.

Park, J. M., Cao, Y., Watanabe, K., Taniguchi, T., & Jarillo-Herrero, P. (2021, February). Tunable strongly coupled superconductivity in magic-angle twisted trilayer graphene. *Nature*, *590*, 249-255.

Paschotta, R. (2008). Optical aberrations. *Encyclopedia of Laser Physics and Technology*, *First Edition*.

Patel, S. (2019, March). *Rapid advancements for fast reactors.*

Paul, W., & Steinwedel, H. (1953). Ein neues massenspektrometer ohne magnetfeld. *Zeitschrift für Naturforschung*, *8*(7), 448–450.

Pessoa, I., Antonioli, L., & Geraldes, M. (2021). Hidden archives of environmental change: Application of mass spectrometry methods in coral reef science. *Earth and Space Science Open Archive*, 1. Retrieved from `https://doi.org/10.1002/essoar.10505765.2` doi: 10.1002/essoar.10505765.2

Puranen, A., Tejland, P., Granfors, M., Schrire, D., Josefsson, B., & Bengtsson, B. (2017). Lithium and boron analysis by la-icp-ms results from a bowed pwr rod with contact. *EPJ Nuclear Science and Technology*, *3*(2).

Radford, K., & Pope, J. (1983). UO2 fuel pellet microstructure modification through impurity additions. *Journal of Nuclear Materials*, *116*(2), 305-313.

Riglet-Martial, C., Martin, P., Testemale, D., Sabathier-Devals, C., Carlot, G., Matheron, P., ... Largenton, R. (2014). Thermodynamics of chrmoium in uo_2 fuel: A solubility model. , *447*, 63-72.

Rolison, J., Treinen, K., McHugh, K., Gaffney, A., & Williams, R. (2017). Applications of the ^{226}ra - ^{230}th - ^{2234}u and ^{227}ac - ^{231}pa - ^{235}u radiochronometers to uranium certified reference materials. *J Radioanal Nucl Chem*, *314*(3), 2459-2467.

Rondinella, V., & Wiss, T. (2010, December). The high burn-up structure in nuclear fuel. *Materials Today*, *13*(12).

Saint-Gobain. (2019). *High purity tubing.*

Sawa, K., & Tanaka, T. (1995, October). A study of silver behavior in gas-turbine high temperature gas-cooled reactor. *JAERI*.

Scates, D., Hartwell, J., Drigert, M., & Walter, J. (2007). Preliminary results of an on-line multi-spectrometer fission product monitoring system to support advanced gas reactor fuel testing and qualification in the advanced test reactor at the idaho national laboratory. *INL/CON-07-12687 Preprint*, *7*(2), 43-55.

Schaltegger, U. A., Schmitt, M., & Horstwood. (2015). U–Th–Pb zircon geochronology by D–TIMS, SIMS, and laser ablation ICP–MS: Recipes, interpretation, and opportunities. *Chemical Geology*, *402*(7), 89-110.

Schlichting, H., & Gersten, K. (2017). *Boundary layer theory* (Ninth ed.). Berlin: Springer-Verlag.

Schnitzler, B., & Borowski, S. (2012, July). Small fast spectrum reactor designs suitable for direct nuclear thermal propulsion: 2012 joint propulsion conference..

Scott, R. H., Fassel, V. A., Kniseley, R. N., & Nixon, D. E. (1974). Inductively coupled plasma-optical emission analytical spectrometry. *Analytical Chemistry*, *46*(1), 75-80. doi: 10.1021/ac60337a031

Seibert, R., Terrani, K., Velazquez, D., Hunn, J., Baldwin, C., Montgomery, F., & Terry, J. (2018). Local atomic structure of pd and ag in the sic containment layer of triso fuel particles fissioned to 20% burn-up. *Journal of Nuclear Materials*, *500*, 316-326.

Sewall, W. (1921, January). Correlation and causation. *Journal of Agricultural Research*, *20*, 557-585.

Shaheen, M. E., Gagnon, J. E., & Fryer, B. J. (2013). Laser ablation of iron: A comparison between femtosecond and picosecond laser pulses. *Journal of Applied Physics*, *114*(8). Retrieved from `https://doi.org/10.1063/1.4819804` doi: 10.1063/1.4819804

Silfvast, W. T. (2004). *Laser fundamentals* (2nd ed.). Cambridge University Press. doi: 10.1017/CBO9780511616426

Smirnov, A., Bonarev, A., Sulaberidze, G., Borisevich, V., Kulikev, G., & Schmelev, A. (2015). Isotopically modified molybdenum: Production for application in nuclear energy. *Physics Procedia*, *72*, 126-131.

Smythe, W. R., & Mattauch, J. (1932, May). A new mass spectrometer. *Phys. Rev.*, *40*, 429–433. Retrieved from `https://link.aps.org/doi/10.1103/PhysRev.40.429` doi: 10.1103/PhysRev.40.429

Snead, L., Nozawa, T., Katoh, Y., Byun, T.-S., Kondo, S., & Petti, D. A. (2007). Handbook of sic properties for fuel performance modeling. *Journal of Nuclear Materials*, *371*(1), 329-377. (Nuclear Fuels and Structural Materials 1) doi: https://doi.org/10.1016/j.jnucmat.2007.05.016

Sommerfeld, A. (1928, January). Zur Elektronentheorie der Metalle auf Grund der Fermischen Statistik. *Zeitschrift fur Physik*, *47*(1-2), 1-32.

Sonwalkar, V., Mohanta, S., Pal, S., Rajagopalan, H., & Venkataramana, K. (2018). Identification of the contributors (Ag-110 m) for higher radiation field on primary heat transport system of Tarapur Atomic Power Station-3 and its impact on collective dose. *Radiation Protection and Environment*, *41*(2), 66-69. doi: 10.4103/rpe.RPE_5_18

Sonzogni, A. (2021). *Evaluated nuclear data file.* Retrieved from `https://www.nndc.bnl.gov/exfor/endf00.jsp/[Accessed04April2021].`

Spano, Simonetti, A., Corcoran, L., Smith, P., Lewis, S., & Burns, P. (2019). Comparative chemical and structural analyses of two uranium dioxide fuel pellets. *Journal of Nuclear Materials*, *518*.

Spectra-Physics. (1998).

Strickland, D., & Mourou, G. (1985). Compression of amplified chirped optical pulses. *Opt. Commun*, 219–221.

Tarnopolsky, G., Kruchkov, A. J., & Vishwanath, A. (2019, Mar). Origin of magic angles in twisted bilayer graphene. *Physical Review Letters*, *122*(10). Retrieved from `http://dx.doi.org/10.1103/PhysRevLett.122.106405` doi: 10.1103/physrevlett.122.106405

Teng, H., He, X.-K., Zhao, K., & Wei, Z.-Y. (2018, july). Attosecond laser station. *Chinese Physics B*, *27*(7). doi: 10.1088/1674-1056/27/7/074203

Thompson, Goulter, J., & Sieper, F. (1981, January). Laser ablation for the introduction of solid samples into an inductively coupled plasma for atomic-emission spectrometry. , *106*(32), 32-39.

Thompson, J. (1913, June). Rays of positive electricity. *Bakerian Lecture*.

Touran, N. (2009, September). *What is a fast reactor.*

Tremsin, A., Losko, A., Vogel, S., Byler, D., McClellan, K., Bourke, M., & Vallerga, J. (2017). Non-contact measurement of partial gas pressure and distribution of elemental composition using energy-resolved neutron imaging. *AIP Advances*, *7*(015315), 1-14.

Tremsin, A., Vogel, S., Mocko, M., Bourke, M., Yuan, V., Nelson, R., ... Feller, W. (2013, September). Non-destructive studies of fuel pellets by neutron resonance absorption radiography and thermal neutron radiography. *Journal of Nuclear Materials*, *440*, 633 - 646.

Turner, Mills, D., Schroder, E., Lapitajs, G., Jung, G., & Montaser, A. (1998). *Sample introduction for icp-ms*. New York: Wiley VCH.

Turner, & Montaser, A. (1998). Plasma Generation in ICPMS. In *Inductively coupled plasma mass spectrometry.* New York: Wiley–VCH.

Vanderheyden, G., Miller, S., & van Staden, M. (2021). Topical report: Triso-x pebble fuel qualification methodology revision 2. *2021-XE-NRC-012*.

van der Merwe, J. (2009, September). Evaluation of silver transport through sic during the german htr fuel program. *Journal of Nuclear Materials*, *395*, 99-111.

Vanhaecke, F., & Degryse, P. (2012). *Isotopic analysis: Fundamentals and applications using icp-ms*. Wiley-VCH Verlag GmbH Co. KGaA.

van Rooyen, I., Dunzik-Gougar, M., & van Rooyen, P. (2014). Silver transport mechanisms in triso coated particles: A critical review. *Nuclear Engineering and Design*, *271*, 180-188.

van Rooyen, I., Meher, S., & Rosales, J. (2018, October). Effect of neutron irradiation damage on fission product transport in the sic layer of triso fuel particles. *HTR Conference, Warsaw, Poland*, *Paper HTR 2018-3013*.

Vervoort, J., & Mueller, P. (2020, May). `https://serc.carleton.edu/research_education/geochemsheets/techniques/MCICPMS.html`.

Vogel, S. (2021). Beauty of pulsed neutrons - obtain neutron energy and wavelength by time-of-flight (unpublished draft).

Wigner, E. (1932). On the quantum correction for thermodynamic equilibrium. *Physical Review*, *40*(5), 745-759.

Wise, S., & Watters, R. (2012, April). Certificate of Analysis, Standard Reference Material® 610. *National Institute of Standards and Technology*, 1-4.

Wojciech, V., & Huneke, J. (1991, 07). Relative sensitivity factors in glow discharge mass spectrometry. , *46B*(2), 137-153.

Yang, G., Tazoe, H., & Yamada, M. (2018, May). Improved approach for routine monitoring of 129i activity and 129i/127i atom ratio in environmental samples using tmah extraction and icp-ms/ms. *Analytica Chimica Acta*, *1008*, 66-73.

Chapter 7

Appendix

7.1 Python Code

Written by Dr. Dajie Sun, Lawrence Berkeley National Laboratory

Input 1:
import numpy as np # numerical calculation model, very common library in python
import pandas as pd # a special matrix form calculation model, very popular library in python
import matplotlib.pyplot as plt # figure plot libary
import re # this library is used as to read the name of elements

# the below two libraries are used to create the folder import os
import shutil

Input 2:
def plot_for_each_file(data):
isotopes=data.columns.values[1:] # names of all isotopes
elements=np.asarray([re.split(r'(+)', x)[2] for x in isotopes]) # name of elements for each column
elements_set, idx=np.unique(elements, return_index=True) # elements set (remove the duplicated) while maintaining their order
elements_set=elements[np.sort(idx)] # find the elements set while keeping their order
for x in elements_set:
col_index=isotopes[np.where(elements==x)] # find out which columns correspond to element x
col_index=np.append('Time', col_index) # add the time columns to the data frame
element_to_plot=data.loc[:, col_index].astype('float') # change the data type to numerical values

```
#next, plot the whole data frame, with the first column(time) as x axis
element_to_plot.plot(x='Time', figsize=(10,8), fontsize=15)
plt.xlabel('Time', fontsize=15)
plt.ylabel('Unkonw y label', fontsize=15) # y label is User modified
plt.legend(fontsize=15)
plt.title(f'Element of x.", fontsize=20)
plt.tight_layout()
fig = plt.gcf()
fig.savefig(output_each_inputfile+'/'+f'Plot of Element of x.png')
plt.close() # don't display these plots in the jupyter notebook
#plt.show()
```

Input 3:

```
directory="./input_files/" # folder that contain all important files, ./ means current folder
filenames = os.listdir(directory)# search all the files in that folder, and put their names into a list

output_dir="./output_plots/"
if not os.path.exists(output_dir):# check whether the figures folder exists. If it does not exist, create it
os.makedirs(output_dir)
else:
shutil.rmtree(output_dir)# if it exists, delete it and recreate it
os.makedirs(output_dir)

files_info= pd.DataFrame(columns=['file_name', 'detail'])# define a dataframe to store file names and information
for i in range(len(filenames)):# read these files one by one
#print(filenames[i])
file_path=directory+filenames[i]
data=pd.read_csv(file_path)
first_row=data.loc[0].values
detail=first_row[ pd.isnull(first_row)][0]
#print(detail)
files_info=files_info.append('file_name': filenames[i], 'detail': detail, ignore_index=True)
data=data.drop([0, 1])# remove the first and second lines of the data because they are duplicated
output_each_inputfile=output_dir+filenames[i]
if not os.path.exists(output_each_inputfile):# check whether the figures folder exist, if they do NOT exist, create
os.makedirs(output_each_inputfile)
else:
```

shutil.rmtree(output_each_inputfile)# if it exists, delete it and recreate it
os.makedirs(output_each_inputfile)
plot_for_each_file(data)# plot the data for each file, save these plots as png image files. Do not display them here.
#data.head()
#files_info.head()

7.2 Wimpenny approach

1. Select a minimum in the background signal (taking the average of the background often leads to negative results for low concentrations)
2. Subtract the minimum background from each instance of the signal
3. Ratio each instance of the background subtracted signal to a major constituent of the matrix, such as Si for NIST glass
4. Take the Mean, Standard Deviation, Maximum, and Minimum of the ratioed data
5. Reject outliers (In Excel: IF(OR($A1>$B1, $A1<$B2), "Reject", $A1)
6. Take the Mean, Standard Deviation, Number of acceptable values n (In Excel: Count (A1:An), and Standard Error ($\frac{\text{Standard Deviation}}{\sqrt{\text{n}}}$ of the outlier-rejected data)
7. Compile data for all three NIST glasses
8. Take the abundance of the chosen bulk matrix constituent from the GeoREM website (usually given as an oxide)
9. Determine the fraction of the element from the oxide
10. Variation often occurs between the difference glasses. For SiO_2, the fraction of Si in NIST 610 is 69.7 versus 72.1 in NIST 612. Divide the percent of Si in each glass by the largest fraction of Si among any of the glasses and multiply by the fraction of Si (See Table 7.1).
11. Calculate the final isotopic values based on the internal standard correction.
12. Convert from a specific isotopic to elemental abundance by dividing result by the isotopic abundance. For example, if the value for ^{63}Cu is 100 ppm, divide by 0.6917 (the natural abundance of ^{63}Cu) to obtain the amount of total copper, neglecting fractionation and detector dead time effects.

NIST	%SiO_2	%Si	Internal Standard
610	69.7	32.58	0.96671
612	72.1	33.70	1
614	72.1	33.70	1

Table 7.1: Internal standard calculation for Si in NIST glass.

7.3 Relative Sensitivity Factor approach

1. Begin with samples containing known concentrations of a wide variety of elements. At present, the National Institute of Standards and Technology (NIST) Standard Reference Material (SRM) glasses (610, 612, and 614) are the accepted starting point. However, these standards are certified only for the sample as a whole. The certifications state explicitly that "Spatial heterogeneity exists within each wafer, which may adversely affect repeatability of microanalysis techniques."

2. Using the Certificate of Analysis issued by NIST for the 61X series, find the 'Preparation and Analysis' section. The percent oxides contained within the glass matrix are listed. Choose the oxide with the largest percent; here, SiO_2 at 72%.

3. Determine the fraction of Si in the SiO_2 by dividing the mass of Si by the total molecular mass:

$$\frac{\text{Si}}{\text{Si} + \text{O}_2} = \frac{28.085}{28.085 + 15.999 \cdot 2} = 0.4674$$

4. Use the fraction of Si in SiO_2 to find the percentage of Si in the NIST 610 glass: $0.72 \cdot 0.4674 = 33.65\%$. NIST glass is composed of 33.65% Si.

5. Of this Si matrix, it is important to know the abundance of the specific isotope ^{29}Si. To find it, multiply the total amount of Si present by the natural abundance of ^{29}Si, 0.04685:

$$0.3365 \ \cdot 0.04685 = 0.01577 = 1.577\% = 15,770 \text{ parts per million [ppm]}$$

   The NIST 610 matrix contains 15,770 ppm ^{29}Si.

6. Now build a table of concentrations from the Certificate of Analysis (Table 7.2) and from GeoRem (Jochum et al., 2007).

Table 7.2: Table of concentrations from NIST Certificate of Analysis [ppm] and the Preferred Values list in GeoRem (Jochum et al., 2007).

NIST	Ti	Fe	Ni	Cu	Rb	Sr	Cd	Ag	La	Ce	Pr	Nd	Sm	Eu	Gd	Tb	Dy	Er	Tm	Yb	Tl	Pb	Th	U
610	437	458	458.7	444	425.7	515.5	244	268	139	448	440	430	452	450	440	440	430	440	430	450	61.8	426	450	450
612	50.1	51	38.8	37.7	31.4	78.4	29.9	22	35.8	38.7	37.5	35.5	37	35	37	36	36	38	37	40	15.7	38.57	38	35
614	3.1	13.3	0.95	1.37	0.855	45.8	0.55	0.42	0.72	0.81	0.76	0.75	0.75	0.8	0.75	0.73	0.74	0.74	0.73	0.77	0.269	2.32	0.748	0.823
616	2.5	11	0.435	0.80	0.10	41.72	0.036	0.048	0.034	0.0292	0.015	0.0227	0.0164	0.0146	0.23	0.0145	0.0173	0.0157	0.0144	0.0171	0.0082	1.85	0.0252	0.0721

7. Again from the Certificate of Analysis, take the value of $\frac{^{235}U}{Total U}$.

   For NIST 610, this ratio is 0.002376. Then the ratio of $\frac{^{238}U}{Total U}$ is 1 - 0.002376 = 0.9976 (neglecting ^{234}U). This ratio is used as a correction factor for the listed U values in Table 7.3.

Table 7.3: Corrected U concentration.

NIST	U [ppm] · Correction Factor	Corrected U [ppm]
610	461.5 · 0.998	460.58
612	37.38 · 0.998	37.31
614	0.823 · 0.998	0.82

8. Table 7.4 gives the expected ratio for $\frac{^{238}U}{^{29}Si}$.

Table 7.4: $\frac{^{238}U}{^{29}Si}$ and $\frac{^{63}Cu}{^{29}Si}$ for calibration.

Quantity	610 [ppm]	612 [ppm]	614 [ppm]
^{238}U	460.58	37.31	0.82
^{29}Si	15770	15770	15770
$\frac{^{238}U}{^{29}Si}$	0.029	0.00173	0.00005
^{63}Cu	307±4	26.1±0.9	0.10±0.07
^{29}Si	15770	15770	15770
$\frac{^{63}Cu}{^{29}Si}$	0.01949	0.001654	6 x 10^{-5}

9. Plot $\frac{^{238}U}{^{29}Si}$ from Table 7.4 against the measured U concentration normalized to measured Si (Figure 7.1).

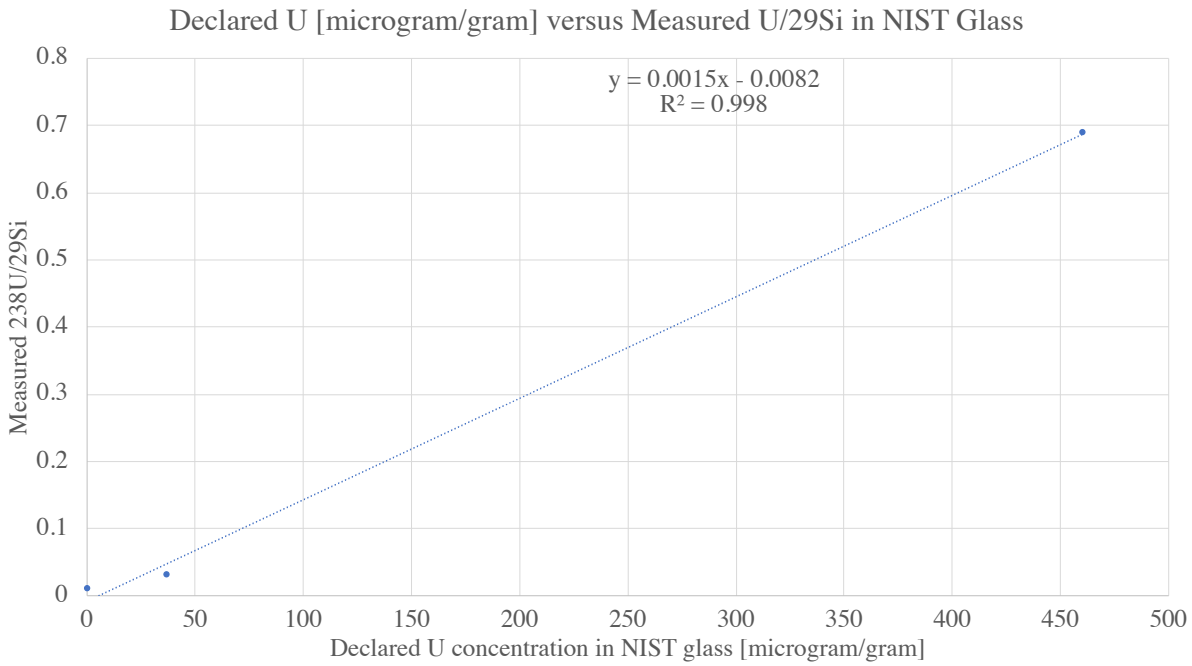

Figure 7.1: Declared U versus measured $\frac{U}{^{29}Si}$ in NIST Glass.

10. This can be used as a calibration curve between a measured ratio from mass spectrometric data to concentration in micrograms/gram (ppm).

11. A similar process can be followed to determine the concentration of other elements in NIST glasses, as in Figures 7.2, 7.4, and 7.6 below.

7.4 Select NIST Glass Calibration Curves

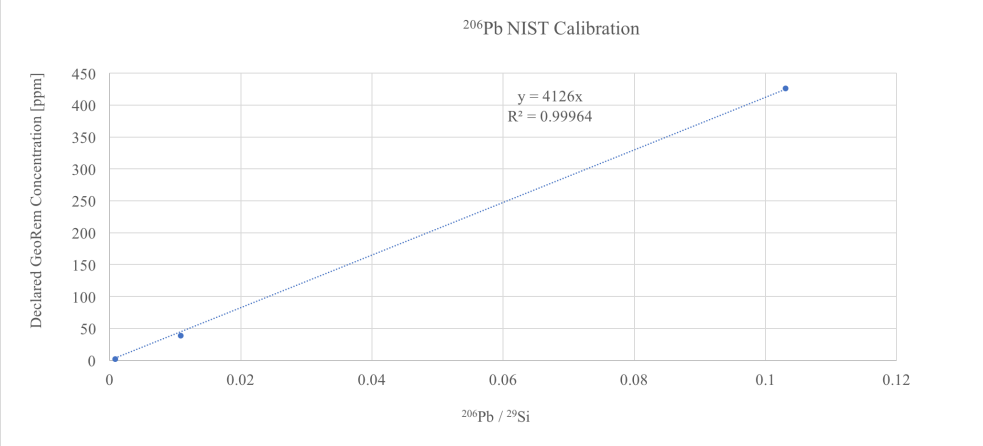

Figure 7.2: Calibration curve for ^{206}Pb.

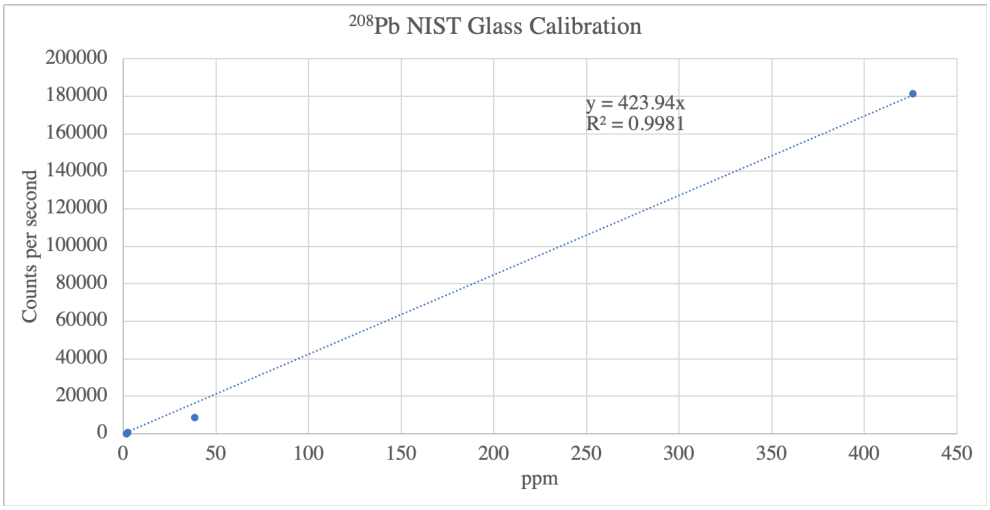

Figure 7.3: Calibration curve for ^{208}Pb.

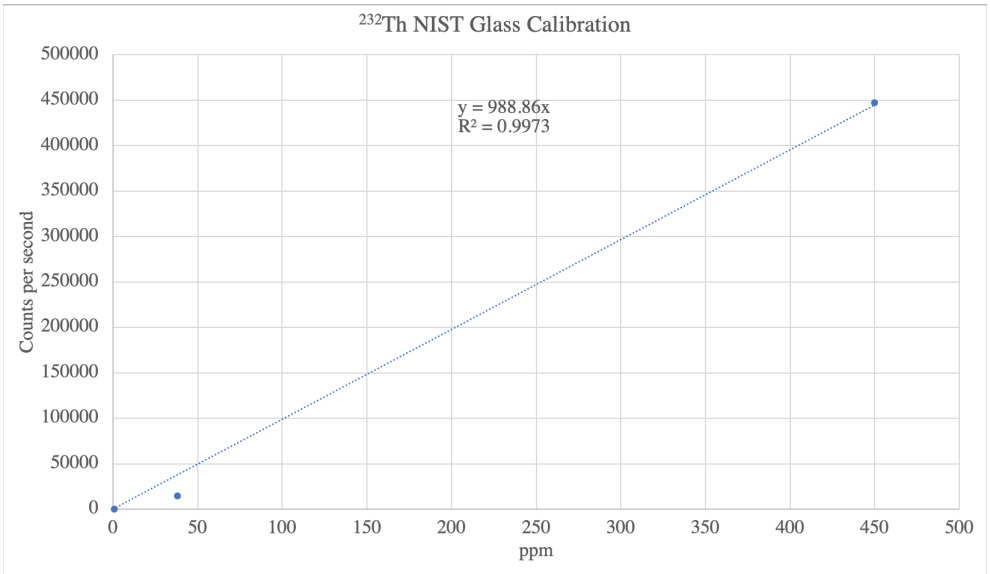

Figure 7.4: Calibration curve for ^{232}Th.

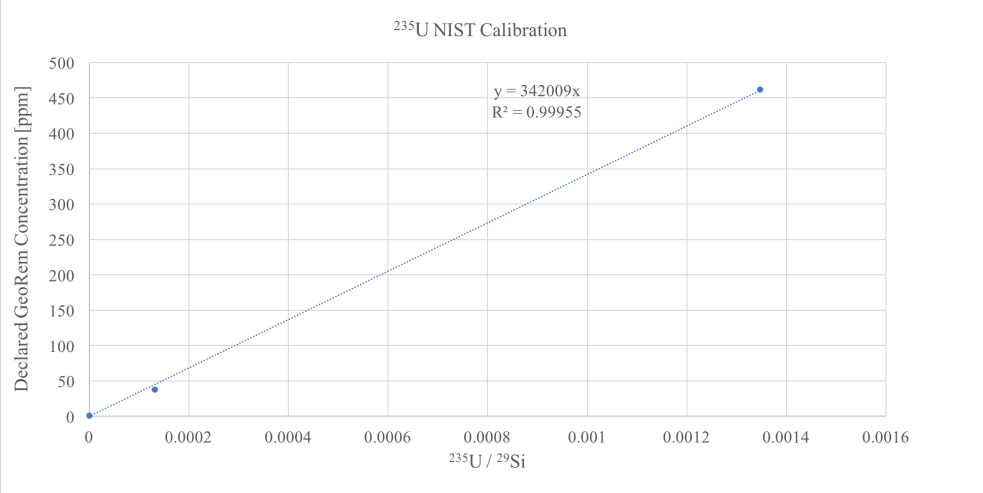

Figure 7.5: Calibration curve for ^{235}U.

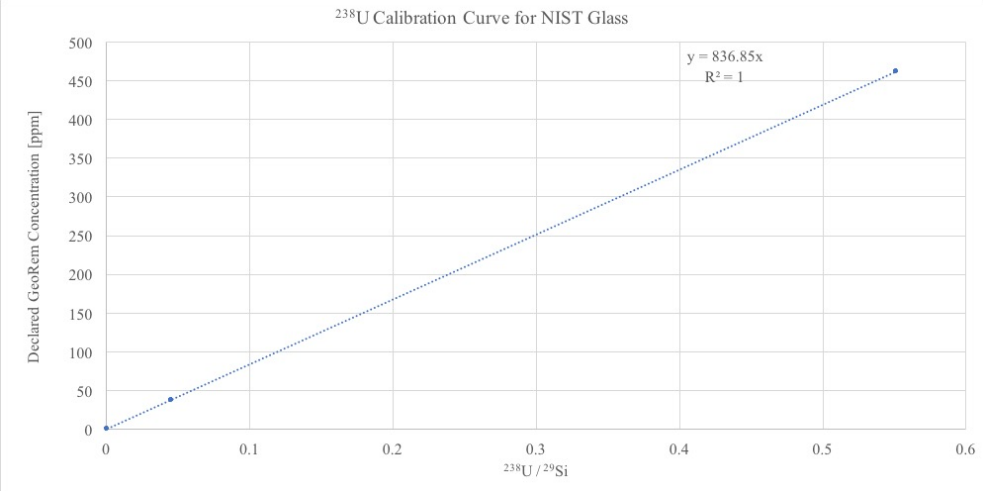

Figure 7.6: Calibration curve for ^{238}U.

7.5 Sample Images

Figure 7.7 shows 5x magnification of the end of Sample 5, highlighting the behavior of the ablation track across a gap.

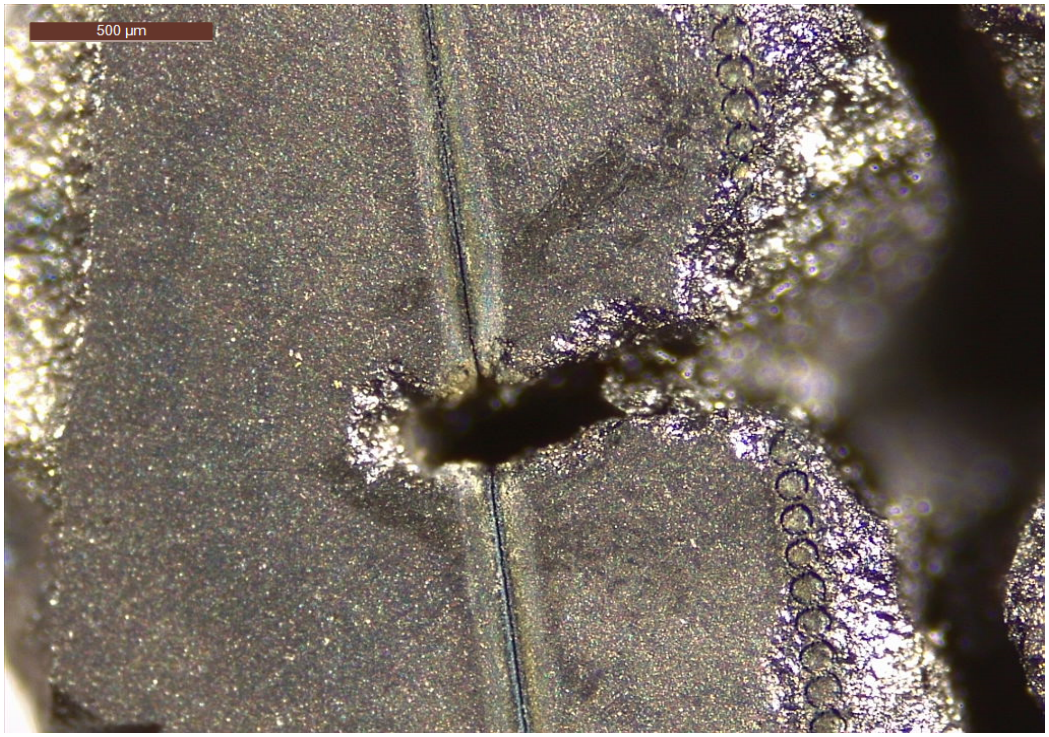

Figure 7.7: Optical image of Sample 5 showing the ablation track crossing a gap.

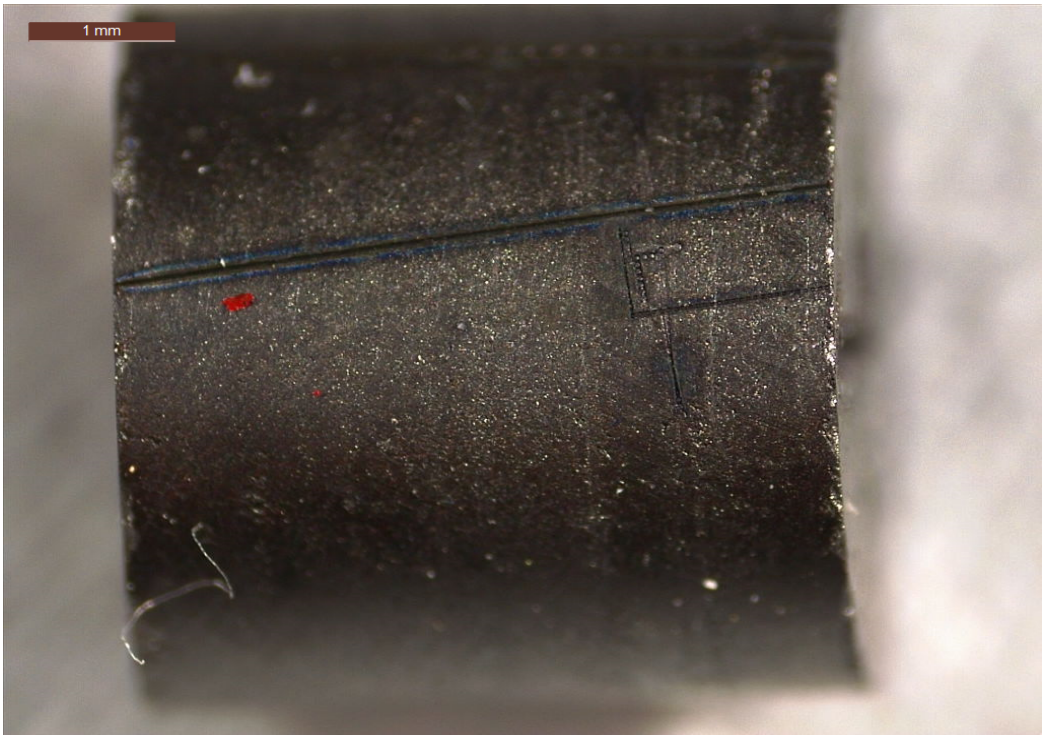

Figure 7.8: Optical image of Sample 1 showing a typical ablation track.

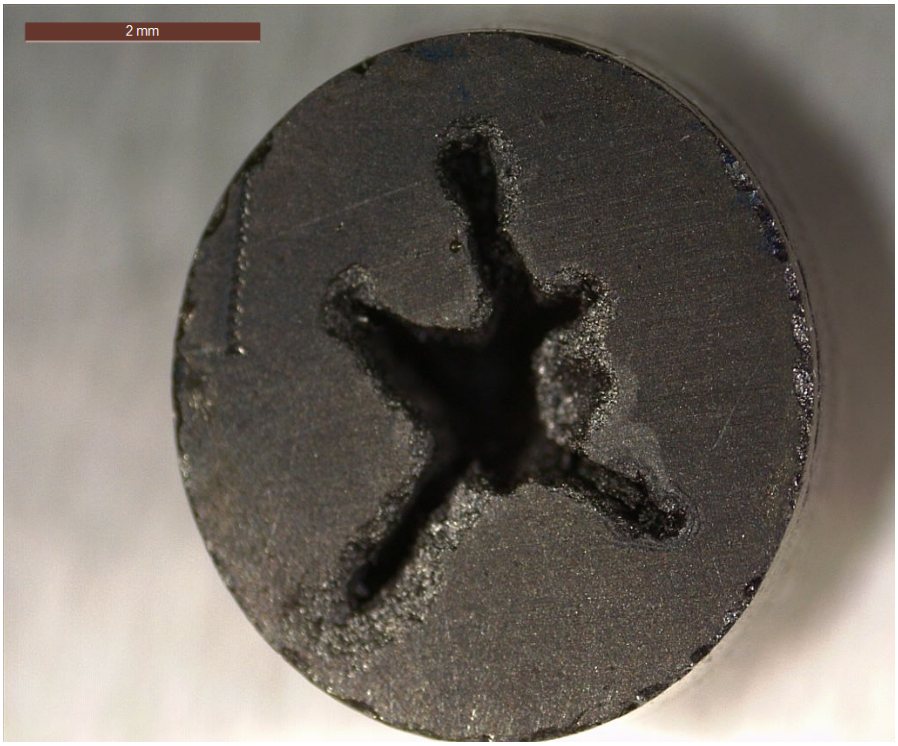

Figure 7.9: Optical image of the end of Sample 1 highlighting the void space.

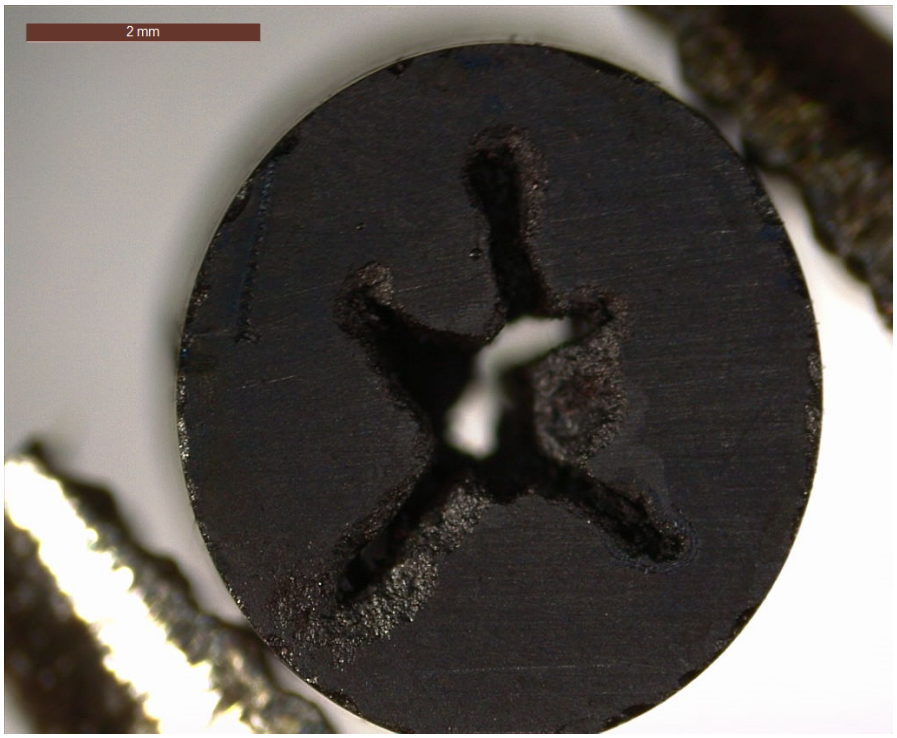

Figure 7.10: Optical image of Sample 1 demonstrating that the core is hollow.

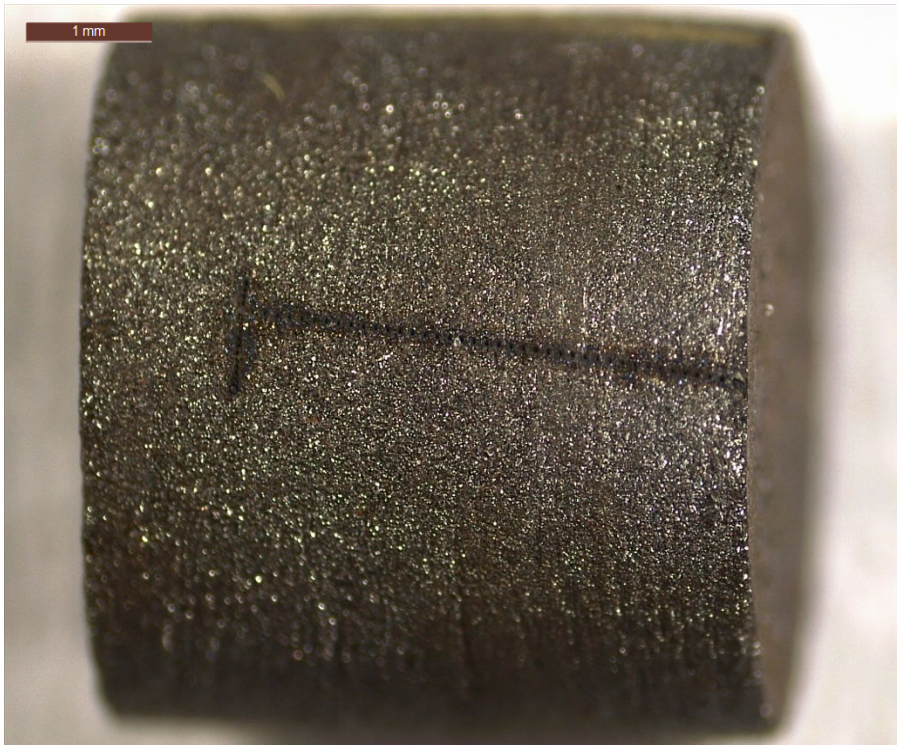

Figure 7.11: Optical image of Sample 2 showing the rough surface texture compared to the other samples.

Figure 7.12 shows an overview of the impact of slight changes in surface height relative to the laser objective on ablation efficiency in Sample 2.

Figure 7.12: Optical image of Sample 2 showing an overview of the impact of surface height variation on laser ablation efficiency.

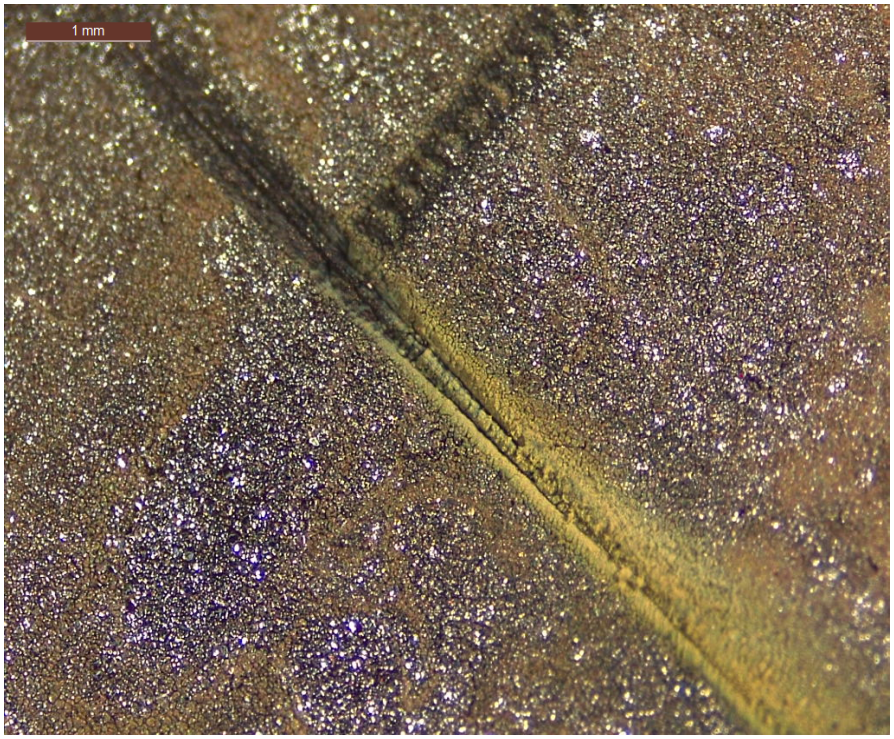

Figure 7.13: Optical image of Sample 2 shows a closeup of the impact of slight variations in surface height.

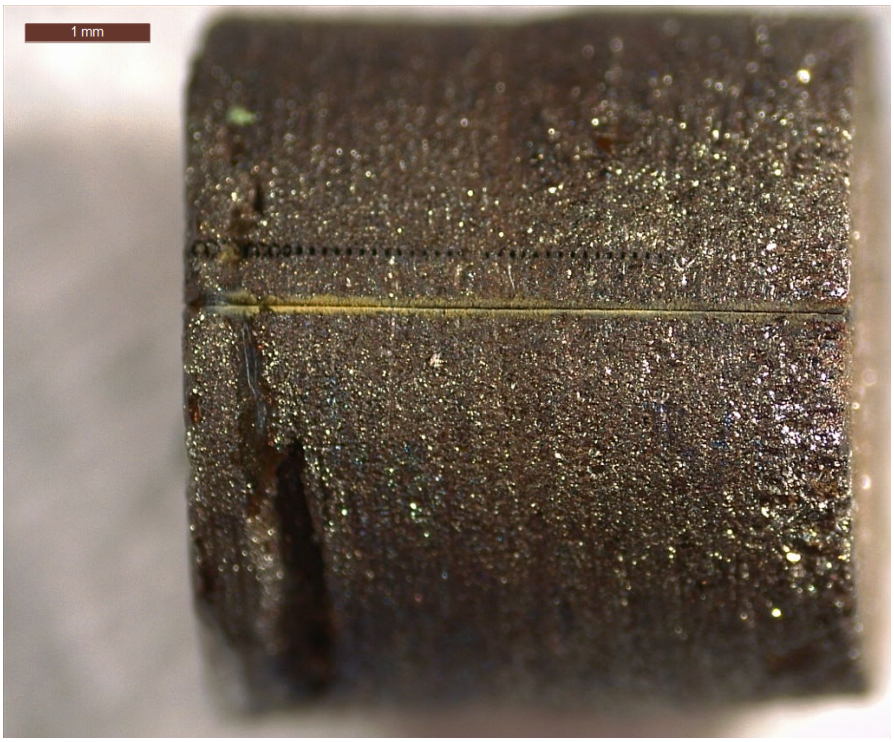

Figure 7.14: Optical image of Sample 3 demonstrating the difference between stepped and continuous translation on ablation effectiveness.

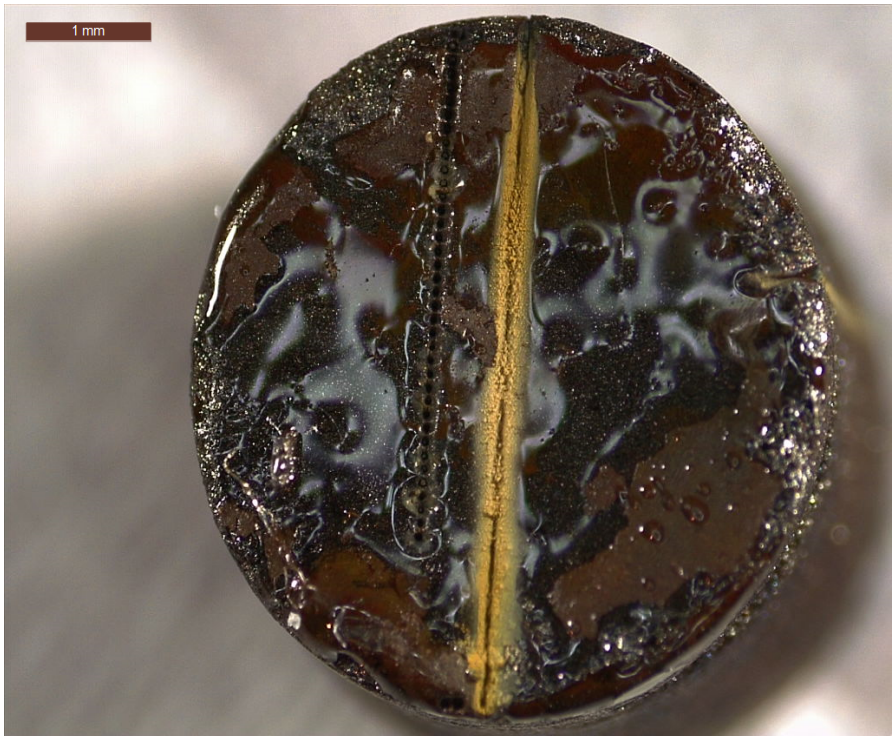

Figure 7.15: Optical image of stepped and continuous ablation tracks through variable surface texture across the end of Sample 3.

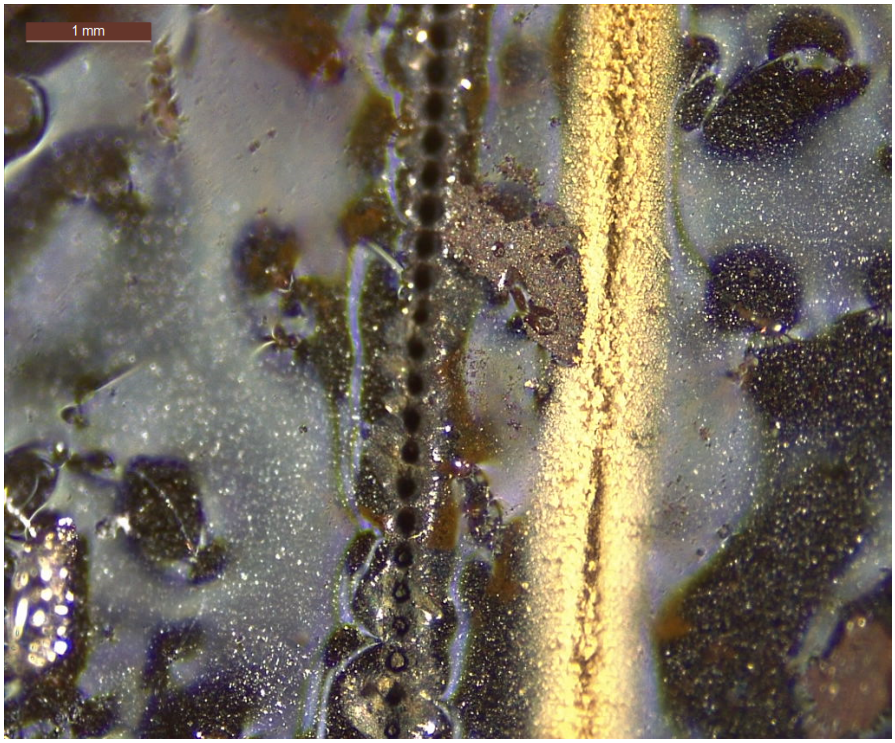

Figure 7.16: Optical image of Sample 3 showing a closeup of stepped and continuous ablation tracks.

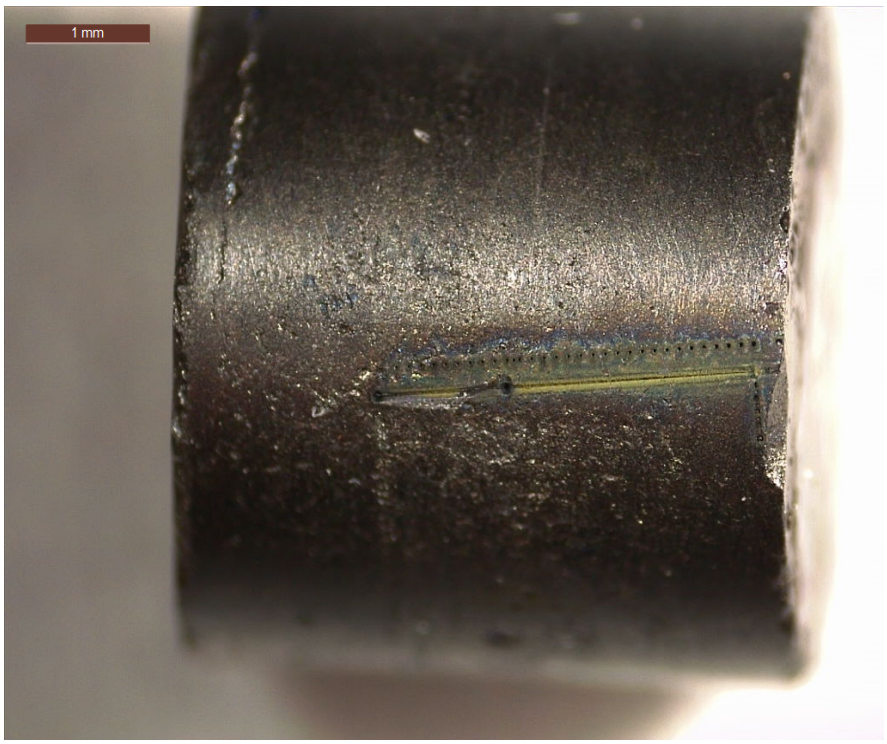

Figure 7.17: Optical image of a truncated ablation track along the axis of Sample 4.

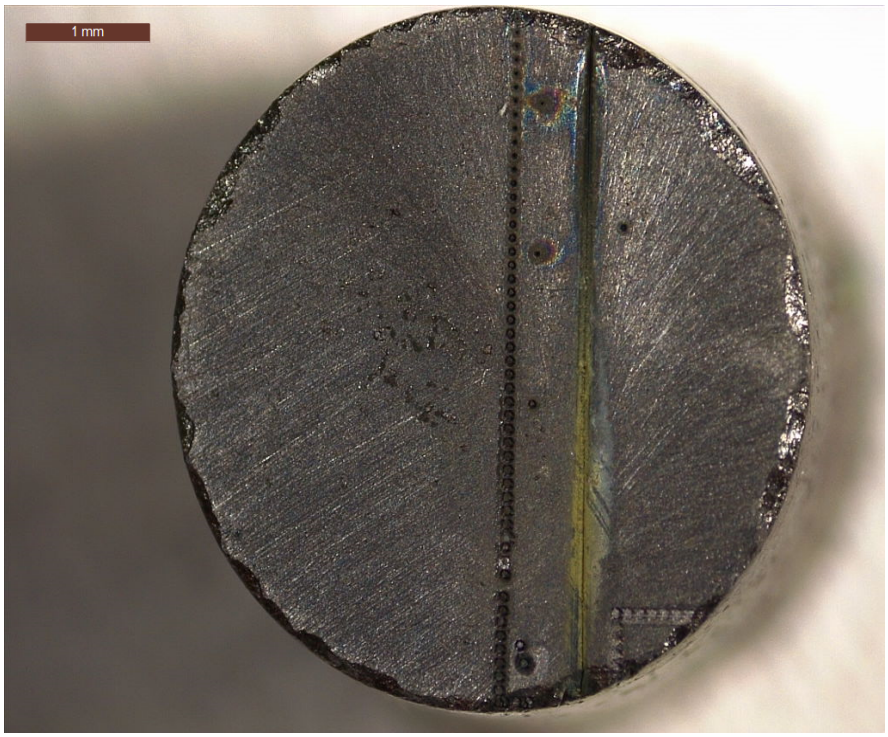

Figure 7.18: Optical image of Sample 4 showing the end surface texture.

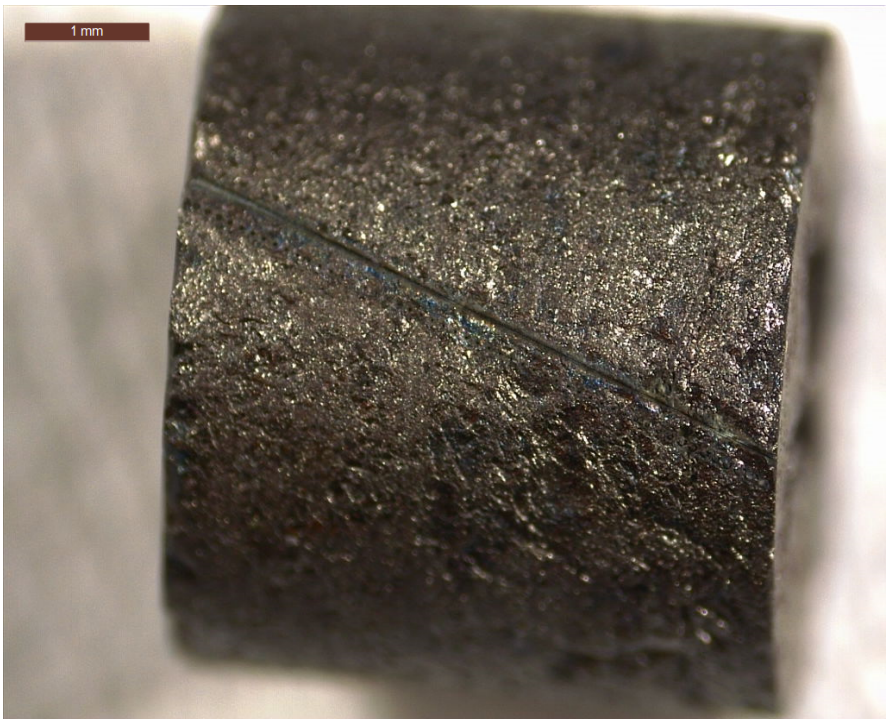

Figure 7.19: Optical image showing the loss of focus due to axial misalignment on Sample 5.

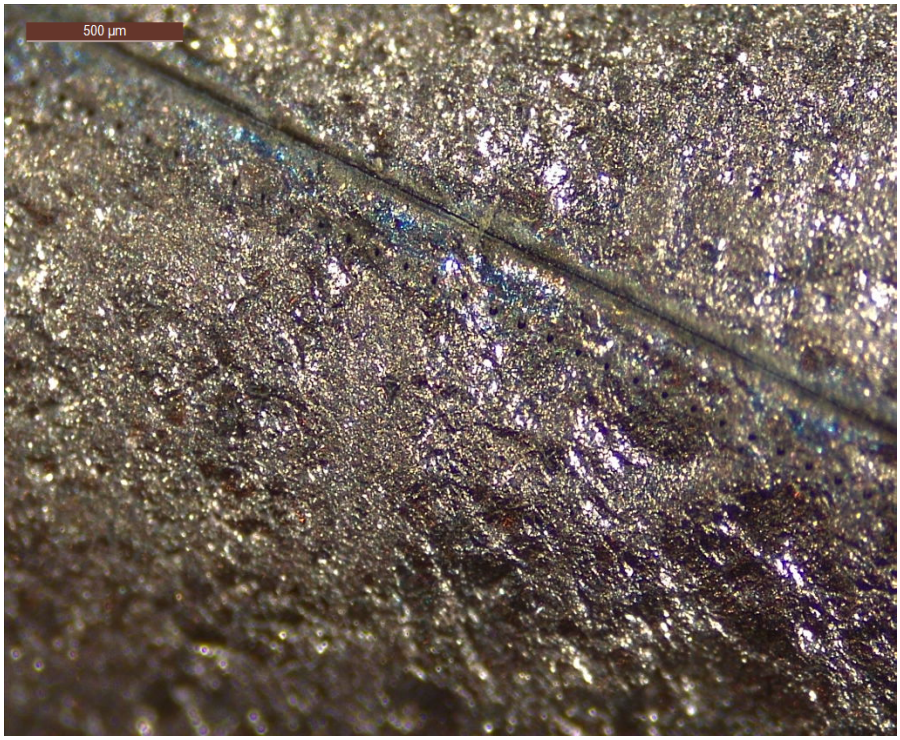

Figure 7.20: Optical image of Sample 5 showing a 5x closeup of stepped and continuous ablation tracks.

Figure 7.21: Optical image of ablation tracks across the end of Sample 5.

Figure 7.22: Optical image of Sample 5 showing the hollow core.

SEM Images

The following images were taken using a FEI SEM at LLNL.

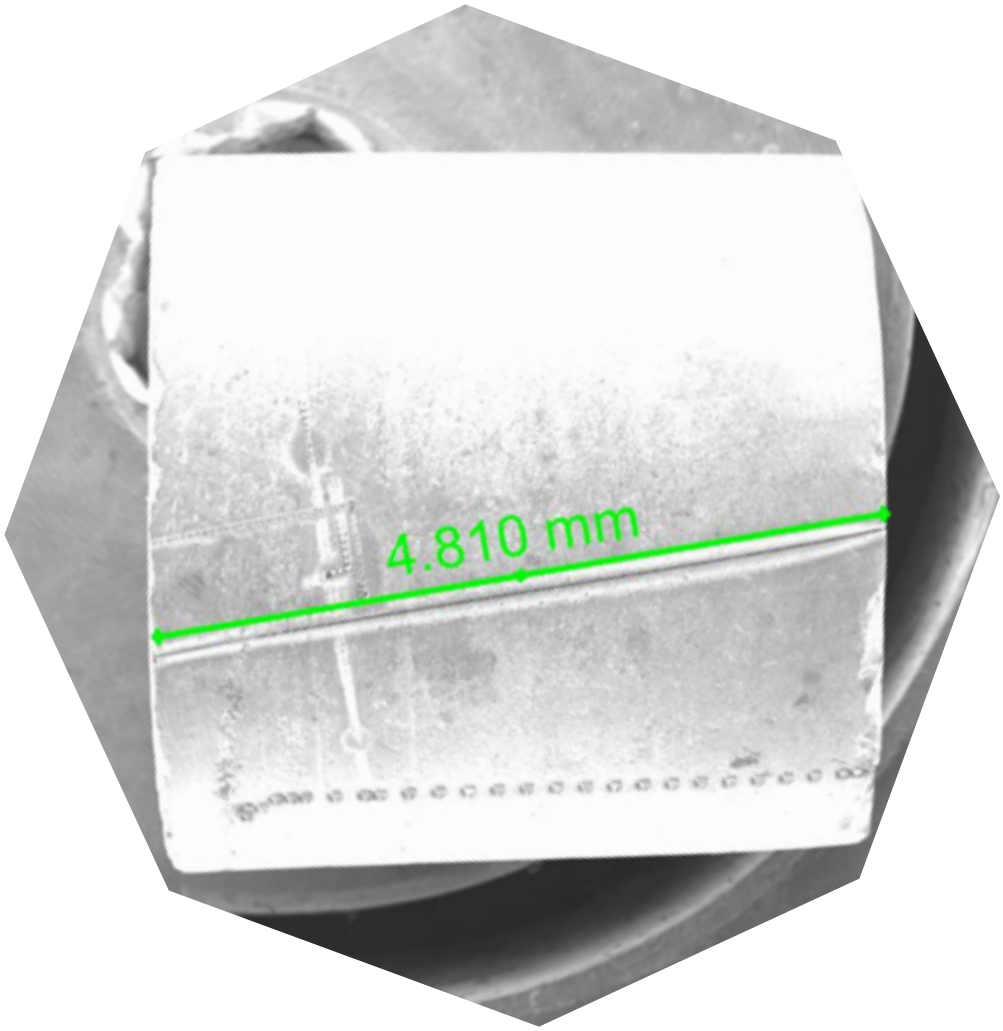

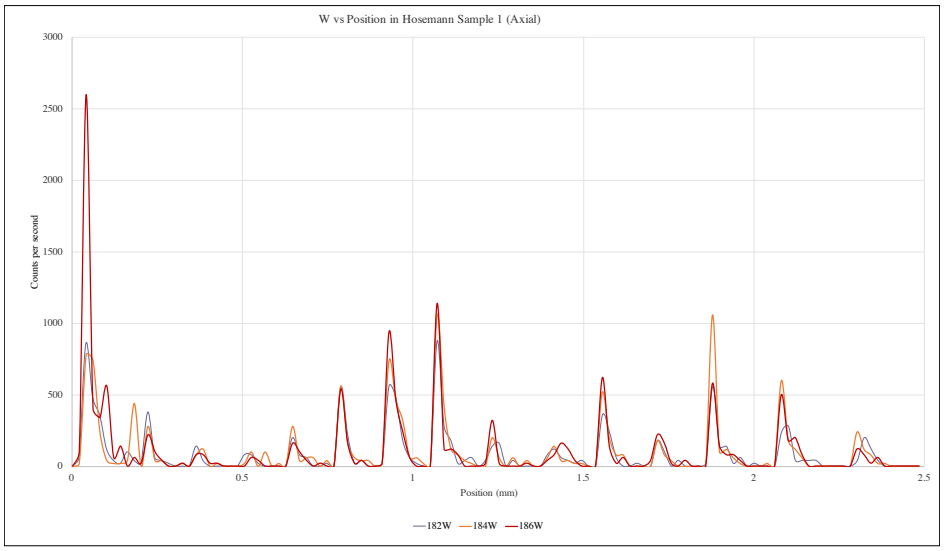

Figure 7.23: Sample 1 with ablation track and corresponding mass spectrum showing tungsten isotopes as a function of position along the ablation track.

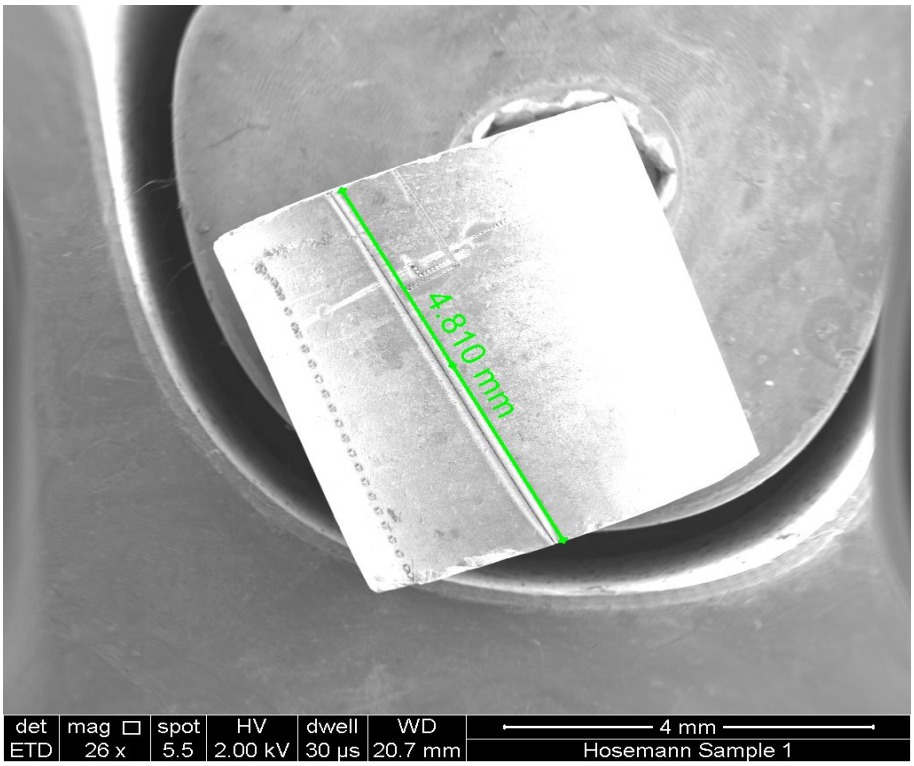

Figure 7.24: SEM image of Sample 1 showing ablation tracks and dimension.

Some samples were injected with polymethylmethacrylate (PMMA) to simulate void formation. The PMMA would be compressed within the pellets during formation, then evaporate away during sintering to leave behind voids, as shown in Figure 7.25.

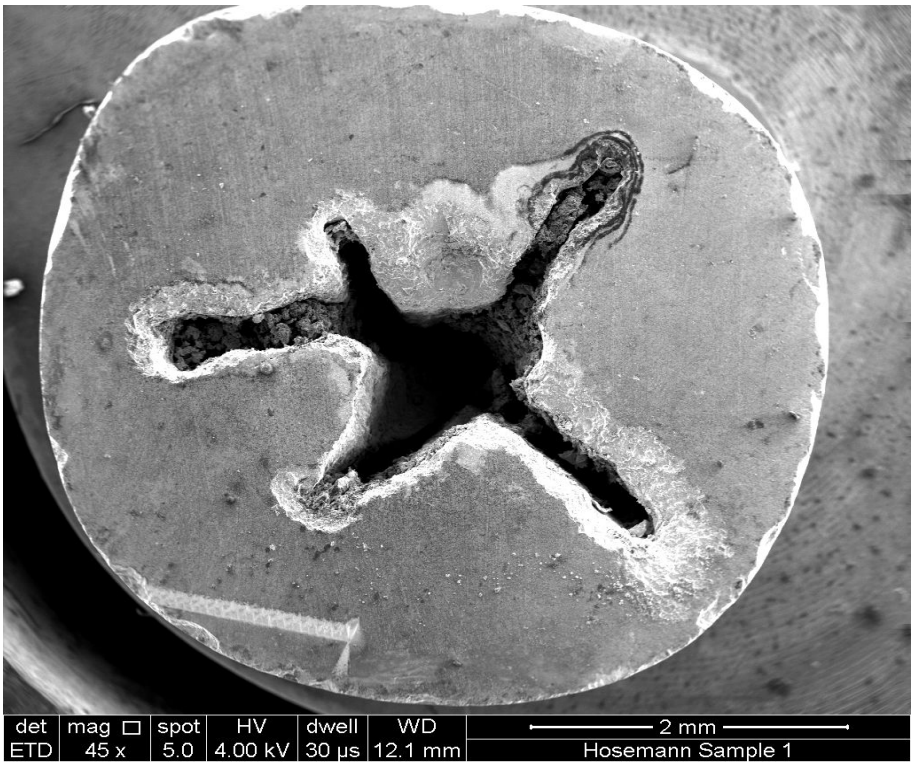

Figure 7.25: SEM image of Sample 1 end-on showing voids left by PMMA during fabrication.

Figure 7.26 shows an SEM image of a typical ablation crater on the end of Sample 1.

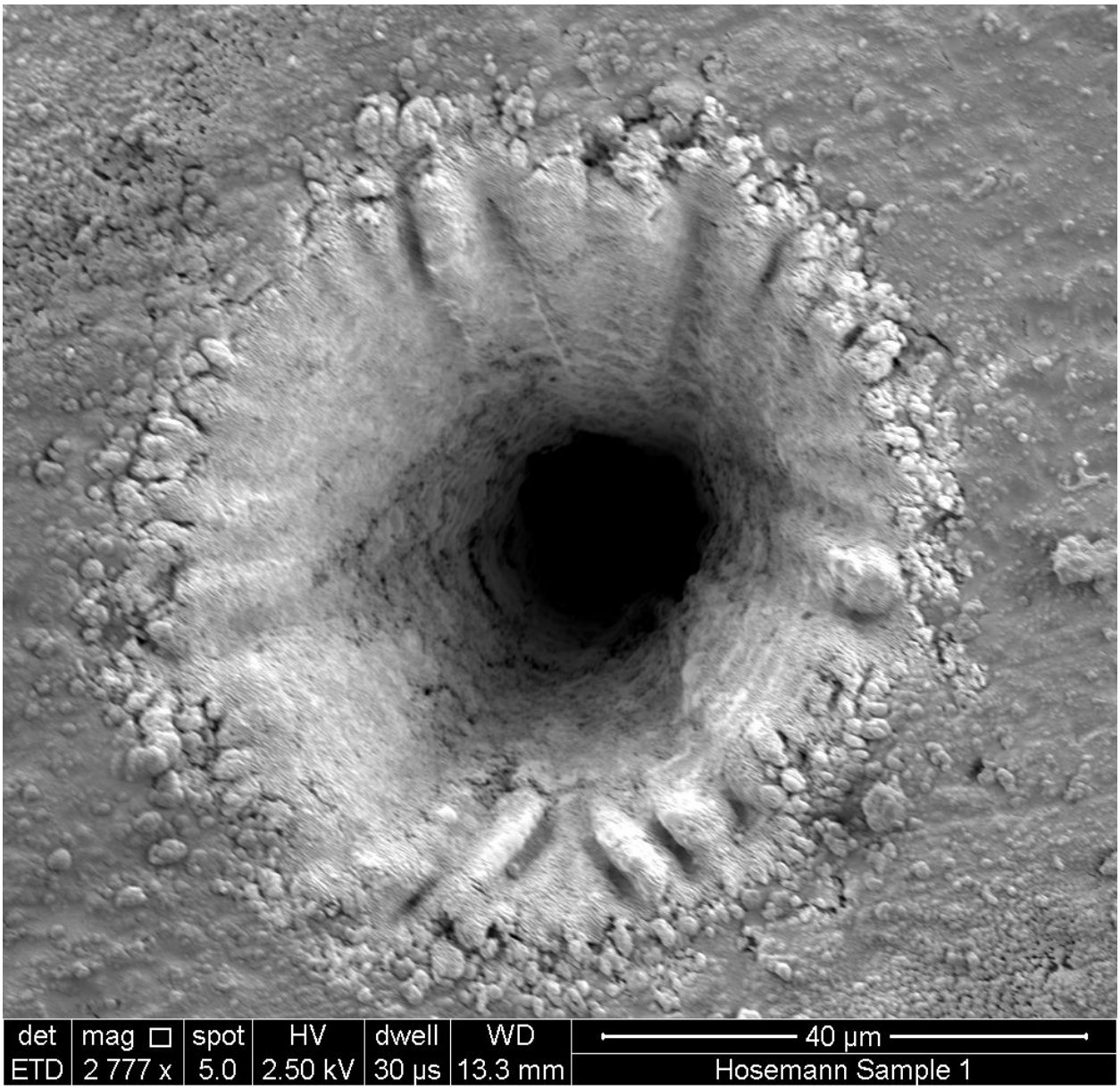

Figure 7.26: Typical ablation crater along the end radius of Sample 1.

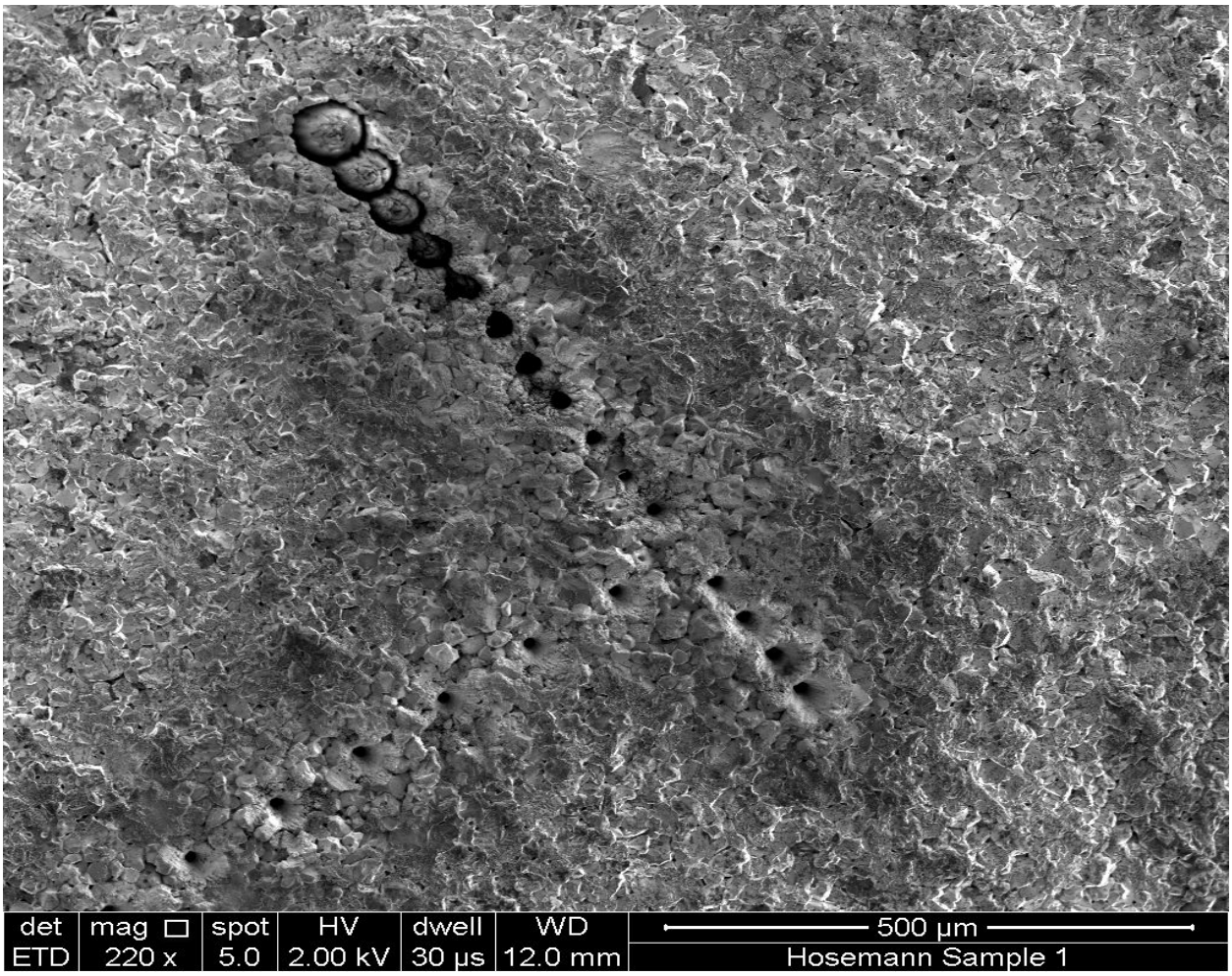

Figure 7.27: Axial and circumferential tracks showing rapid loss of focus about the sample waist.

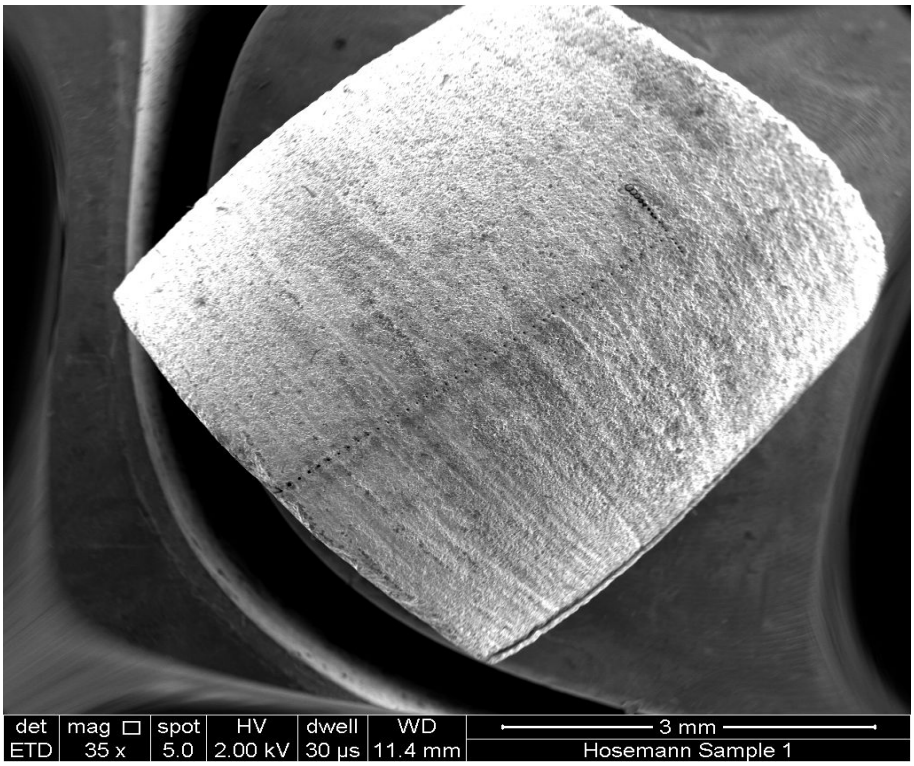

Figure 7.28: SEM image of Sample 2 showing ablation tracks and surface roughness.

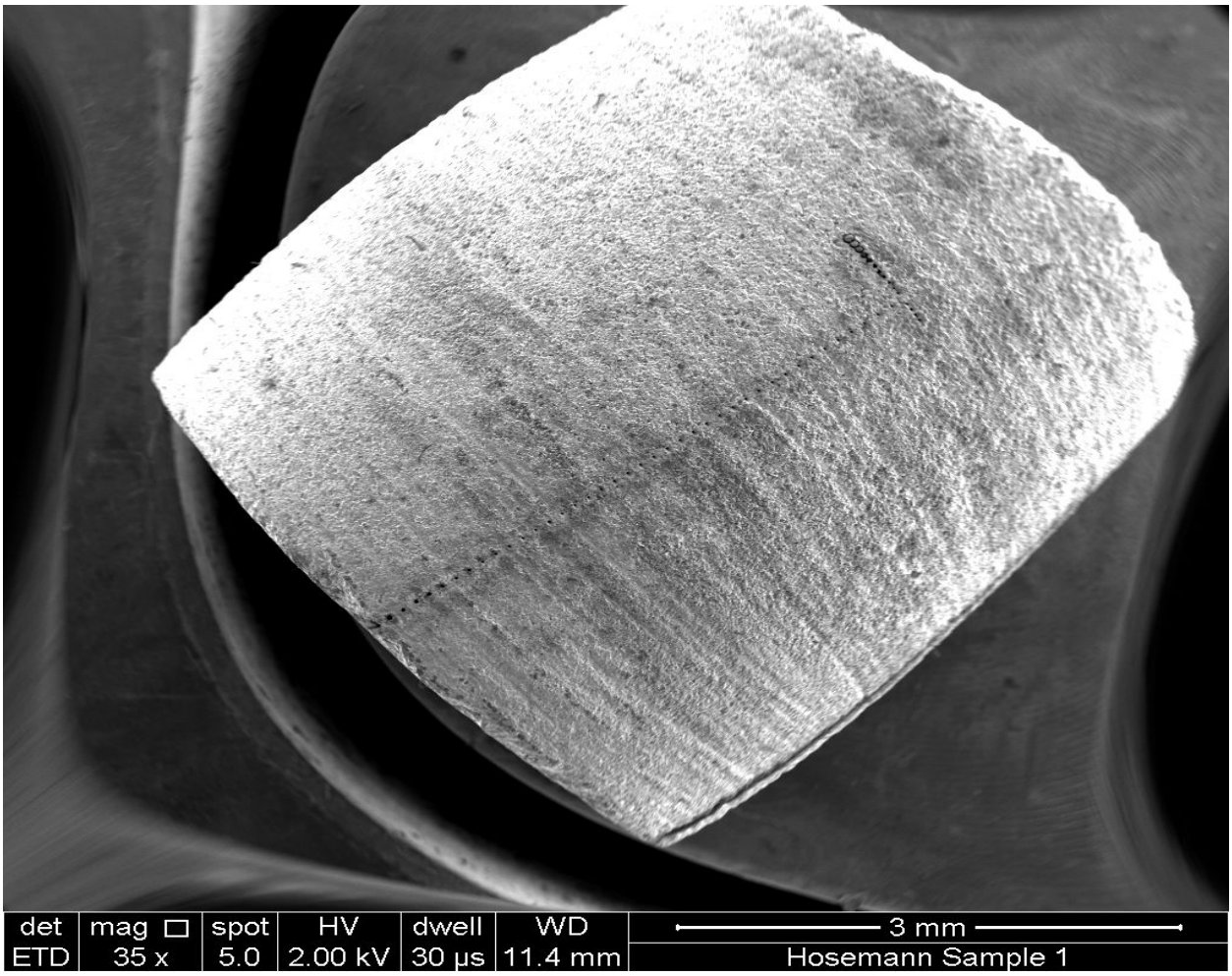

Figure 7.29: Overview of Sample 2 showing pulsed ablation track and significant surface roughness of the sample.

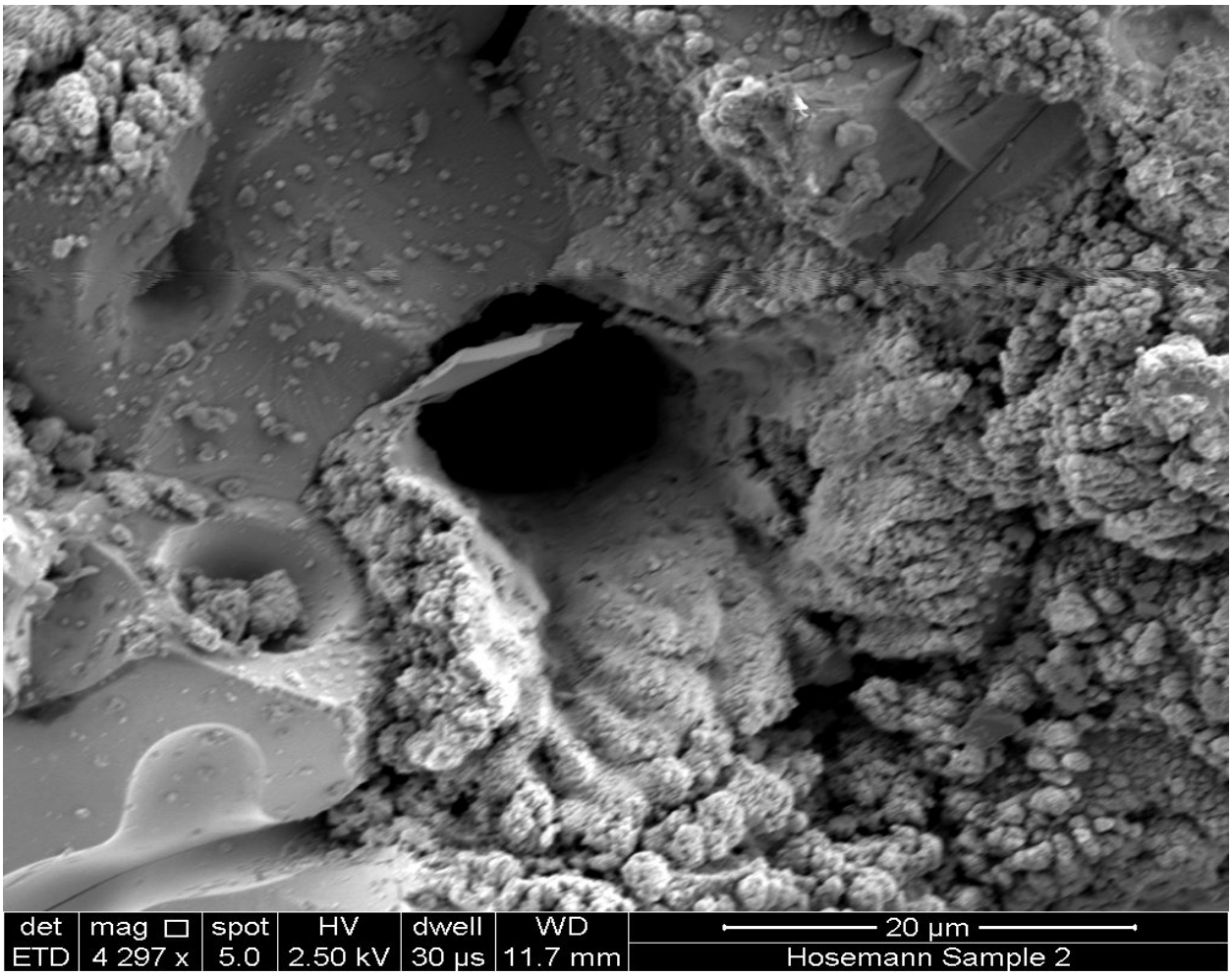

Figure 7.30: Closeup of an ablation crater showing clean ablation on top edge and debris on bottom edge.

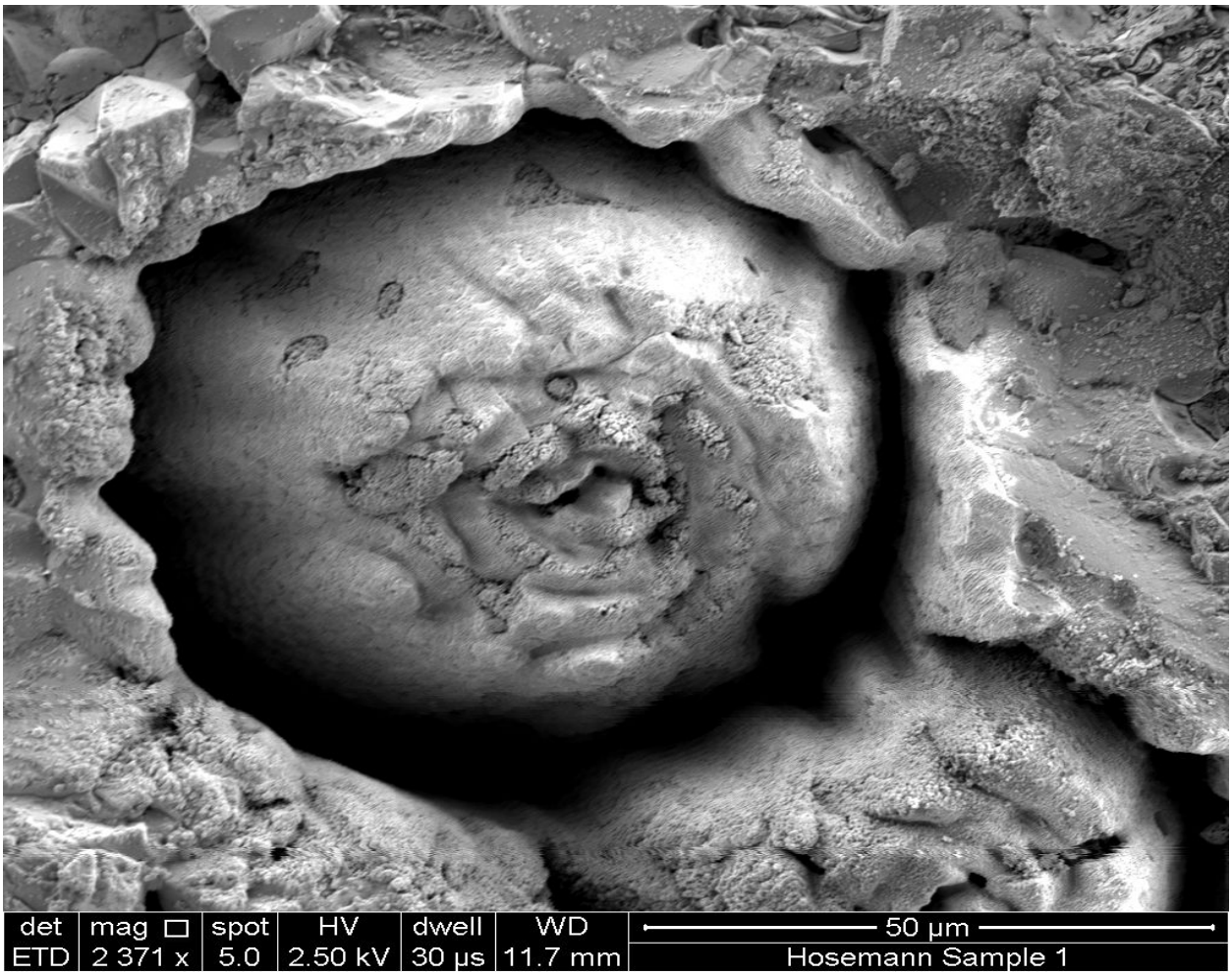

Figure 7.31: Closeup of ablation crater highlighting the effect of poor laser focus.

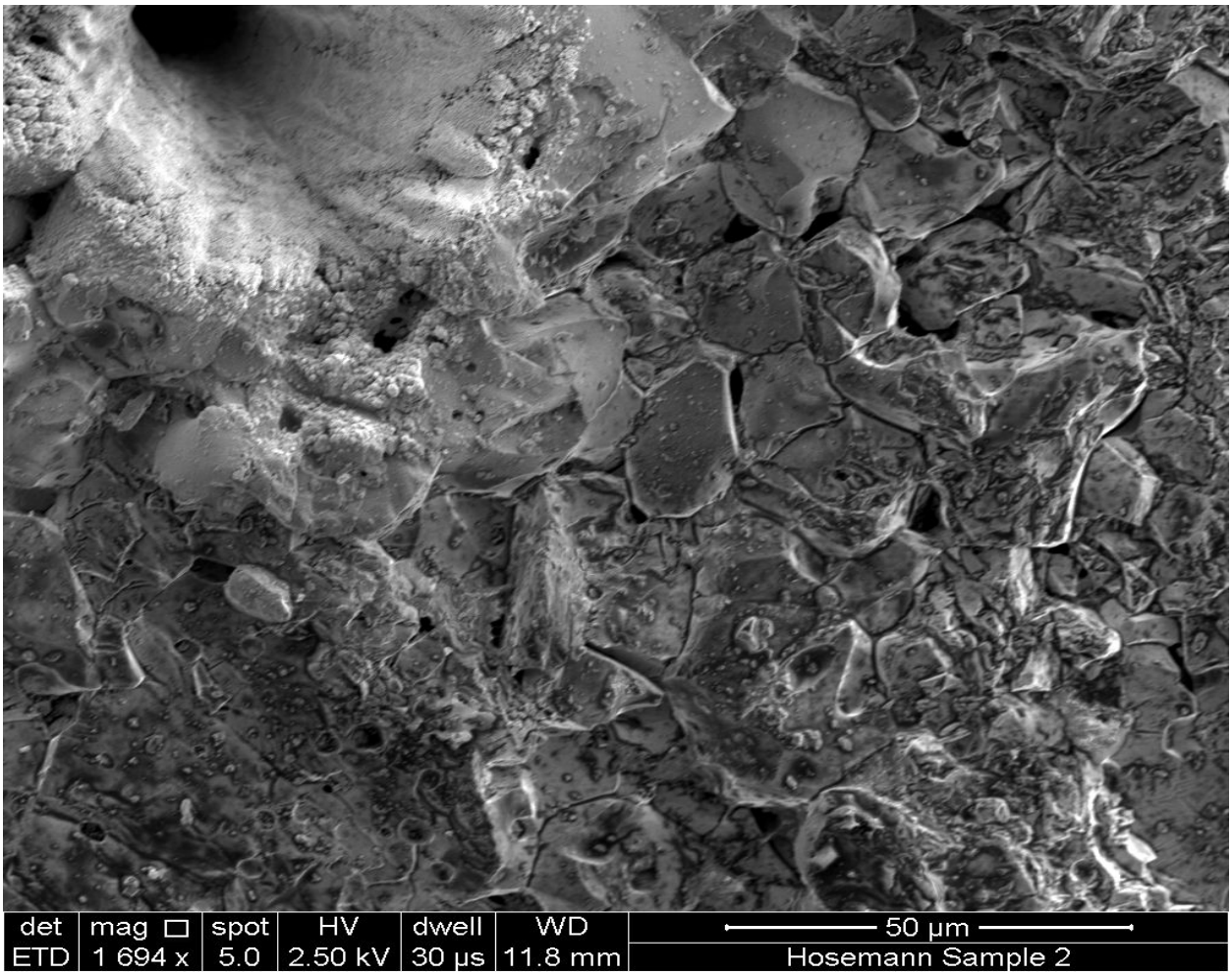

Figure 7.32: Closeup showing surface texture and ablation crater.

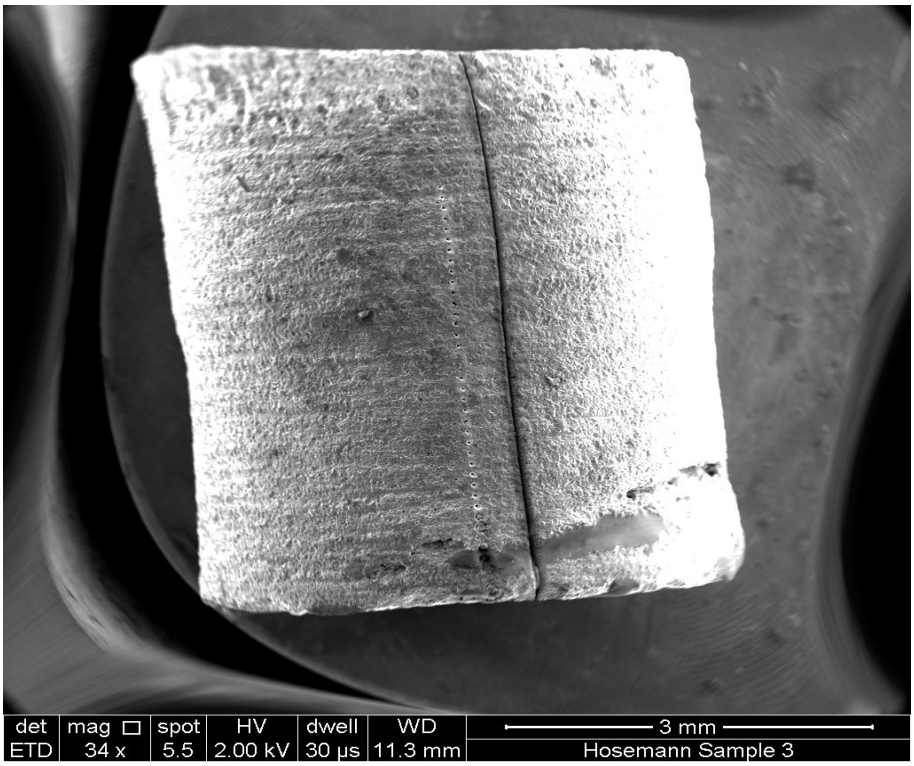

Figure 7.33: SEM image of Sample 3 showing pulsed and continuous ablation tracks.

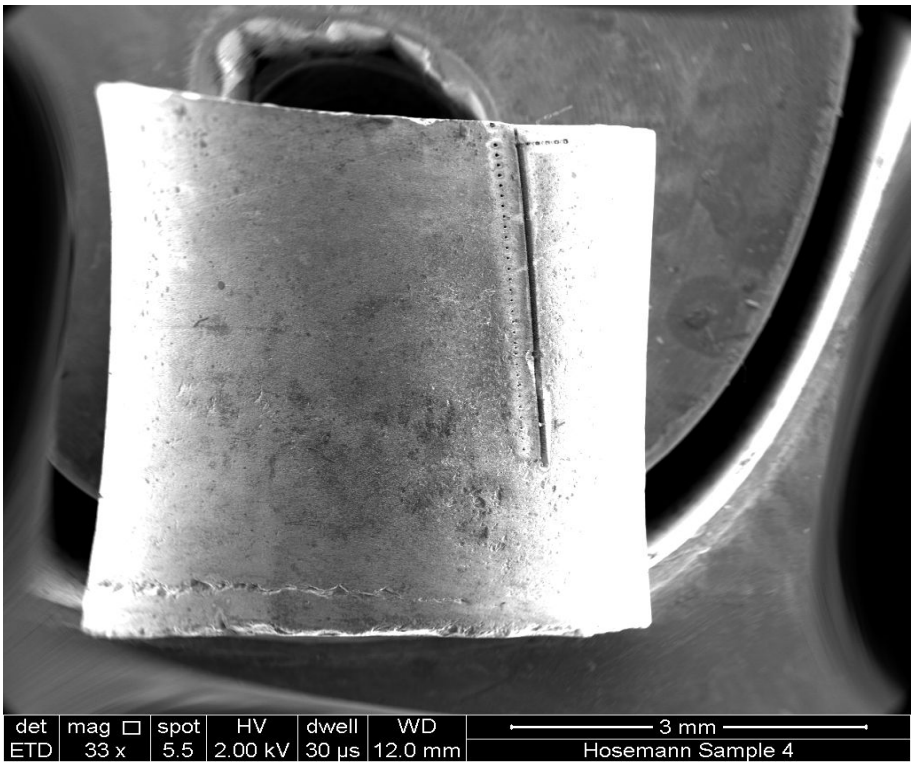

Figure 7.34: SEM image of Sample 4 showing pulsed and continuous ablation tracks across a surface smooth in comparison to Sample 2.

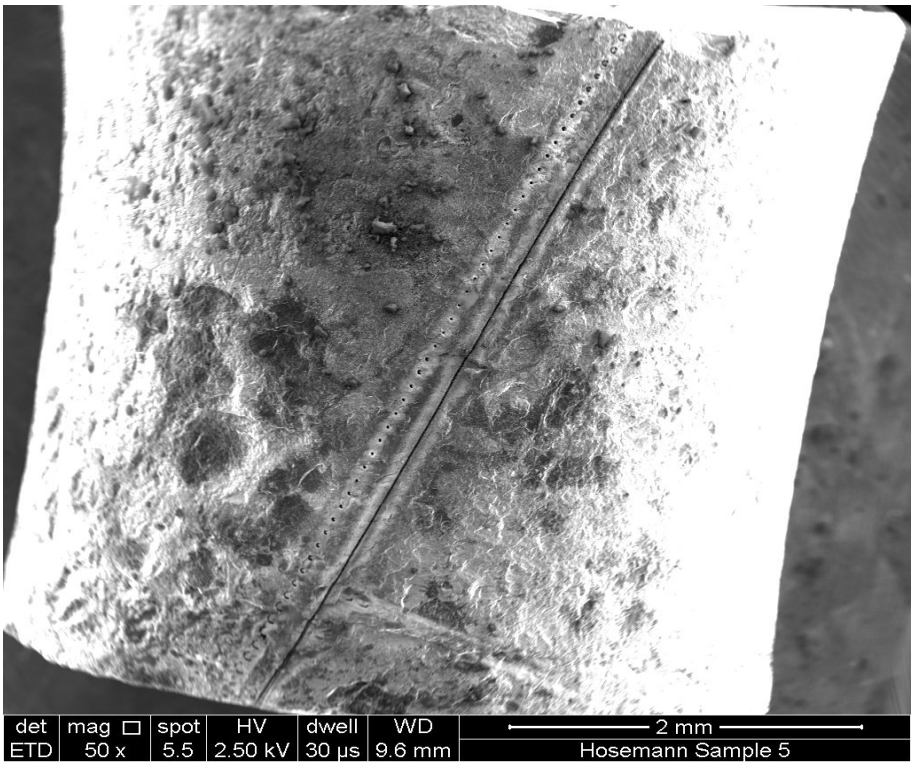

Figure 7.35: SEM image of Sample 5 showing pulsed and continuous ablation across a somewhat rough surface.

7.6 Mass Spectra

Many spectra were taken during this effort. The spectra below show characteristic results and highlight the flexibility of mass spectrometry to detect a wide range of isotopes.

Figure 7.23 compares the mass spectrum to an SEM image of the sample.

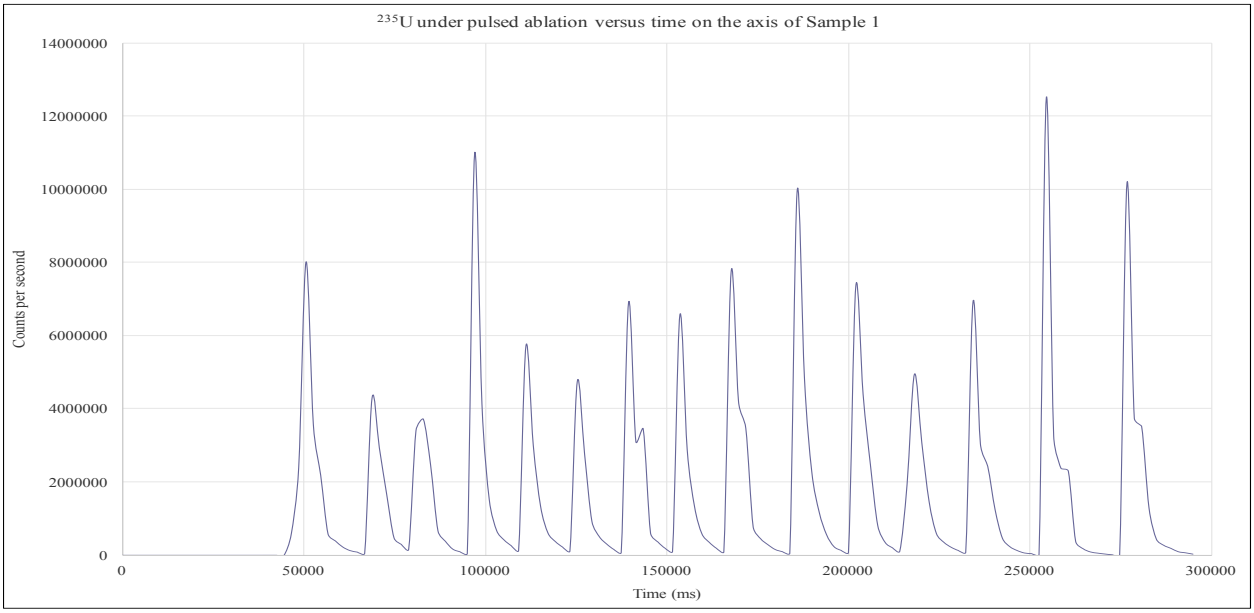

Figure 7.36: ^{235}U under pulsed ablation versus time on the axis of Sample 1.

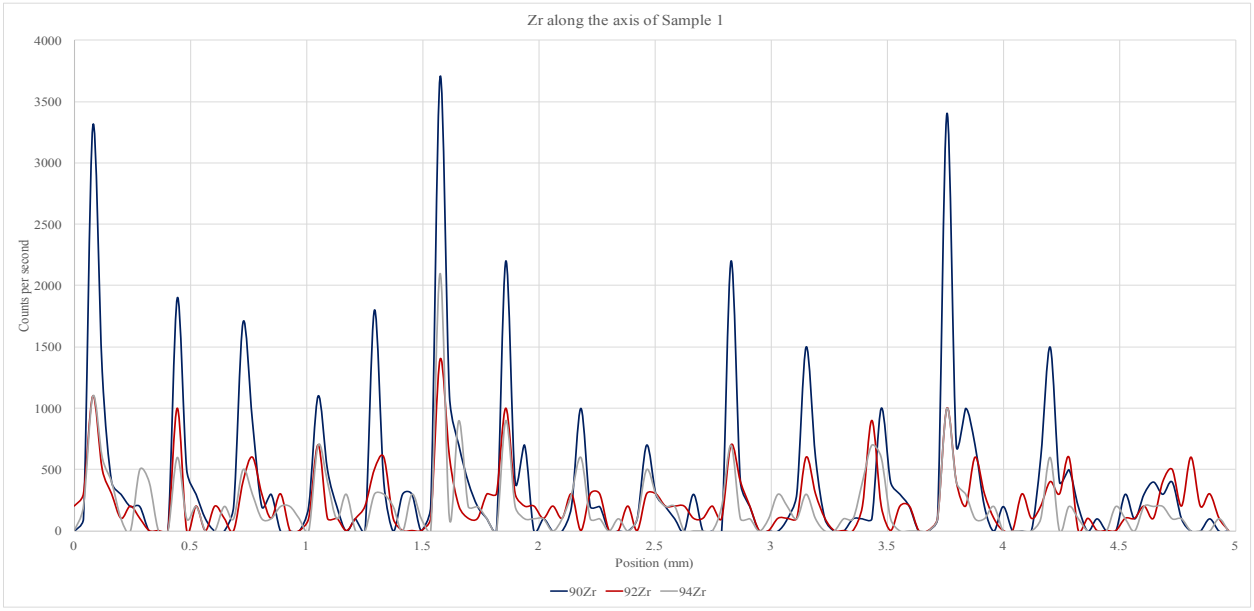

Figure 7.37: Zr isotopes versus position on the axis of Sample 1 under pulsed ablation.

Figure 7.38 shows an example of continuous ablation in contrast to Figure 7.36

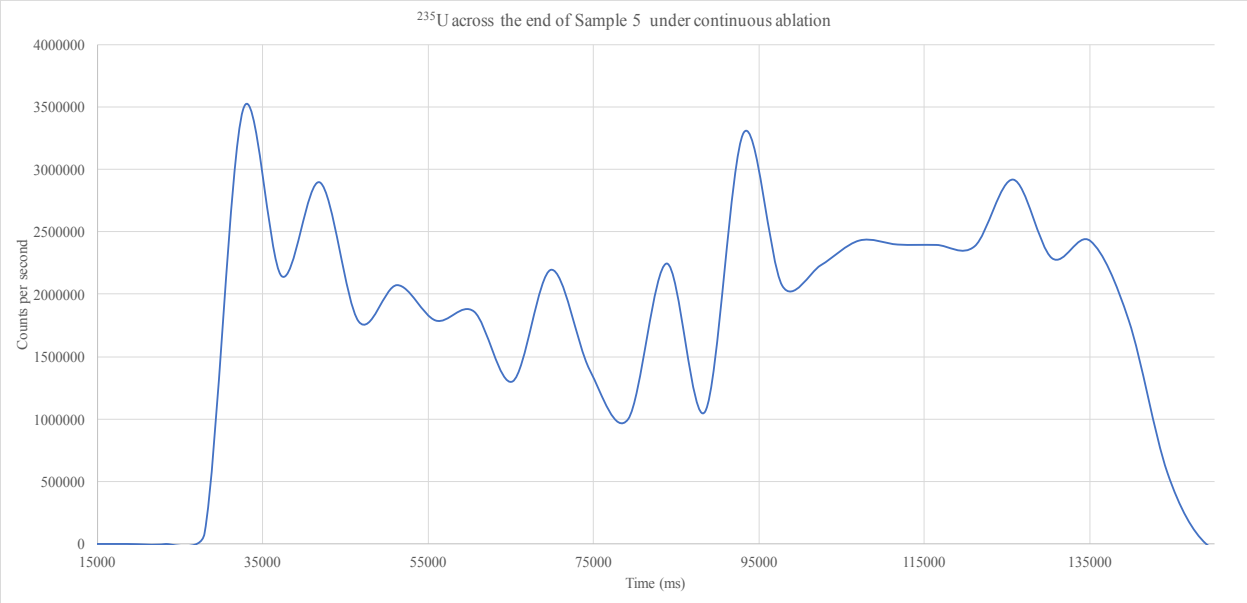

Figure 7.38: ^{235}U across the end of Sample 5 under continuous ablation.

Figure 7.39 shows an example of a strong tungsten signal at one end of Sample 2.

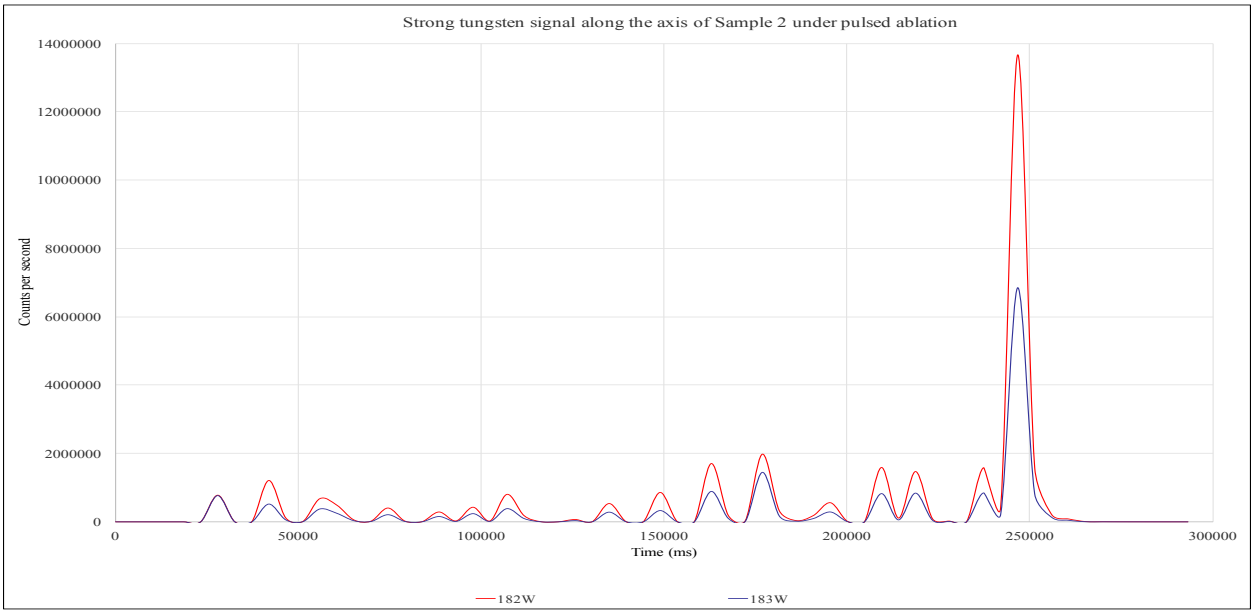

Figure 7.39: Strong tungsten signal along the axis of Sample 2 under pulsed ablation.

The following figures show some unexpected constituents such as gadolinium and lead in the samples. They are taken from various samples as illustrative examples.

Figure 7.40 shows an example of zirconium, here in Sample 5.

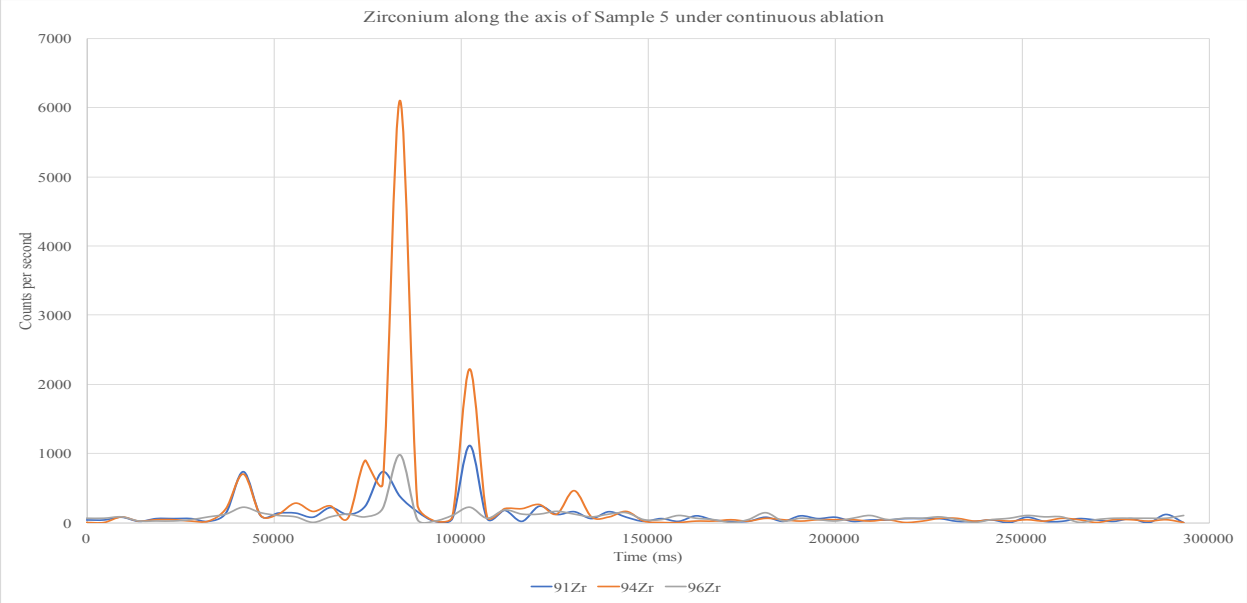

Figure 7.40: Zirconium along the axis of Sample 5 under continuous ablation.

Figure 7.41 shows the ^{140}Ce signal along the axis of Sample 5.

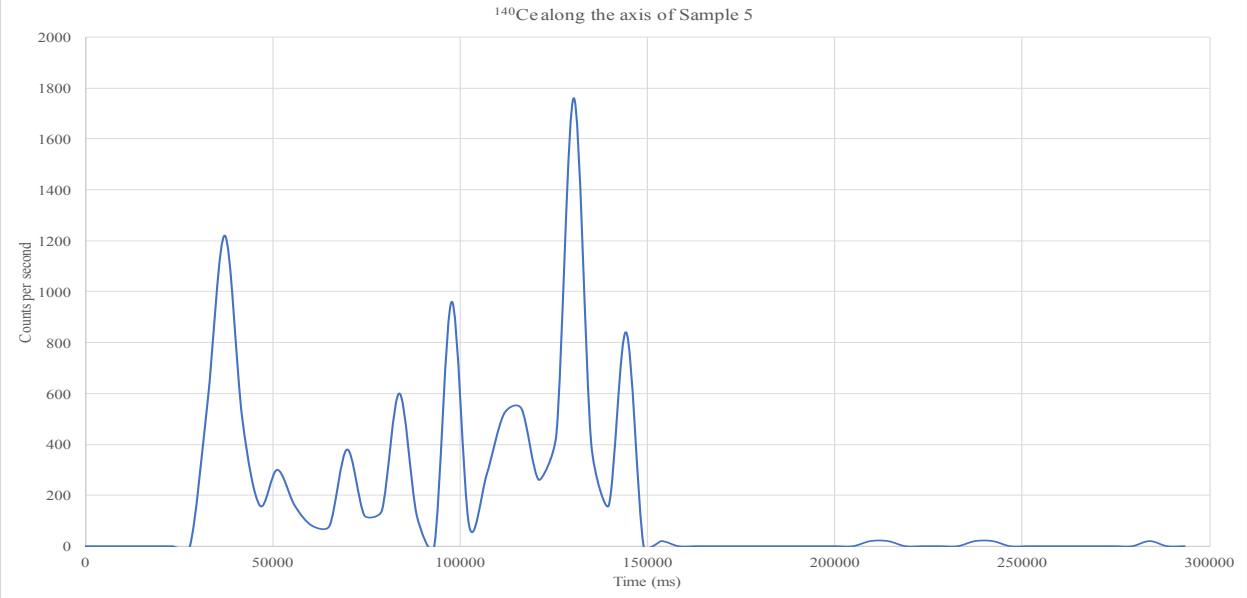

Figure 7.41: ^{140}Ce along the axis of Sample 5.

Figure 7.42 shows a relatively strong neodymium signal along the axis of Sample 5.

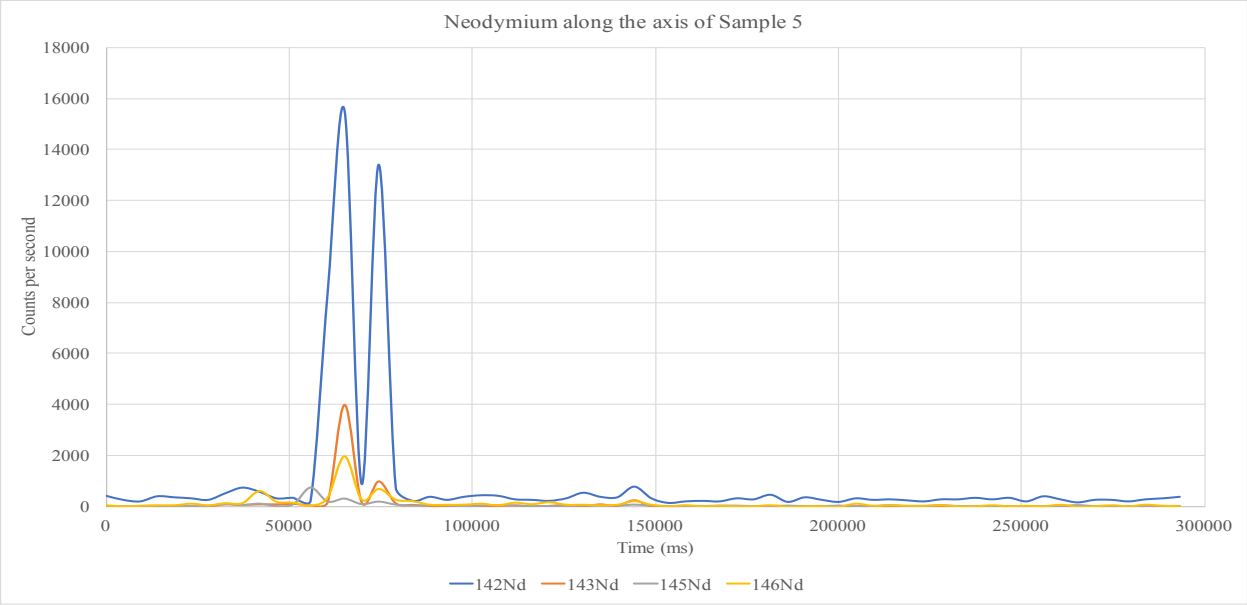

Figure 7.42: Neodymium along the axis of Sample 5.

Figure 7.43 shows lead along the axis of Sample 5.

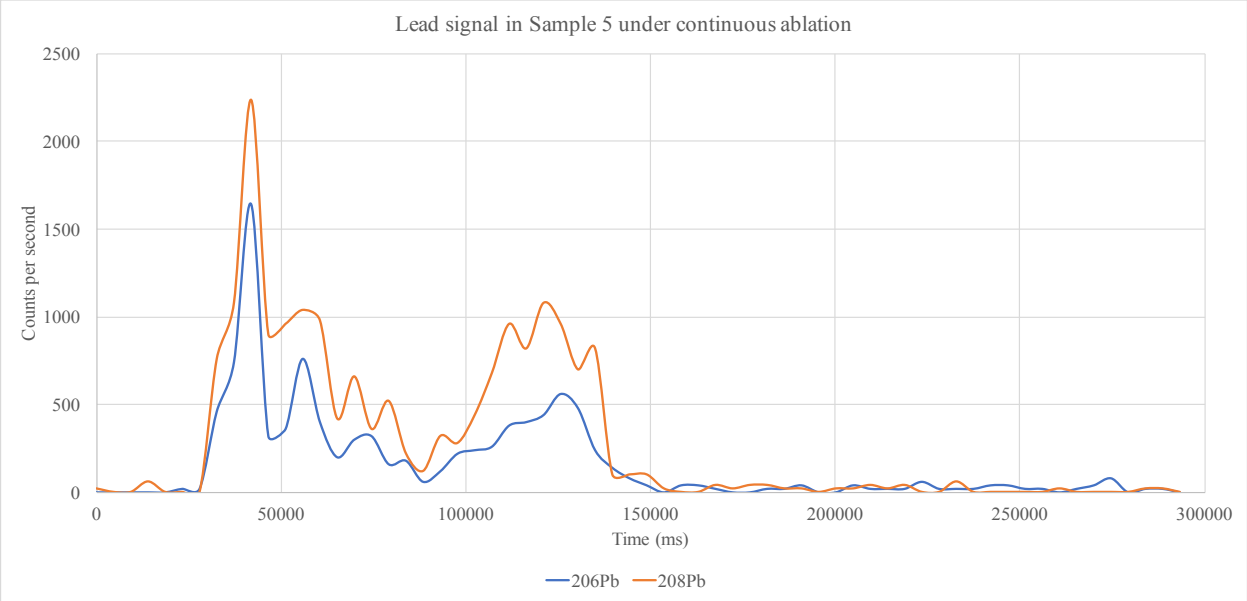

Figure 7.43: Lead signal in Sample 5 under continuous ablation.

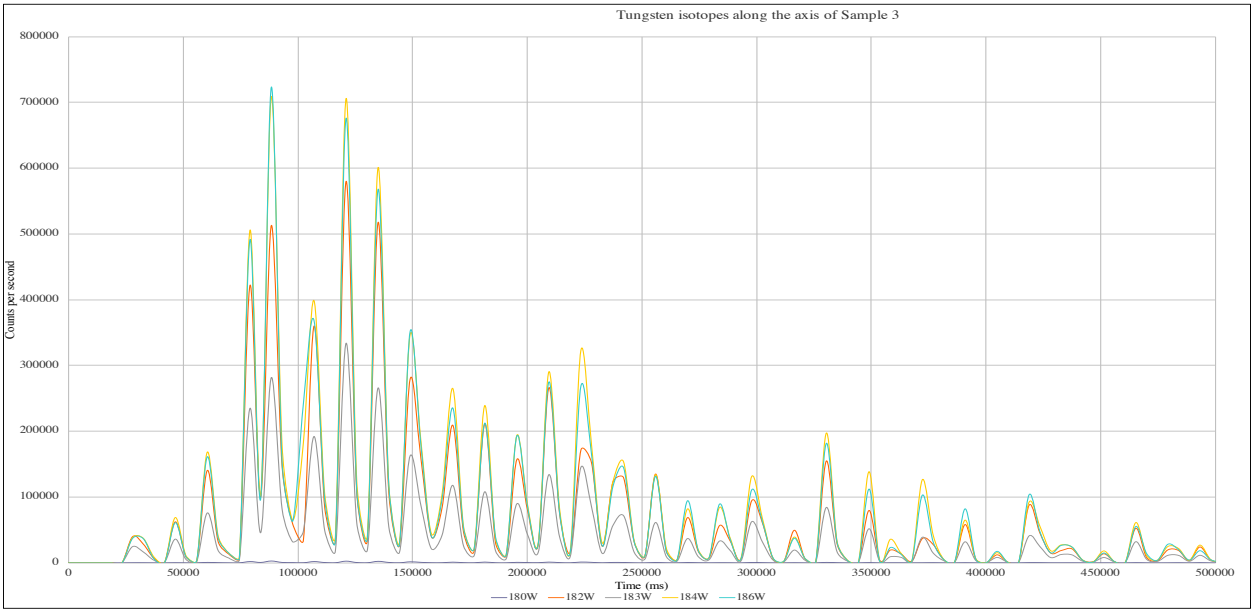

Figure 7.44: Tungsten isotopes along the axis of Sample 3.

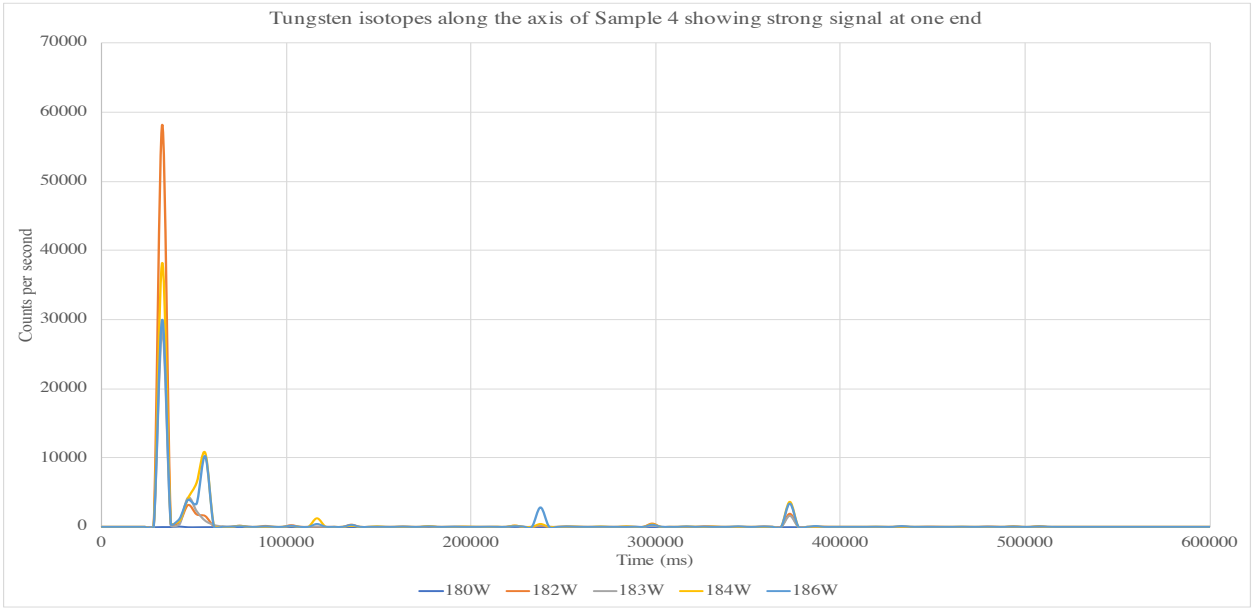

Figure 7.45: Tungsten isotopes along the axis of Sample 4 showing strong signal on one end

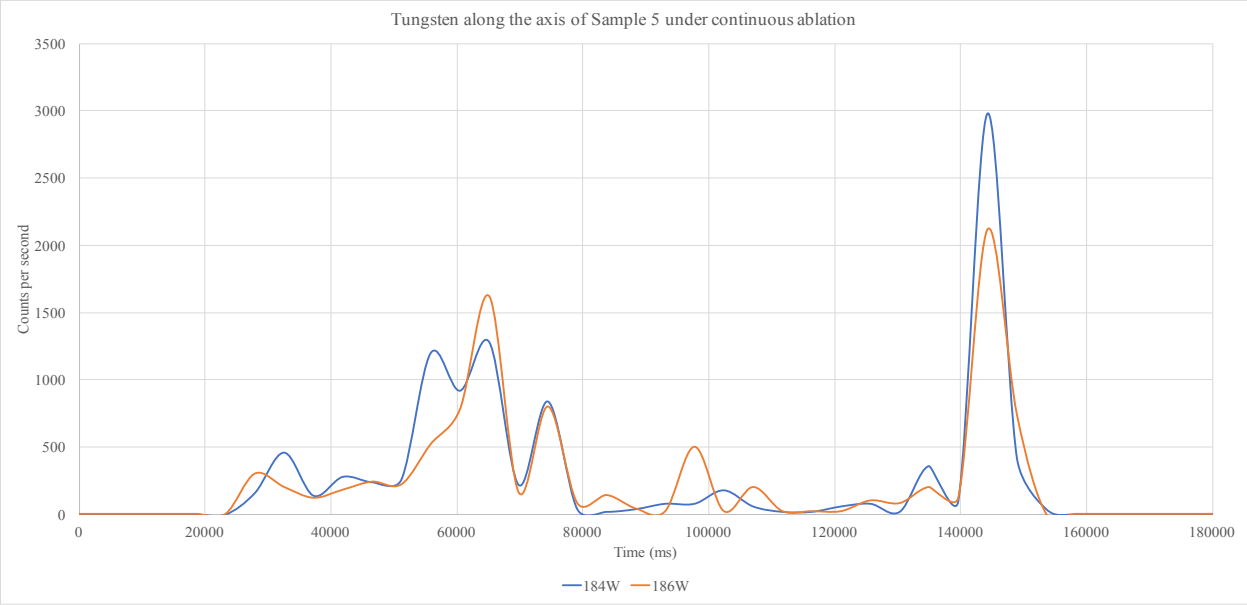

Figure 7.46: Tungsten along the axis of Sample 5 under continuous ablation showing generally low signal.